Nuclear graphite: Structural characterisation and effects of irradiation

Brindusa Elena Mironov

Submitted in accordance with the requirements for the degree of

Doctor of Philosophy

The University of Leeds
Institute for Materials Research
School of Chemical and Process Engineering

September, 2014

The candidate confirms that the work submitted is her own and that appropriate credit has been given where reference has been made to the work of others.

This copy has been supplied on the understanding that it is copyright material and that no quotation from the thesis may be published without proper acknowledgment.

Acknowledgements

My first thoughts and thanks go to my supervisors for all the resources and time invested in me: Prof. Rik Brydson, to which I am greatly indebted for the invaluable discussions, scientific guidance and encouragement given during the course of my PhD, Dr. Aidan Westwood, for funding my PhD studies and the opportunities he gave me and Dr. Andrew Scott, for cheering me up and encouraging me.

I would also like to express my deepest gratitude to Dr. Andy Brown for his time, discussions and continuous support which all kept me determined and focused during the final stages of my PhD.

I would like to express my true appreciation to Dr. William Windes, from National Idaho Laboratory, US, for providing me the neutron-irradiated samples, which were instrumental in the completion of my research. My thanks go also to Miss Helen Freeman, for the collaboration on the electron irradiation and beam convergence studies. In particular, I would like to thank Dr. Fredrik Hage for making my life easier by developing the script in Hyperspy, which facilitated the EELS data analysis.

I would like to thank the LEMAS team members: Dr. Michael B. Ward, and Mr. John P. Harrington, for their time and support. I thank also Mrs. Diane Cochrane for her support and encouragements through all the years.

I would like to thank all the other peers and PhD students who I have worked with during my studies at Leeds, for their friendship and support in all these years of challenging times: Dr. Mehrdad Irannejad, Mr. Yothin Chimupala, Mr. Tarun Kakkar, Dr. Sussane Selle, Dr. Fangyuan Zhu, and, in particular, Miss Helen Freeman.

Finally, I would like to thank my family for their support and patience during my studies, especially my sister, who gave me strength and ambition, and who taught me to learn from the past, but to look at the future.

Abstract

This thesis investigates graphites used in nuclear materials engineering applications – so called nuclear graphites. As well as outlining a microstructural model for nuclear graphite, it aims to develop a new understanding for nuclear graphite degradation under neutron irradiation and at high temperatures by the use of different characterization techniques and different irradiating species.

Part of the thesis aims to develop a new methodology for understanding nuclear graphite and its damage processes via the correlative use of different characterisation methods and by novel data processing methods applied to characterisation data. This includes use of electron energy loss spectroscopy (EELS) acquired under damage free conditions and analysed using an improved automated fitting method in order to extract information on carbon bonding within the samples. Some of this methodology was developed using *in situ* electron irradiation of nuclear graphite.

A range of different virgin (unirradiated) nuclear graphite grades were initially investigated and these were compared in terms of the crystallite coherence lengths obtained from X-ray diffraction (XRD) and by the relative proportions of non-graphitic carbon derived from Raman spectra. From both these results and from scanning and transmission electron microscopy (SEM and TEM) an initial model was developed for micro- and nano-structure of the complex composite graphitic material.

Neutron irradiated nuclear graphites were then sourced and analysed using XRD, Raman and TEM/EELS and the effect of degradation was studied as variation of irradiation dose and temperature in terms of the change in crystallite size and carbon bonding. These results indicated a model involving the fragmentation of graphite crystallites and an increase in porosity during irradiation with the presence of some effects due to annealing of defects at higher temperatures. This is similar to a previous model developed for electron irradiation at doses lower than 1 dpa and temperatures lower than 370 °C.

Table of contents

Table of Figures

Tables

Abbreviations and symbols

a, c	Lattice parameters
AGC	Advanced Graphite Creep
AGR	Advanced Gas-Cooled reactors
ATR	Advanced Test Reactor
BF	Bright field
BSU	Basic structural unit
BWF	Breit-Wigner-Fano
C_2	Current of the second condenser lens
CCD	Charge Coupled Device
CL	Camera Length
CTE	Coefficients of thermal expansion
CVD	Chemical vapour deposition
DF	Dark field
d_{hkl}	The inter-planar distance corresponding to (hkl)
DP	Diffraction pattern
dpa	Displacement per atom
E_D	Displacement threshold energy
EELS	Electron Energy Loss Spectroscopy

E_i	Kinetic energy of the incident electron
ELNES	Electron energy near-edge structure
E_{TEM}	Energy of the electrons
EXELF	Extended electron energy loss fine structure
FEG	Field Emission Gun
FFT	Fast Fourier Transforms
FIB	Focused Ion Beam
FWHM	Full width half maximum
F_X	Pore accumulation parameter
GILSO, GIL	Gilsocarbon graphite
HOPG	Highly Oriented Pyrolitic Graphite
HRTEM	High resolution transmission electron microscope
HTGR	High Temperature Gas-cooled reactor
HTR	High Temperature Rectors
I_D	Intensity of the graphite D peak from Raman spectra
I_G	Intensity of the graphite G peak from Raman spectra
IR	Infra - red
J	Electron fluence
k	The shape factor

L_a	Coherence length/ Dimension of the crystallite in the a direction
L_c	Coherence length/ Dimension of the crystallite in the c direction
MA	Magic angle
m_c	Carbon mass
m_e	Electron mass
NG	Nuclear graphite
NGNP	US Next Generation Nuclear Plant
PBMR	Pebble Bed Modular Reactor
PGA	Pile grade A graphite
PKA	Primary knock-on atom
R	GIF entrance aperture radius
RS	Raman Spectroscopy
SAED	Selected Area Electron Diffraction
SEM	Scanning Electron Microscope
SKA	Secondary Knock-on Atoms
TEM	Transmission Electron Microscope
UNGG	Natural Uranium Graphite Gas reactor
UV	Ultra violet
VHTR	Very High Temperature Reactor
XRD	X-Ray Diffraction

X_T	Evolution of crystallites dimension parameter
α	The convergence angle
θ	The Bragg angle
θ_E	Characteristic scattering angle
β	Collection semi-angle
β^*	The effective collection semi-angle
δ	Full width of Bragg XRD peak at half-maximum height
ν_0	the Rayleigh scattering energy
ν_M	the Raman Stokes or anti Stokes scattering
σ_d	The displacement cross section
ω_g	G position in the Breit-Wigner-Fano definition

Chapter 1 Introduction

Graphite is a key part of nuclear reactors as moderator, reflector, and major structural component material, whether they are Advanced Gas Cooled Reactors (AGR), or Magnox reactors [1]. Used in 80% of current UK I and II generation nuclear plants, graphite is likely to be the first material considered for future high temperature gas cooled reactors because of its thermal stability and integrity [2].

Inside a nuclear reactor, the graphite blocks are subject to high levels of radiation that result in chemical and physical properties changes, affecting neighbouring reactor components. The lifetime of reactors is therefore primarily governed by the performance of the graphite, an accurate estimation of its condition being essential for economic success, and plant safety. The characterization and comparison between the virgin graphite structure, and of the damage evolution after neutron irradiation, have an important role in predicting the long-term behaviour of graphite. A systematic study will support the development of more accurate theoretical models which are able to predict the behaviour of graphite, and will also help the improvement of new materials to be used in current and future nuclear reactors.

Nuclear graphite is a synthetic material produced from pitch and petroleum coke particles, with a high degree of crystallinity following major thermal treatment at high temperatures (graphitization) [3]. When the graphitization process is complete, two main features can be distinguished: the majority filler particles, and the minority binder phase, both of which are formed by domains of aligned individual crystallites. Both features have potentially inter- and intra- structural porosity, ranging from Mrozowski cracks between crystallites (50 nm -10 μm) to micro and macro pores around domains, and particles [4–6].

The properties of nuclear graphite are determined by its structure, which can be changed by the neutron irradiation dose, irradiation temperature, and oxidation. Inside a reactor, these parameters can significantly alter the crystallite size and the lattice parameters of the graphite crystallites, with the **a**-axis contracting and the **c**-axis expanding - assuming that the crystallites are aligned with their **a**-axis parallel with the extrusion direction [7], hence influencing bulk properties by interfering with the integrity and dimensions of nuclear graphite components. Even though the full details and mechanisms are not fully understood, it is clear that the solidity and working life of reactor components are influenced by dimensional changes, creep and weight loss, amongst other effects of neutron irradiation [7].

Since the 1940s, a lot of effort has been spent in understanding the behaviour of irradiated graphite. The bulk properties of damaged features have been thoroughly experimented upon [3,5,8,9] and theoretical models have been derived [10,11]. Although this has allowed behavioural changes in the irradiated bulk, to be partly accounted for in current and future graphite based reactor designs, the mechanisms of such processes at the nano scale still remain uncertain. The irradiation database for nuclear graphite is incomplete and old. Old, because of the space between the beginnings of the “nuclear era” (~1940s), when characterization was made on virgin or low level irradiated nuclear graphites and incomplete, because of the gaps in data due to inconsistent irradiation regimes studied. Furthermore, existing models for graphite behaviour do not explain the real performance inside nuclear reactors, and also do not predict accurately multi-scale behaviour. The study of real reactor irradiated samples which come from decommissioned rectors with a working life of around 20 - 30years, could improve the knowledge data base and offer new hypothesis in revealing the true behaviour of nuclear graphite when irradiated.

This work investigates the structure of both virgin, and neutron graphites irradiated at different doses and temperatures (Chapter 2).

The aim of this thesis, as part of the FUNGRAPH project, sponsored by EPSRC, was to evaluate the evolution of damage in the nuclear graphite structure, and to identify atomic and mesoscopic relationship processes, which are dose and temperature dependent. The research process started with main objectives:

- To obtain proper working parameters for damage and orientation free collection when using TEM/EELS examination;
- To observe and compare the differences/similarities between different grades of virgin;

- To observe and compare the structure of different nuclear graphites irradiated with different parameters (e.g. temperature, dose)
- To analyse the change in the structure of nuclear graphite from virgin to after neutron irradiation;
- To compare electron and neutron irradiation damage on nuclear graphites;

Highlighting the importance of nuclear graphite integrity and following the main objectives, it seems that a study of the structural properties of crystallites and crystalline lattice is necessary (Chapter 3), which is the main topic of this thesis. In particular, this thesis tried to link findings obtained experimentally by different characterization techniques (**XRD**, **Raman Spectroscopy, TEM**, **EELS** and **SEM**), and to propose a model for the structural degradation of graphite which is dependent on temperature and irradiation dose. The above-mentioned techniques provide information ranging from the atomic scale to the nano- and micro-scale structure (XRD and Raman Spectroscopy), that can have a big influence on the macro-scale and therefore on the working life of a nuclear reactor.

X-Ray Diffraction **(XRD)** was used to analyse the changes of crystallites as a result of neutron irradiation dose, by providing means of L_a and L_c values, along with the lattice constants **a** and **c** (Chapter 5.1). This information was used in filling the gaps/or reinforcing the findings from EELS and Raman data. **Raman spectroscopy** was used to assess the degree of graphitization/order different nuclear graphites, by quantifying the I_D/I_G ratio, or FHWM of the G peak (Chapter 5.2). The Transmission Electron Microscopy (**TEM**) was used as a tool for finding information about the lattice structure (e.g. lattice constants **a** and **c**), and the crystallites orientation change within the lattice due to irradiation (Chapter 5.3.1). Electron Energy Loss Spectroscopy (**EELS**) was used with the aim to establish a correlation of the presence of defects due to irradiation (e.g. the possible change of the carbon atoms bond from sp^2 to sp^3 bonding), with the degree of order observed by Raman Spectroscopy (Chapter 5.3.3). The reason for using the Scanning Electron Microscopy (**SEM**) was to correlate the micro-scale and atomic scale results, for a better understanding of the evolution of nuclear graphite's structure from virgin to a neutron irradiated condition.

To minimize electron beam induced damage on the graphite by the electron beam, TEM and EELS were conducted at 80 keV. Other special calibrations were made in order to collect the EELS data correctly, without any misleading effects due to crystallites orientation dependence. These new studies are summarised in Appendix A.

Non-irradiated graphites were investigated and characterised, along with the corresponding irradiated analogue – irradiated with both electron (Chapter 4) and neutron irradiation (Chapter 5).

Nightingale has done an extensive work on the structure and properties of nuclear graphite summarised in his book published in 1962 [3], however since then there has been the development of new grade of nuclear graphite. The virgin graphite used in this work included an old type of graphite, PGA (Oldbury and Wylfa graphites – big grain needle coke graphites), the same graphite used by Nightingale The knowledge about these two nuclear graphites and their structure has a major importance in the development of new nuclear graphites, as they are the oldest nuclear graphite used to build the first generation of nuclear reactors in the UK, the Magnox reactors [12]. Their importance increased now because, after more than 30 years of heavy neutron irradiation, the reactors where they were used have been decommissioned, and the building material can provide valuable information on changes to all kind of graphite's parameters relative to long working time, including irradiation dose.

Besides the study of virgin graphites - PGA (Oldbury and Wylfa), NBG-18, IG-110 and Gilsocarbon (GILSO) - the research was completed by the addition of the newly developed graphites (PCIB and PCEA) which are considered for use in the IVth generation of nuclear reactors.

Data from the virgin graphites was directly compared with data from graphites that were neutron irradiated with different doses and temperatures. The differences and similarities of all these virgin nuclear graphites make possible the comparison and the extrapolation of their behaviour when irradiated in a nuclear reactor, and also lead to the development of a model of graphite behaviour irradiated at high temperatures and doses.

The electron irradiation and beam convergence studies were conducted in collaboration with Miss Helen Freeman, while Dr. Fredrik Hage helped in developing the script in Hyperspy, which facilitated the EELS data analysis. The neutron irradiation research was possible due to Dr. William Windes, from National Idaho Laboratory, US, who provided the irradiated materials analysed in this thesis.

Chapter 2 Literature review

2.1. Carbon: general considerations

Carbon is one of the oldest chemical elements, known from antiquity, and the most frequent element found in nature. As a chemical element, C, carbon is characterized by its atomic number Z = 6, and the atomic weight A = 12.011. Carbon contains about 98.9% of the isotope C^{12} with 1.1% of isotope C^{13}; natural carbon can also contain the radioactive isotope C^{14} [5,13].

2.1.1.Carbon allotropes

Carbon has its 6 electrons in a configuration $1s^2 2s^2 2p^2$ (Figure 2.1), with the four free valence electrons ($2s^2 2p^2$) available to be shared with other atoms. The combination of orbitals is called hybridization, and for carbon it can have 3 forms: sp^3, sp^2 and sp.

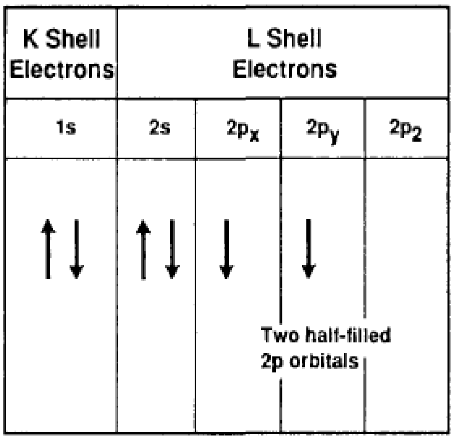

Figure 2.1 Ground state electronic configuration of carbon [14].

Carbon-carbon bonds can have different structures and strengths.

I. Diamond

One of the carbon allotropes that has exclusively sp^3 bonding is diamond. Diamond can have two forms: cubic (Figure 2.2 (a), the most common form, and more rarely (and unstable) a hexagonal form.

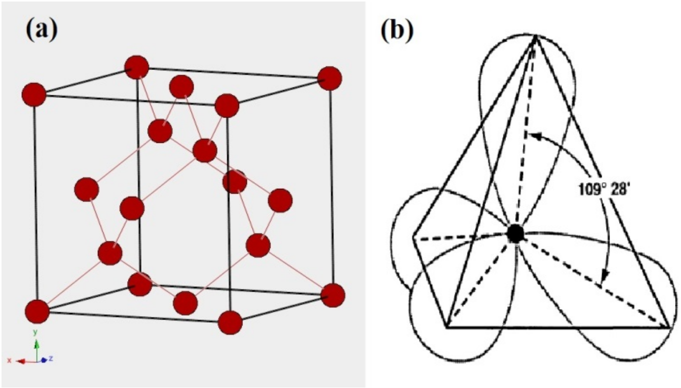

Figure 2.2 (a) Schematic diagram of the cubic diamond; (b) schematic representation of the diamond tetrahedron [14].

The most common electronic state in which carbon can be found is the **sp^3** hybridization form, in which each carbon atom is sharing 2s and 2p orbitals, forming a tetragonal structure (Figure 2.2 (b)).

The cubic form has 8 atoms in a cubic cell of dimension **a** = 3.56 Å: 4 atoms inside, and the other 4 atoms shared, 1/8 in each corner of the cube, and ½ on each face of the cube. The stacking layers of diamond have a sequence of ABCABC, after every third (111) plane the sequence is repeating. Diamond is a dense material known for its properties of high stiffness and hardness among all materials [14].

II. Graphite

The second type of hybridization that carbon can have is **sp^2** Figure 2.3 (b) In this case, carbon is bonding one 2s orbital with two 2p orbitals, leaving one 2p orbital free, giving birth to two sp^2 hybrid orbitals, which are in plane orbitals with an angle of 120 degrees between each other, and leaving the unbonded 2p orbital perpendicular to the hybrids. For the bonding between two carbon atoms where sp^2-sp^2 hybrids bond to each other, a **σ** bond is born, and where the free p orbitals are bonding to each other and **π** bonding exists, forming a double bond (σ+π).

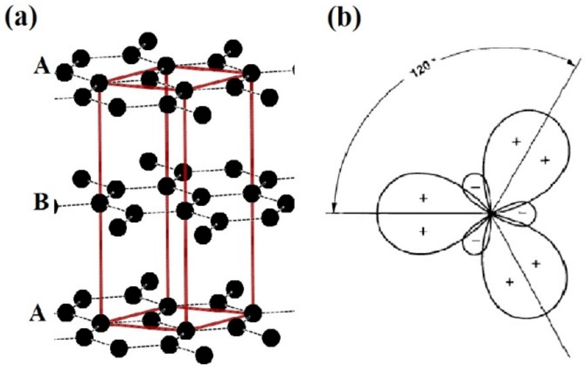

Figure 2.3 Schematic diagram of the (a) 3D graphite; (b) sp^2 hybrid [14].

The most famous allotrope that has exclusively the sp^2 bond is the hexagonal graphite. For graphite, the most common stacking sequence is the hexagonal ABABAB form giving rise to a hexagonal unit cell. Others may exist, however are uncommon – e.g. ABCABC form.

The unit cell, which makes the basal structure of hexagonal graphite, is defined by the second nearest neighbour atoms, for which the position is described by two equal vectors with a 60° angle in between. Every unit cell consists of four atoms. The basal plane has the lattice constant **a** = 2.46Å and the rule for **c**-axis vector that must be twice the length of the inter-planar distance, so the neighbouring planes do not overlap (Figure 2.4). Graphite's structure will be discussed in more detail later in this thesis.

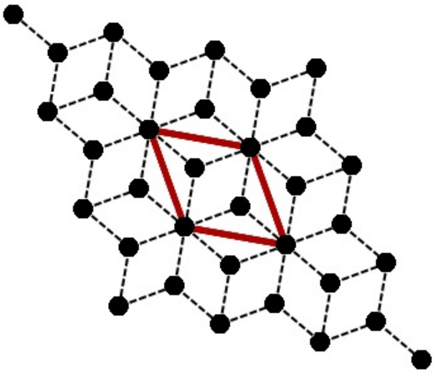

Figure 2.4 Representation of 2D graphite layer planes structure. Highlighted is red is the unit cell of graphite.

III. Fullerenes and C60

Other notable allotropes of carbon are the fullerenes, discovered in 1985 by Smalley & Kroto [15], and synthesised in 1990 by Kratschmer & Huffman [16], Their synthesis is done by the evaporation of a graphite electrode. Their structure is edgeless, and has the particular property of self-assembly into spheres (Figure 2.5 (b)). Fullerenes consist of pentagonal or hexagonal rings, for which case, depending of the number of rings, it has variable hybridization. The simplest fullerene structure is C_{20}, consisting of twelve pentagons and has an unstable sp^3 configuration. However, the most famous and stable structure of the fullerenes is the C_{60} (Figure 2.5 (c)), a structure which is made from a combination of (twenty) hexagons and (twelve) pentagons having both sp^2 and sp^3 hybridizations.

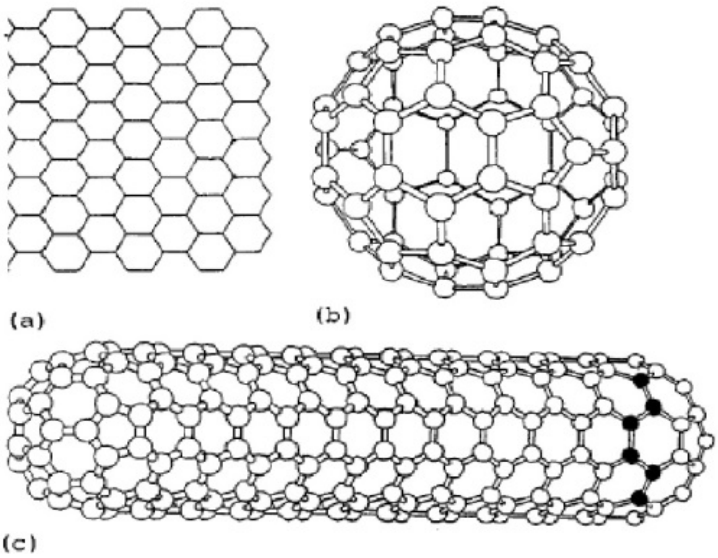

Figure 2.5 Schematic representation of C forms: (a) graphene sheet; (b) C60 fullerene and (c) single-wall nanotube.

The applications of fullerenes are wide, because of their properties of bonding with surfaces (but not to themselves), from electronics to other fields of science that need nano scale manipulation of the structure [17].

IV. Graphene and Nanotubes

If graphite is known to be a stack of layers in the ABABAB, the 2D form of graphite is the graphene sheet, which forms the 3D structure of graphite. In 1985 the term graphene was used the first time to define a single layer of graphite (Figure 2.5 (a)) and utilized as a modelling tool for systems using graphite, but it took almost 20 years (2004) for the graphene to be synthesized artificially in the lab as a single layer of material. Since then, the graphene has been intensively researched because of its unique chemical and thermal stability, high conductivity and low resistivity, flexibility, transparency and durability [18].

The tendency of graphene sheets to curve made possible the discovery of the carbon nanotubes in 1991. However, only after 1996 they were synthesised by laser vaporization of graphite, and since then, became one of the most intense researched fields. Carbon nanotubes are very close in structure to fullerene, being basically capped by half fullerenes (Figure 2.5 (c)) [17]. Depending on the way the graphene sheets are rolled up, they have varied mechanical, electronic, transport, and thermal properties which make them the subject of intensive research in different technological areas.

Graphene kept the researchers from many fields busy for the past 10 years, in order to identify all the capabilities of such flexible material. Being either metallic or semiconducting, the graphene can poses metallic properties in which the valence electrons can move freely, or by adding impurities a graphene can play the role of a semiconductor structure, in which the metallic or insulating properties can be manipulated,

V. Graphitising and non-graphitising carbons

A. Graphitising carbons – Graphite

The process of going through different steps of heat treatments and changing the structure from turbostratic into a more ordered graphitic structure is called graphitization.

According to Oberlin [19], for carbonaceous materials to graphitise this must commence with a small (<10Å) Basic Structural Unit (BSU), which then become aligned and parallel over larger areas. Starting from the carbonization of aromatic hydrocarbons (e.g. anthracene, naphthalene), by increasing the temperature, the remaining volatiles are gradually evaporated (~600℃) and a well-ordered structure is formed - the coke, a mixture of different cokes giving rise to coal-tar pitch [14].

After passing the carbonization temperature (~1200 °C), the structure is free from metallic impurities around 2000 °C with the slow transformation of the structure from turbostratic into a graphitic structure (Figure 2.6). After reaching 2200 °C the structure has already a crystallite size increased from 50Å to 1000Å, and by controlling further the graphitization process (pressure ~0.1 Torr, temperature >3000 °C) [14] a highly order graphitic structure can be obtained as it will be seen further on.

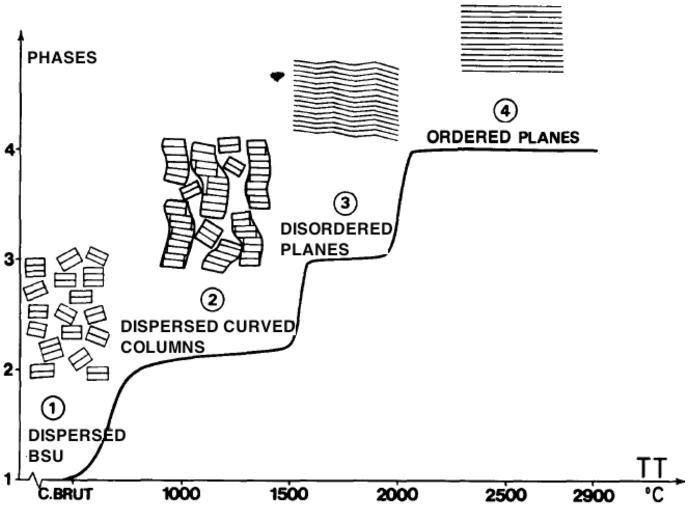

Figure 2.6 Schematic representation of the graphitization process [19].

B. Non-graphitising carbons - Glassy /porous carbon

There are a number of important forms of carbon which do not possess long range order.. Glassy or porous carbons are a type of disordered sp^2 structure, which are synthesised from pitch in reaction with O_2 or CO_2 at temperatures in the range of 800 °C - 1200 °C [14]. Considering their random structure, the properties of this material differ from the ones of amorphous carbon, and their porous structure makes them low density and isotropic materials. Their usages are mainly of a chemical nature: due to its chemical resistance being close to that of graphite, and they are employed in battery production or glass applications [14].

2.1.2. Graphite properties

After J.D. Bernal introduced the hexagonal crystal structure in 1924, graphite was known as a hexagonal, well-developed layer structure of carbon, in which the layers have certain order in stacking sequence [5].

Graphite crystal structure

The main peculiarities of hexagonal graphite are: a) the mobility of electrons in the hexagonal rings in the **a**-**b** plane formed by atoms spaced at 1.415 Å each with a strong chemical bonding of ~628 kJ/mol and b) the large spacing of 3.354 Å between carbon layers along the **c**-direction arising from weak van der Waals force of only 5.54kJ/mol (Nightingale 1962).

Graphite is defined by crystallites made from a multitude of unit cells arranged in a periodic order according to the symmetry rules. In the **a**-direction and **c**-direction, the crystallites are defined by their dimensions (or coherence lengths), L_a and L_c respectively (Figure 2.7).

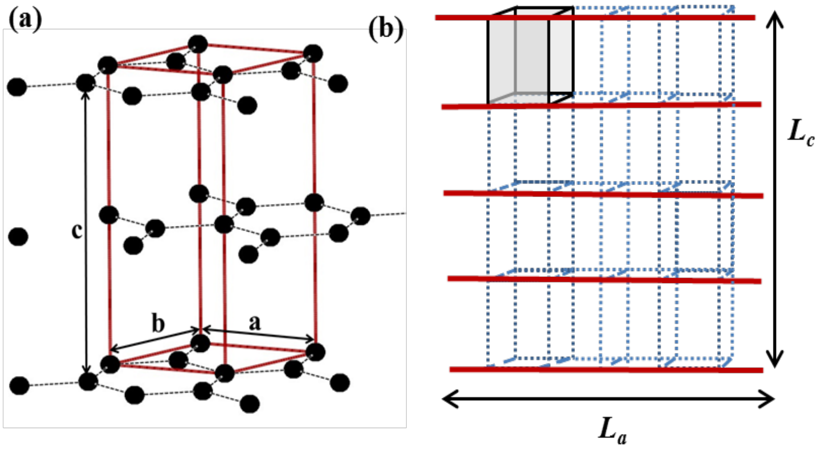

Figure 2.7 Schematic representation of: (a) single hexagonal unit cell of graphite and (b) the crystallite sizes - highlighted in grey is the unit cell of graphite.

The packing of crystallites, and the nature of materials from which the graphite is synthesised influence the overall properties of graphite, which are in Table 2.1

Table 2.1 Graphite (both synthetic –pyrolitic graphite and natural graphite) - general properties (values taken from different sources)

Properties	Graphite
Bulk density (kg ·m^{-3})	2180- 2270 (HOPG [20,21]) 2090 – 2230 (nat. graph. [22])
Electrical resistivity, (Ohm·m)	
ab direction	0.15 –0.25 (HOPG [23]) 1.2 x 10^{-6} (nat. graph. [24])
c direction	1.5-3.0 x 10^{-3}(HOPG [23])
Thermal conductivity,@25℃ (W· m^{-1} · K^{-1})	
ab direction	159 – 389.3 (HOPG [3]) 160 (nat. graph.[24])
c direction	2 – 3.5 (HOPG [3])
Tensile strength (Pa)	
ab direction	15 - 80 x10^{6} (HOPG [3,20]) 8 x10^{6} (nat. graph.[25])
c direction	-
Compressive strength (Pa)	
ab direction	20 - 200 x10^{6} (HOPG [23]) 7.3 x10^{3} (nat. graph [25])
c direction	-
Coefficient of thermal expansion K^{-1}	
ab direction	2.4 x 10^{-9} (HOPG [20])
c to grain	-

2.1.3. Types of graphite

Three main types of graphite exist: natural, pyrolytic and synthetic graphite. These three types differ by their characteristics and occurrences, as is seen below.

I. Natural graphite

This type of graphite is found naturally. It occurs as small disseminated crystalline flakes in the structure of magnesium and calcium rocks. The main characteristic of this structure is that it is very anisotropic, having only some small regions of ideal and structure. This perfect structure can be found near the defect (twist and twin boundaries) within a crystallite. Even so, following purification procedures (most of it annealing, in order to remove impurities) natural graphite can offer an appropriate material for fundamental studies being a good approximation to ideal single crystal graphite.

II. Pyrolytic graphite

Produced by a chemical vapour deposition (CVD) procedure, pyrolitic graphite is formed by carbonization of a solid carbonaceous material: coal–tar pitch, petroleum fractions or polymers.

The manufacturing procedure is as follows: within a room some poly-aromatic hydrocarbons (e.g. methane) are heated at elevated temperatures (>500℃) where the C-H bonds are split and the hydrogen is removed. Through the heating process, some hydrocarbons undergo an intermediate stage at temperatures >400℃ called *mesophase*, where the crystals have a lamellar arrangements with the long axes (the **c**-axis) laying down parallel to each other and develop van der Waals forces which bonds them together encouraging the alignment. This is the stage where the *pre-cokes* are formed. The most common deposited pyrolytic material, which has a highly oriented, perfect and impurity free structure, is HOPG (Highly Oriented Pyrolitic Graphite).

HOPG has become a good substitute to mimic the natural graphite in both research and industry.

III. Synthetic graphites

Synthetic graphite can be either moulded or extruded; the first moulded graphite was obtained in 1896 to be used as electrodes.

In manufacturing synthetic graphite, the selection of the raw material is vital in obtaining good properties and quality products, and in determining the costs. Both the size of the coke particles, and the degree of carbonization of the pitch are important for the grade quality of the synthetic graphite as it will be shown later on in thesis. The main parts of synthetic graphites are: the filler, the binder, and the additional impregnants and additives.

The filler particle is generally derived from cokes the first choice in most applications being the petroleum cokes. As a raw material, it is a pure solid carbon at room temperature, with a high degree of porosity characteristic of all the petroleum-derived materials. The filler particle is also the most important component in the synthetic graphite, as its parameters influence the grade of the resulting graphite (e.g. needle coke or isotropic coke) [14].

The second most important component of the synthetic graphite is the binder, made most of the time from coal-tar pitch (a distillation of coal), a brittle and glassy material.

Starting from solid hydrocarbons as raw materials, passing through different stages of heat treatment, and ending at high temperatures (>2800℃), the final product has some important properties (e.g. low neutron-absorption cross section, high scattering cross section, high temperature resistance etc.). These outstanding properties made synthetic graphite the perfect candidate for military purposes, in particular nuclear graphite, which will be discussed further.

2.2. Nuclear graphite (NG)

The graphite used in nuclear reactors (namely the nuclear graphite) is of high purity synthetically obtained graphite: it has a polycrystalline structure with filler particles kept together by a binder [3]. When making nuclear graphite, it is very important to consider the reduction of the impurities present in the material [3], as a large fraction of impurities can change important physical properties [26].

2.2.1. How is it made?

Nuclear graphite is a highly pure (~99.8% purity) mainly produced from coal-tar pitch and petroleum coke particles which by passing consecutive and well established manufacturing procedure can "achieve a higher degree of crystallinity than other materials" [3].

The coke is the primary material that forms the body, and the pitch is used as a binder. The procedure is complex (Figure 2.8) and consists of multiple heating treatments until the crystal growth takes place. Most of the time, the filler must be added in order to increase the density of the resulting porous material [8].

One of the most important steps in manufacturing nuclear graphite is the mixture of different phases of carbon. The quantity of filler (the petroleum coke) compared to that of the binder (the coal-tar pitch) is well defined by the manufacturer: about 30 parts binder for 70 parts filler [27]. The manufacturer has to consider that if the binder is too low, then the final material will crack easily because of the presence of high strain inside the filler; if the percentage of binder is too high, than the final material will have bad structure with inappropriate properties (one of most important is low thermal resistance to high irradiation temperatures) [28]. The density and the dimension of the grains are influenced also by the "packing" of the graphite, which can be either done by *extrusion* or by *isostatic moulding*. The manufacturing methods are influencing also the geometric form of the grains and the isotropy of the ending material, in the way that the extruded graphite has a needle shape grain and is anisotropic or semi-anisotropic (e.g. PGA like graphite), while the moulded graphite has more a spherical grain size and is isotropic (e.g. Gilsocarbon graphite).

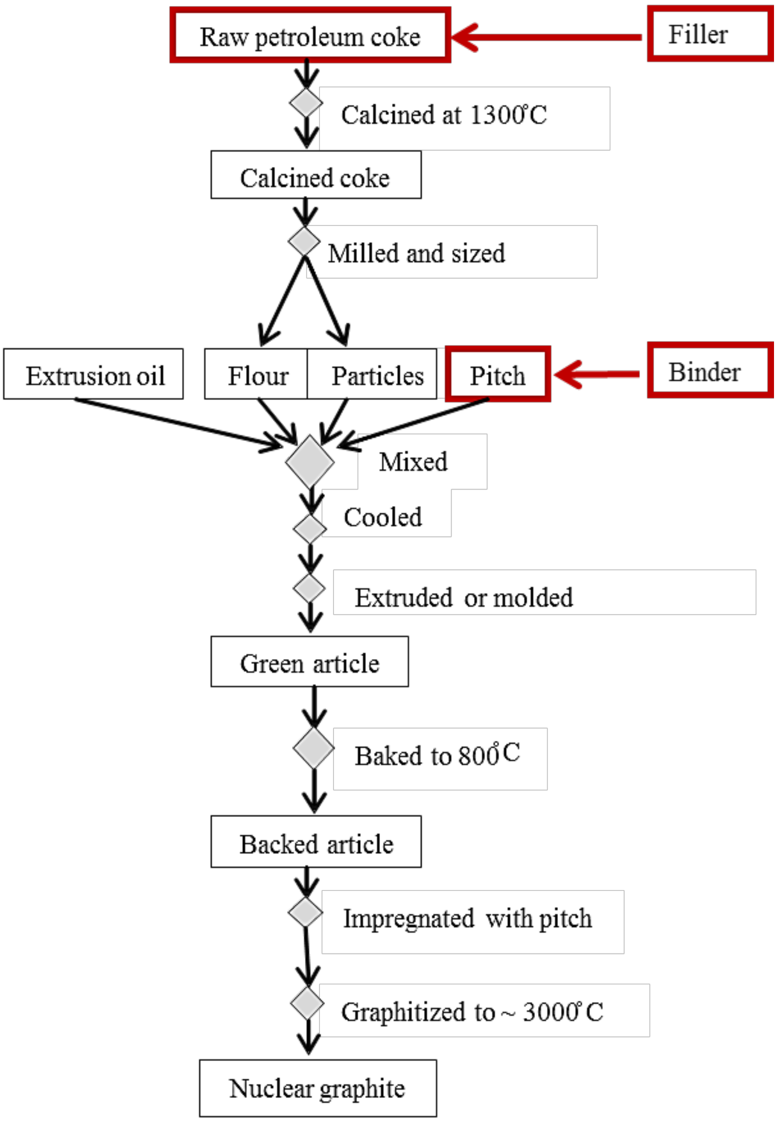

Figure 2.8 Process of manufacturing nuclear graphite.

After suffering several baking and impregnation procedures, the final stage is finishing with a last procedure - the graphitization, a process that takes place ~ 3000^0C. The importance of this step is crucial in establishing the crystal growth and maximizing the internal order. On reaching this temperature, the material is composed only from carbon, having all of the physical properties well established (Hall coefficient, magnetic susceptibility, electrical and thermal conductivity etc.) [3].

2.2.2. Types of NG

Pile grade A (PGA) graphite is needle-coke graphite produced by extrusion, being anisotropic, and has a grain size (filler domain) of ~1mm. This type of graphite was used in some UK designed reactors under the name of Magnox reactors. Currently in UK only Magnox Wylfa is still functional, the old Magnox Oldbury being shut down in 2012.

Gilsocarbon (GILSO) graphite is produce by using Gilsocoke and compared to PGA the filler grains are spherically shaped with an average grain size of ~0.5mm. Mainly used in the second-generation British Advanced Gas-Cooled reactors (AGR), after the first generation of Magnox reactors which used PGA, this graphite is formed by a moulding process leading to a near-isotropic material.

IG-110 graphite is a fine-grained product manufactured by Toyo Tanso in Japan. This graphite is petroleum coke isotropic graphite formed by isostatic pressing with an average grain size of 5-50µm and it is used in HTGR reactors in Japan.

NBG-18 graphite is produced in Germany by SGL and is formed by vibrational moulding, which makes it isotropic. It has a medium grain diameter of ~1.6mm with a filler particle made from pitch coke. NBG-18 is used the Pebble Bed Modular Reactor (PBMR) in South Africa.

PCEA is anisotropic new medium grained graphite with a needle grain size of 360-800µm produced by extrusion and using petroleum coke source.

PCIB as well as PCEA is a newly made material with an ultra-fine grain size produced by an isomolding procedure, which makes it isotropic, and having as a precursor petroleum coke.

After years of research PCEA and PCIB candidate materials were selected as candidates for the new High Temperature Reactors (HTR) [29]. However, after intense property characterisation, a change in plan occurred and NBG-18 and PCEA were chosen for the US Next Generation Nuclear Plant (NGNP) in the building of high temperature gas-cooled reactor (HTGR) with a large graphite core [30].

2.2.3. Microstructure and properties of NG

As was mentioned in above, the grain shape and size of the graphite particle depend almost entirely on the filler particle and the manufacturing process. For the oldest nuclear graphites PGA and GILSO, the particles are very distinctive, in size and shape. In PGA the filler particle (~1mm) is long and needle shaped with pores along the long axis of the needle (Figure 2.9 (a)), whereas is GILSO the filler particle (~0.5mm) has an onion shape with pores that follow the spherical shape (Figure 2.9 (b)).

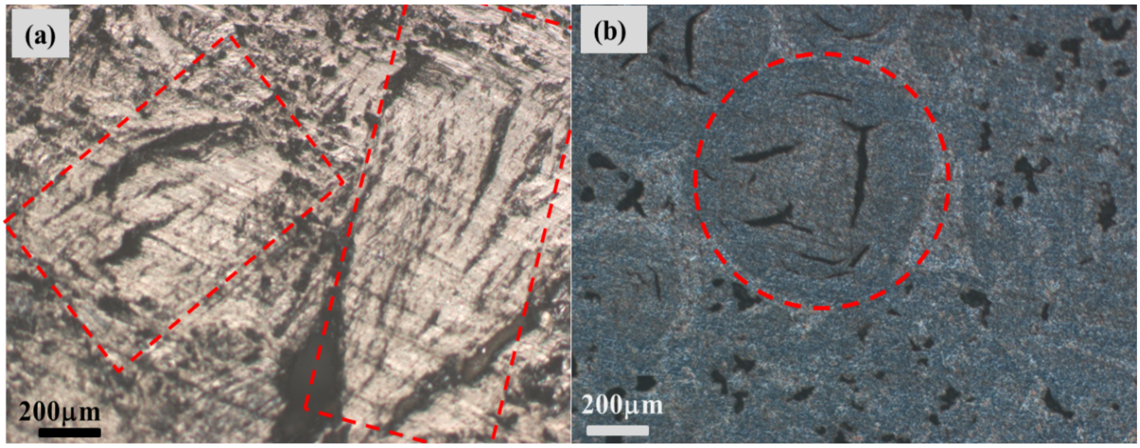

Figure 2.9 Polarised light micrographs showing: (a) long filler particle of PGA and (b) onion-like filler particle of GILS; highlighted in red are the filler phase.

Nightingale[3] was reported that for the majority of the petroleum coke graphites the distribution of pores, in both filler and binder phase, is in the 20-300Å range,. He also suggested that the longer the crystallite size, the smaller the pore volume is. A schematic diagram of the microstructure of needle shape nuclear graphite is shown in Figure 2.10.

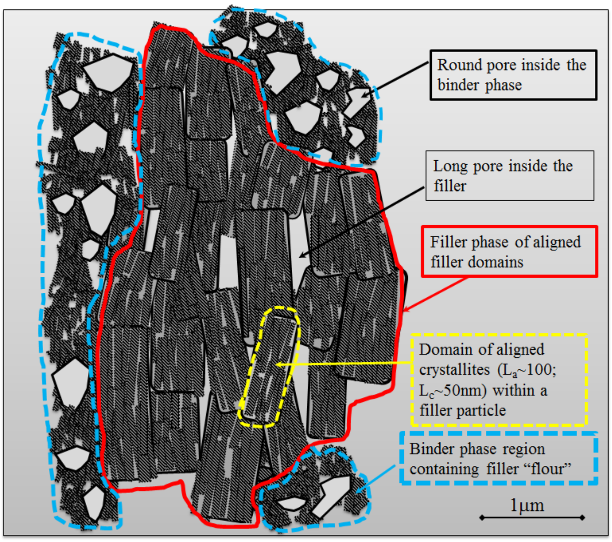

Figure 2.10 Schematic representation of needle like-shape NG with structural units and nomenclature.

After more than 50 years of improvement made in manufacturing nuclear graphite, Kane *et al.* [31] reported the discovery of 3 new graphites: IG-110, NBG -18 and PCEA shown in Figure 2.11.

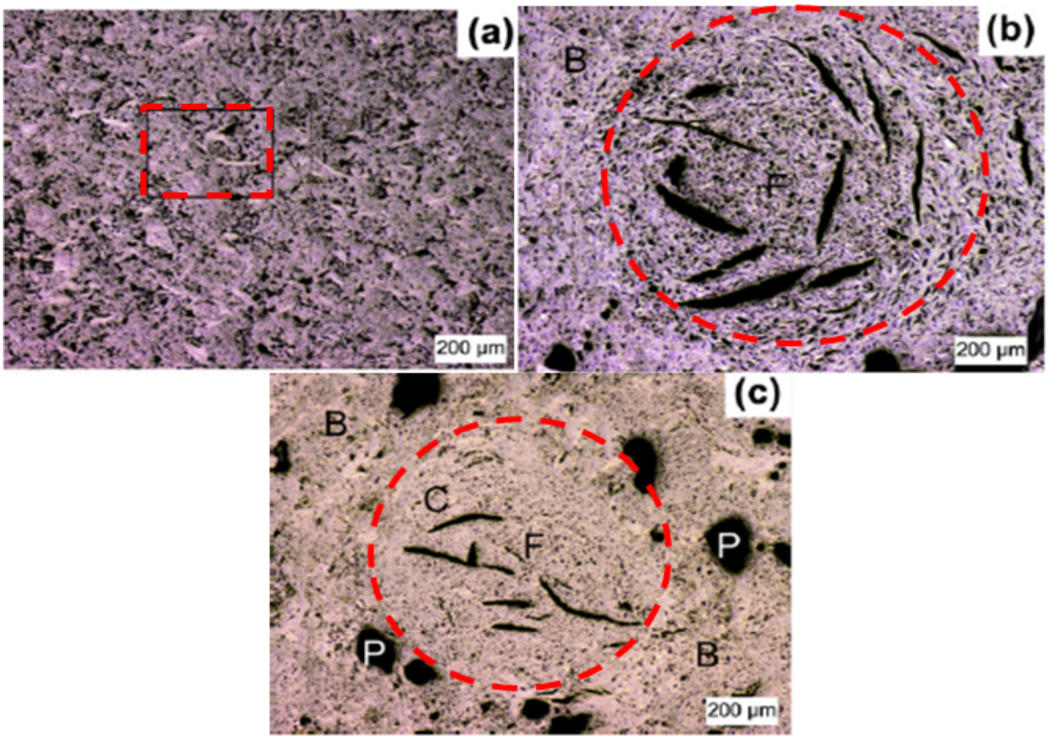

Figure 2.11 Micrographs showing: (a) fine grained IG-110; (b) NBG-18 onion-like filler particle and (c) PCEA filler particle; with : B-binder, C-cracks, F-filler and P-pores after Kane *et al.* [31]; highlighted in red is the filler particle.

Kane *et al*. observation revealed that: 1) IG-110: with a density of 1.925 g/cm^3 has a fine needle shape with the particle length of 27 ± 2μm; 2) NBG-18 with a density of 1.938 g/cm^3 has a round medium filler particle diameter of 360 ± 25μm ; 3) PCEA with medium size filler particle of variable shape, both round and needle like , has the measured density of 1.896 g/cm3 with an average size of the filler particle of 137 ± 12μm .

As can be seen from **Table 2.2** with general properties of various types of nuclear graphites, the new improved neutron graphites have all higher density than the previous generation, PGA and GILSO. This property of having a more dense material has a major importance as it brings higher moderation of the neutron flux.

Table 2.2 Representative properties of some Nuclear Graphites

Property-units	PGA[1]	GILSO[1]	IG110[1]	NBG-18[2]	HOPG[3]
Filler	Petroleum coke	Gilsocoke	Petroleum coke	Pitch coke	
Bulk density- (kg·m-^{3})	1740	1810	1780	1850	2250 - 2260
Electrical resistivity, (ohm·m)			-		
∥ to extrusion	7.34 x 10^{-6}			-	0.15 – 0.25
⊥ to extrusion	9.40 x 10^{-6}	9 x 10^{-6}			1.5 - 3.0 x 10^{-3}
Thermal conductivity- (W·m^{-1} · K^{-1}) @20 °C					
∥ to extrusion	227.34	131	78		159 – 389.3
⊥ to extrusion	138.16			-	2 – 3.5
Tensile strength - (Pa)			25 x 10^{6}		
∥ to extrusion	17 x 10^{6}	17.5 x 10^{6}		24 x 10^{6}	15 - 80 x10^{6} [3,20]
⊥ to extrusion	11 x 10^{6}				
Compressive strength -(Pa)					
∥ to extrusion	27 x 10^{6}				
⊥ to extrusion	27 x 10^{6}	70 x 10^{6}	77 x 10^{6}	77 x 10^{6}	
Coeff. of thermal expansion K^{-1} (20-120°C)					
∥ to extrusion	0.9 x 10^{-6}		4.1 x 10^{-6}	-	
⊥ to extrusion	2.8 x 10^{-6}	4.3 x 10^{-6}			2.4 x 10^{-9} -

---

[1] Representative data collected from different sources, e.g.[3,53]

[2] [169]

[3] standard data for HOPG[23] [170,171] [21]

2.2.4. Applications of NG

The low neutron absorption cross section made synthetic graphite the first material used for military purposes and nuclear reactors (hence the name **nuclear graphite**), as a moderator and reflector, but also as a fuel-channel sleeve, thermal column and fuel matrix (Figure 2.12) [3].

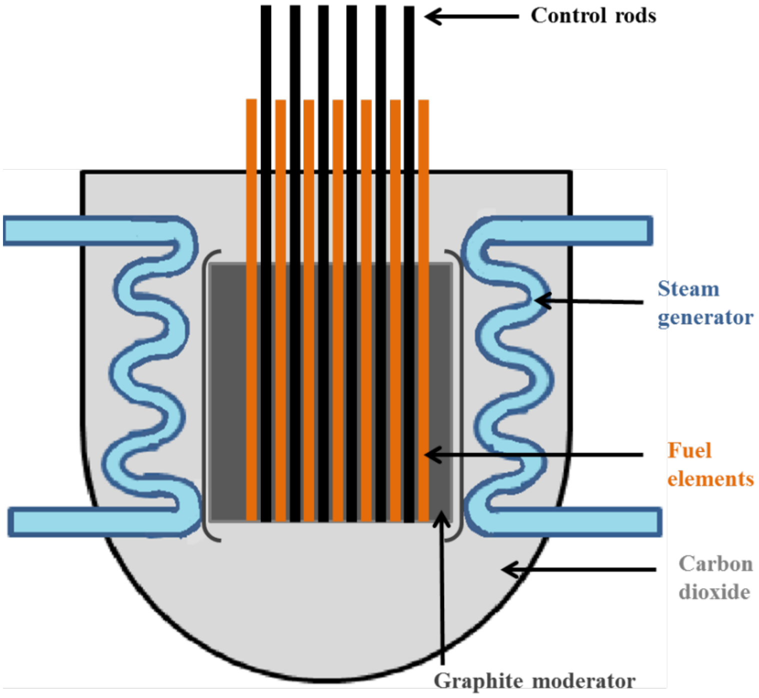

Figure 2.12 Schematic design of a gas-cooled reactor.

To explain the reflector role of graphite it must be said that it is used as a cladding of the core of the reactor. This shield is used in order to keep the neutrons inside, and not to permit any interaction between them and the coolant, which could give rise to extra heat by returning unnecessary neutrons into the core.

The most important application of graphite is as a moderator. Graphite is used in the core of the reactor, where the fast neutrons suffer collisions with the surrounding wall. By losing only a part of their kinetic energy they are scattered and return to interact with other existing ^{235}U atoms and the fission processes is continued. If the moderator would not have a low neutron absorption cross section, the neutrons would be absorbed by the material and halt the fission reaction. However, if the moderator was made from heavy nuclei, each collision would reduce the kinetic energy of neutrons to minimum and when returned into the core, the probability of interaction with the ^{235}U nuclei would be lower therefore halting the fission process [7,32,33].

Graphite is used (and has been used) in couple of graphite moderated reactors worldwide, of which is worth mentioning:

- the UK MAGNOX and AGR as CO_2 gas cooled reactors working at temperatures lower than 400 °C, using as graphite moderators PGA and GILSO; MAGNOX is part of first generation of nuclear reactors while AGR is from the second generation
- the Natural Uranium Graphite Gas (UNGG) reactor is a First Generation French gas cooled reactor, working at temperature in the range 330-400 °C [34]; the UNGG design was also used in Spain.
- the RBMK is a water cooled Russian design reactor from Generation II of nuclear reactors, using graphite as moderator [35].
- the High Temperature reactor (HTR-10) is a helium cooled prototype reactor built in China and it is working at higher temperatures (750-900 °C); This reactor is a new reactor design, using IG-110 graphite as moderator , and is part of the next generation nuclear plants working at high temperatures – High Temperature Gas-cooled reactor (HTGR) - Generation IV [30].

2.3. Irradiation of NG

2.3.1. Neutron Irradiation

When two particles collide, they experience momentum and energy transfer, ΔE, the level of which depends upon the mass ratio between the target (carbon) atom and the incident particle. The atomic displacement rate, measured in displacements per atom (dpa), is dependent on the kinetic energy of this incident particle, E_i. For neutrons (mass = 1), Eq. 2.1 tells that in an elastic collision with a carbon atom, where atomic mass, A = 12, the transfer of energy from the neutron to the carbon atom is $0.28E_i$ [36].

$$\Delta E = \frac{4A}{(A+1)^2} E_i \qquad \text{Eq. 2.1}$$

According to calculations by Thrower and Mayer [37] a 1 MeV electron (much lower mass) and neutron produce 1.6 and 500 atomic displacements respectively. Cascades of atomic displacements are the most common route for large scale structural disturbances.

I. General Process

The impact of irradiation on graphite can be seen in the changing of its properties. This is because of the “Wigner effect” that happens as a result of radiation damage: a very high energy particle does permanent damage to the graphite by causing the displacement of carbon atoms (Figure 2.13) which start to move into the crystal lattice.

The first displaced atom is referred to as the primary knock-on atom (PKA), which travels through the lattice and, if the energy is high enough (Eq. 2.1), it can displace further atoms. They behave as secondary knock-on atoms (SKA), and continue to cause atomic displacements until the energy has been dissipated throughout the structure (Figure 2.13), although some movements are present until the thermal equilibrium is reached. Models have been created to calculate the number of atoms involved in cascade events of varying energy [38–40].

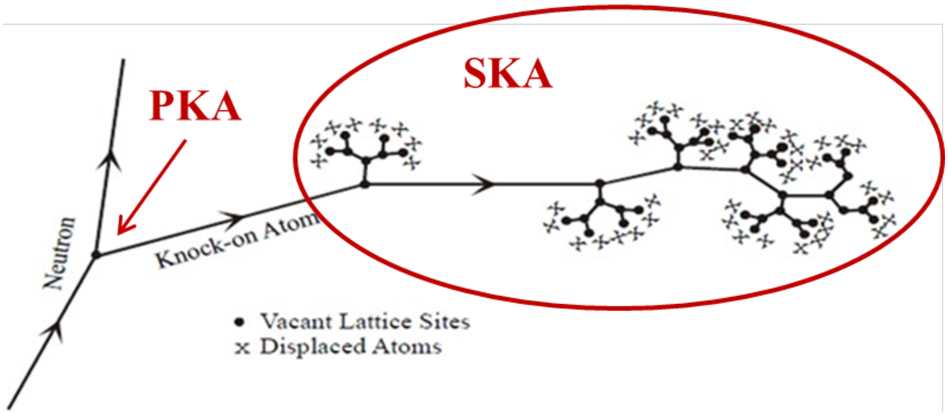

Figure 2.13 Schematic representation of the mechanism of atoms displacement due to high energy neutron.

The relatively wide spacing of graphite's lattice planes results in low density collision cascades, and the low neutron dose rates (10^{-7} dpa s^{-1}) and high temperatures (~450 °C) in the nuclear reactor allow this cascade damage to partially anneal between cascade events [8]. This effect has the result of creating interstitials between layers. Associated with the atoms that formed the interstitials, the presence of vacancies is obvious [8,41].

II. Energy transferred

Interstitial and vacancy defects created during radiation damage can behave independently or coalesce into clusters and gradually deform the crystal lattice resulting in both chemical and physical changes. When the Wigner effect happens, many displaced atoms (interstitials) coalesce and give rise to localised energy, referred to as the Wigner energy. Damage accumulation at temperatures below 200 °C increases the Wigner energy and heat content due to a lack of diffusion. In an adiabatic environment the Wigner energy is discharged causing a sharp increase in temperature and with ignition can result in fire [7]. This poses a serious risk for low-temperature nuclear reactors, and was the indirect cause of the Windscale nuclear accident of 1957. To avoid such risks, and relieve stress within graphite blocks, the reactor core can be engineered to encourage dissipation of the Wigner energy. By using temperatures around 900 °C in the Generation IV graphite moderated Very High Temperature Gas Reactors to encourage energy dissipation, the problem is addressed. However, long term exposure to a high temperature environment (> 400 °C) gives rise to creep, involving dimensional change of components when under load.

At temperatures similar to those of a nuclear reactor (~400 °C), the effect of annealing significantly reduces the damage rate. It is widely agreed that single vacancies become mobile at 100 – 200 °C, whereas interstitial atoms become mobile at temperatures of 500 °C [42,43].

III. Models proposed for defect migration

In the past years, several models were proposed for explaining the movement of defects inside the nuclear graphite. These defects take the form of interstitials and vacancies and are the result of neutron irradiation. Two models will be discussed, one proposed by Bacon and Warren (A) in 1956 [10], and the other introduced by Heggie *el al.* (B) in 2010 [11].

A. Bacon & Warren model for defect migration

The model proposed by Bacon and Warren [10] had as a starting point, the idea that the broadening of the X-ray diffraction peaks, observed in neutron irradiated graphites, is due not to the random distribution of localized displacements but to a distribution of grouped interstitials produced with regularity after a specific number of layers.

During irradiation, an interstitial or a group of interstitials (black dot in Figure 2.14) arriving at the P position will cause another new interstitial arriving at Q’, which will move to position Q to minimise the distortion of the lattice.

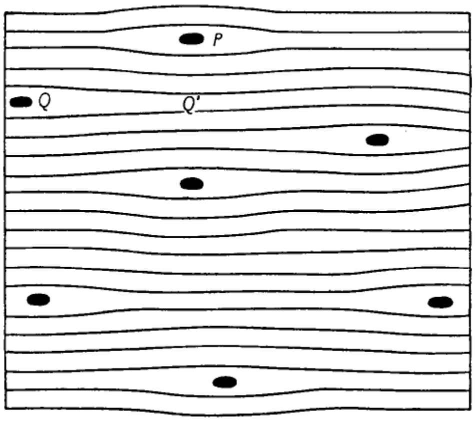

Figure 2.14 Schematic representation of interstitial increasing the space between layers, proposed by Bacon & Warren for radiation-damaged graphite [10].

The idea was that once the damage has accumulated with increasing exposure, the interstitials diffuse along the layer planes and combine with each other (proposed also by Kelly [44]). In time, the groups tend to be so big that is too difficult to anneal and dissociate, and they are basically forming extra sheets. Bacon & Warren also suggested that the vacancies do not have the same behaviour as interstitials.

B. Heggie's model for defect migration

Different from the previous model, Heggie *et al.* [11] adopted a model that takes in account the shear between planes of graphite. According to Heggie, the traditional model, which blames the dimensional changes on the aggregation of interstitials atoms, does not have any evidence to support the theory.

In the new model, basal plane dislocations are considered to cause the basal

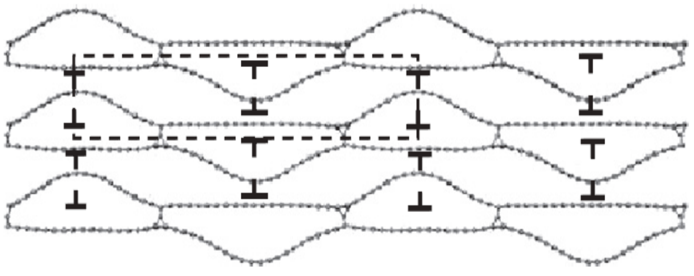

Figure 2.15 Schematic representation of buckled graphite of which layers are held. together by spiro-interstitals, the dislocations being represented by $\perp$ symbol [11].

planes to shift and are seen like line dislocations and not loop dislocations, as evoked in the old model. Through this model another type of defect is introduced, the spiro-interstitial. Below 250^0C when a shorter layer is bonded in two places to a longer layer by these spiro-interstitials, the longer one tends to buckle (Figure 2.15).

For higher temperatures, it is predicted that if two edge dislocations from in neighbouring planes of opposite sign interact with each other, buckling can occur and this is how the "ruck and tuck" defect comes up (Figure 2.16).

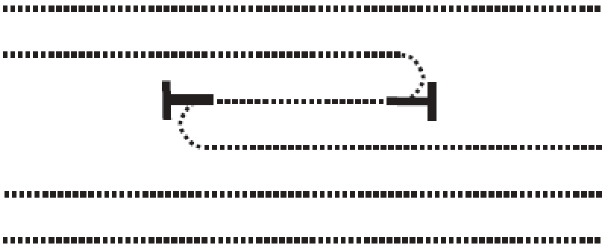

Figure 2.16 Two basal edge dislocation moving toward each other [11].

I. Microstructure changes due to neutron irradiation

Since 1940, consistent work has been done in researching nuclear graphite behaviour due to neutron irradiation. However, the researchers put more weight on property change, and not on the microstructural changes, which are influencing mechanical and material properties [45].

Since 1963, by conducting TEM investigations (Transmission Electron Microscopy) Thrower reported the different behaviour of neutron irradiated graphites (most of the time pyrolitic graphites) when changing irradiation parameters. His investigation revealed cracks present in the structure of single crystal graphite when irradiated at 3 x 10^{24} $n \cdot m^{-2}$ at 200℃, but not present on higher irradiation doses [46], contradicting Simmons and Reynolds who stated that the cracks are close at all irradiation temperatures. In 1964, the same author reported a variation of defect accumulation [47] with the presence of impurities (boron) at different irradiation parameters, especially increasing the temperature and preheating in different environments (Figure 2.17). Following the same trend in 1968, he made a correlation between defect nucleation and crystal perfection, suggesting that the interstitial nucleation is happening around twist boundaries giving rise to interstitial loops , but without creating staking fault defects [48]. In 1973, Thrower *et al.* [49], investigated several pyrolitic graphites irradiated with doses between 2.4 x 10^{24} n·m^{-2} and 5.2 x 10^{25} n/m^2 at high temperatures (up to 1450 ℃), and showed that the crystallite size has an influence in healing the defects with annealing.

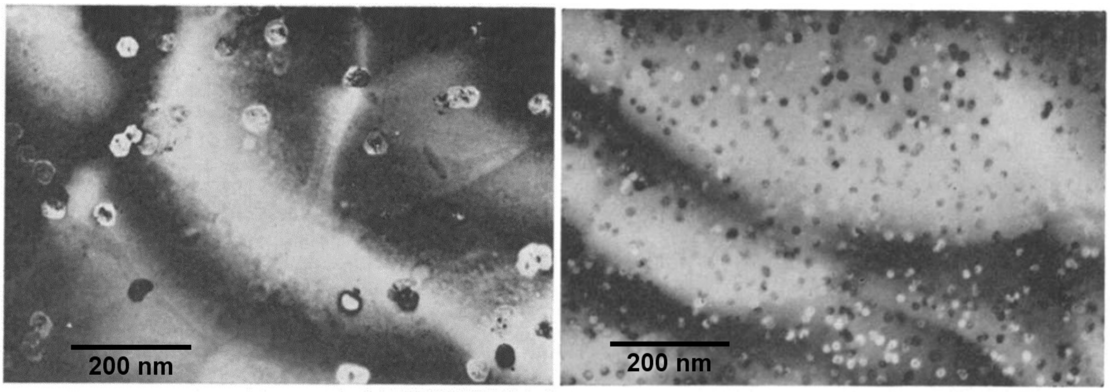

(a) pre-heated in vacuum at 1500° C – dose 2.7 × 10^{20} n/cm^2. 80 000 ×

(b) pre-heated in argon at 3000° C – dose 0.7 × 10^{20} n/cm^2. 80 000 ×

Figure 2.17 Micrographs of single crystal natural graphite showing the increase in impurity nucleation with different irradiation parameters: (a) preheated in vacuum and (b) preheated in argon environment, before irradiation [47] .

In 1990 Niwase *et al.* [50] using Raman spectroscopy, observed a correlation between the irradiation of the graphite and the loss of the atomic order (amorphization). The observations were made for a dose in the range of 0.1 - 1dpa at 200 ℃ by following the increase with irradiation via the full width half maximum (FWHM) of the G peak from Raman. In the same year Tanabe *et al.* [51] reported not an amorphization process, but a decrease in size of the crystallites due to neutron irradiation, at a dose in the range of 1.4 x 10^{23} n/m^2 - 1.9 x 10^{24} n/m^2 (corresponding to 0.14 - 1.9 dpa) and the same temperature of 200 ℃. Tanabe statement was reinforced with the correlation of the Raman results and the TEM findings (both electron diffraction and imaging).

After more than ten years, Niwase *et al.* [52], duplicated Tanabe *et al.* experiment, and following irradiation, observed that even though, the Raman spectra of irradiated HOPG showed signs of a disordered structure compared to virgin HOPG, although the high resolution TEM showed little or no damage. Niwase explained this finding by the ratio of the D and G peaks (I_{1355}/I_{1580}) being influenced not only by the crystallite size, but also by the presence of basal plane defects (interstitials or vacancies) due to irradiation. The same author proposed a correlation between point defects, TEM images and Raman spectroscopy (Figure 2.18).

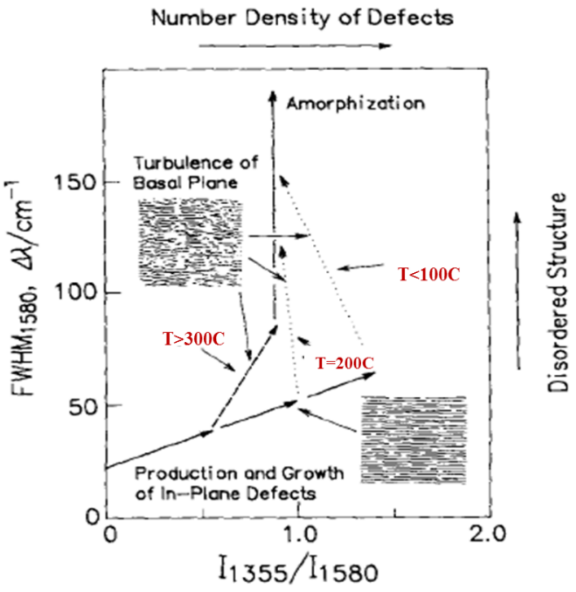

Figure 2.18 Schematic drawing of the change in FWHM of 1580 cm^{-1} and intensity ratio of I_{1355}/I_{1580} on irradiation.

During the years B.T. Kelly has done intensive work on characterising the properties of neutron irradiated graphite especially dimensional changes. In 1993, Kelly [53] , studied the behaviour of two of the most common nuclear graphites, PGA and GILSO under fast neutron irradiation. In his paper, he introduced two parameters in order to characterise the evolution of crystallite dimension (X_T) and the pore accumulation (F_X) due to neutron irradiation:

$$F_X = R_X(S - 0.05)^2 \qquad \text{Eq. 2.2}$$

$$X_T = \left(\frac{\Delta L_c}{L_c} - \frac{\Delta L_a}{L_a}\right) \qquad \text{Eq. 2.3}$$

Where $\Delta L_c/L_c$, $\Delta L_a/L_a$, are the dimensional changes of the crystallites in the **c** and **a** dimension, R_X is the XRD orientation factor, for PGA at 2200 ℃ being 0.2 and 0.4, parallel and perpendicular to extrusion, respectively and S is the crystallite shape change.

Kelly's finding showed an absolute correlation between the crystallite dimensional changes and the pores formation (Figure 2.19).

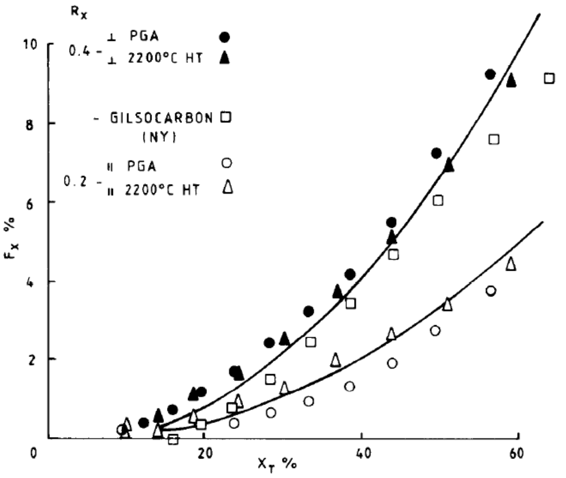

Figure 2.19 Fitting of pore generation as a function of crystallite size dimension (X_T) at an irradiation dose >10^{19} n·m^{-2}and 600C.

It will be seen further on that, the crystallite size change is a very important factor in determining the property change.

II. Property changes following neutron irradiation

Different property data is found between virgin and irradiated graphite. These changes are a function of irradiation parameters, such as dose, temperature and also the time of irradiation. It is still unknown with precision, which factor is more influential, and at what exact time failure will occur. The parameters studied were chosen because they have a direct influence on the working lifetime and failure of a nuclear reactor. Although the experiments were not done on the same type of nuclear graphite, almost all used HOPG as reference material. This is considered to be the most perfect polycrystalline graphite, which has similar structures and properties to nuclear graphites used in the working nuclear reactors, but for which the cost and the time effectiveness do not make it a good candidate for massive manufacture quantities.

The most common data found in the literature is on: irradiation-induced size effect (so called dimensional changes estimated by crystallite change in dimension from XRD), Young's modulus [54,55], coefficient of thermal expansion (CTE), thermal conductivity [56], and creep coefficient. Between all of these, the data for dimensional changes is more abundant and detailed [41,44,57–61]

A. Dimensional changes

The point on which results agree is that the changes are in directly related to the direction of orientation and the character of the deformation. It is observed that as a result of irradiation, there is an expansion in the **c**-direction (direction of the crystal with the stack of planes perpendicular to the extrusion direction), while in the **a**-direction (direction of the crystal with the stack of planes parallel to the extrusion direction) shrinkage was observed.

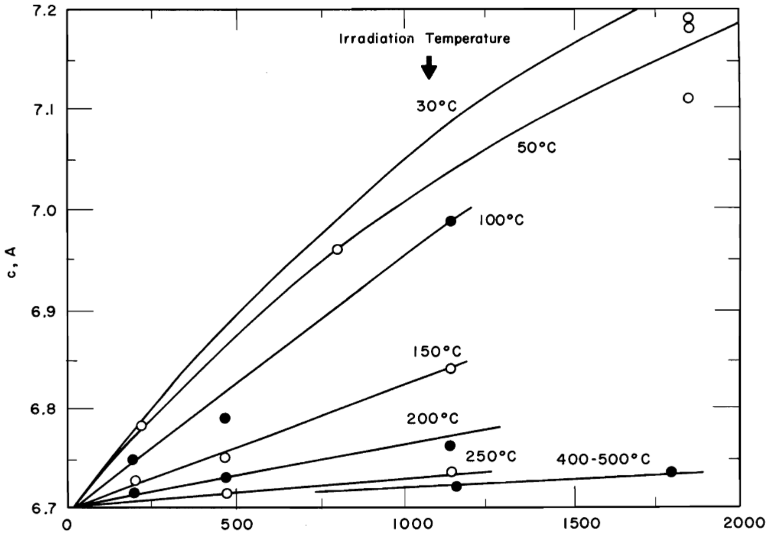

Figure 2.20 Expansion of c direction as a function of neutron flux at different temperatures (1 Mwd/At represents the thermal energy output for one tonne of nuclear fuel produced by a flux of 3.5 x 10^{20} n·m-^{2} in the reactor, corresponding to 3.1 x 10^{23} displacement/m^{2}) [3].

Nightingale who produced one of the most remarkable bodies of work in the field of nuclear graphite, stated that *dimensional changes* are correlated with irradiation and with temperature [3]. He conducted experiments at room temperature and above, and reported that the magnitude of **c**-dimension expansion decreased with increasing temperatures (Figure 2.20), observation reported and completed by other researchers, as it will be seen further on.

Changes in dimension related to dose and higher temperatures than room temperature were reported [57]. Supposing that in nuclear graphite, the crystallites align with the **a**-axis parallel with extrusion direction, and the **c**-axis perpendicular to the extrusion direction, the conclusion of different studies concerning dimensional changes was that irradiation at temperatures lower than 600 °C exhibit a change in both directions, perpendicular and parallel with extrusion directions, by shrinkage (Figure 2.21).

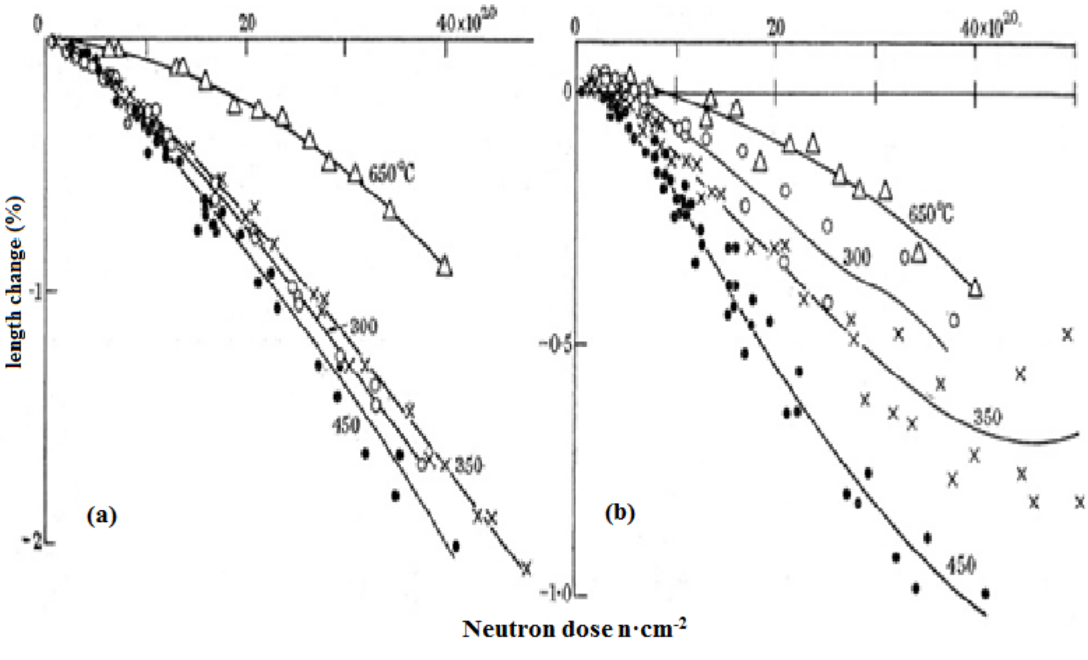

Figure 2.21 Dimensional changes induced in PGA by neutron irradiation in the temperature range of 300 – 650 °C: (a) parallel to extrusion – a-axis; (b) perpendicular to extrusion – c-axis [57].

Above ~600 °C, when it is thought saturation occurs, the magnitude and the behaviour of dimensional change, presents different characteristics,. It was observed that at higher temperatures than 600 °C the shrinkage in the **a**-direction is continued, while the **c**-direction starts to swallow (Figure 2.22).

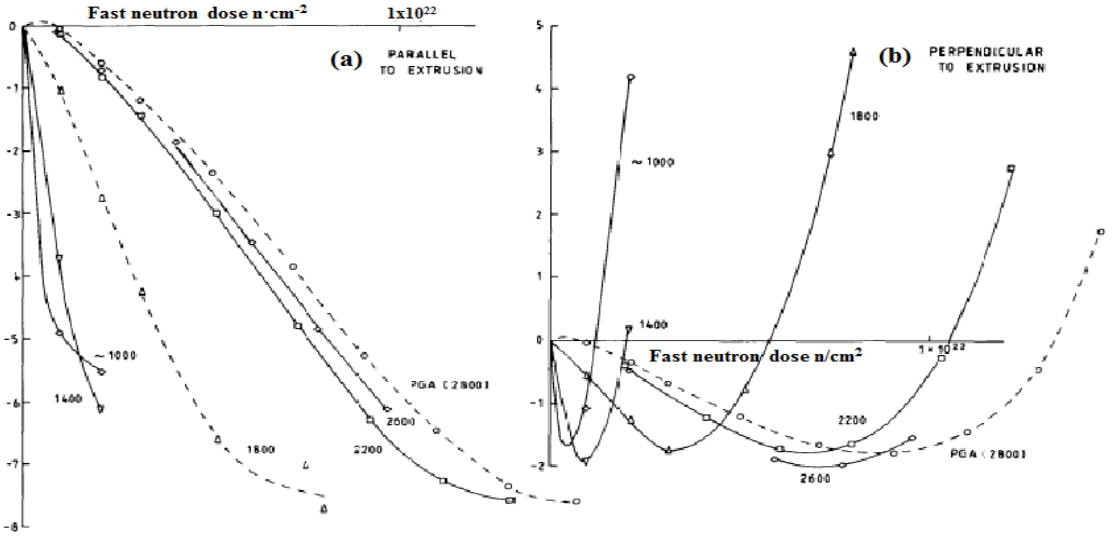

Figure 2.22 Dimensional changes induced in PGA by neutron irradiation at 600°C and heat treated up to 2800°C (a) parallel to extrusion – a-axis; (b) perpendicular to extrusion – c-axis [53]

At high dose rates, the final expansion may be influenced by the alteration of other properties due to irradiation [7]. Ultimately, the key observed changes in nuclear grade graphite are micro-crack closure from expansion in the **c**-direction and dimensional change from irradiation induced creep [7,62].

The observation of the size change motivated further investigation into the cause of these changes. Thrower made an extensive investigation of the defect nucleation and migration inside graphite, and their link with dimensional changes or other physical properties (e.g. elastic modulus) [26,46,48,49,63,64]. As mention in the previous section by conducting TEM investigations, he correlated defect nucleation and the formation of clusters of vacancy loops with the dimensional changes [48].

The experiments revealed that with the same experimental parameters (dose and temperature), the defects created were slightly different, with the appearance of some bigger loops for single crystals as compared with pyrolytic graphite, but with a lower density (Figure 2.23).

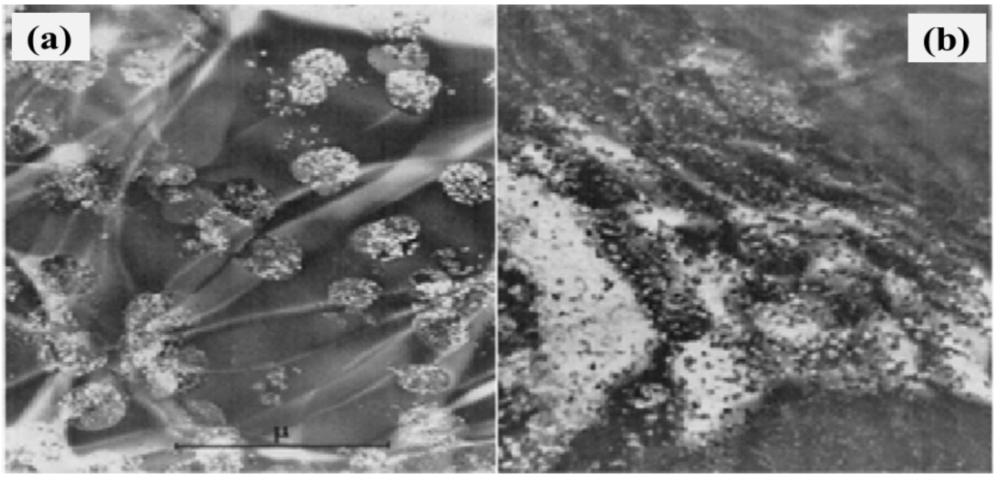

Figure 2.23 Defects produced by irradiation at 1350°C to 11.7 x 10^{20} n/cm^2 on single crystal (a) and (b) pyrolytic graphite graphitized at 2900°C [48].

B. Lattice strain

As it was shown in this chapter, due to annealing, the created vacancies and interstitials tend to group in clusters. This event may induce crystal strain inside graphite, which is correlated with the deterioration of graphite properties, and it is considered to be the major factor in nuclear graphite degradation and failure.

In 1977 Kelly *et al.* [41] made a theoretical estimation of the strain evolution (Figure 2.24) as function of irradiation temperatures, based on the true values of crystal dimension change from: irradiated pyrolitic single crystal or reactor grade graphite (b). His calculations were proven to be very similar to the accumulation of interstitial in defect loops, observed in the PGA irradiated at different temperatures and doses, behaviour presented in Figure 2.24 (a).

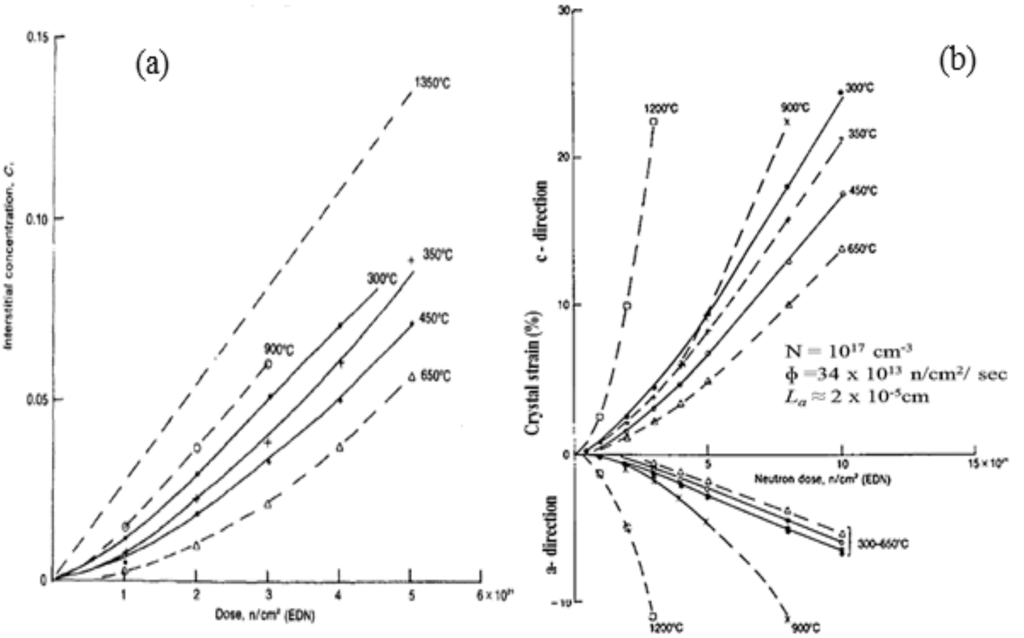

Figure 2.24 (a) interstitial concentration in PGA versus neutron dose; (b) Crystal strains at different temperatures as a function of dose [41];N - density of nuclei; ϕ - irradiation flux, L_a - crystallite size.

C. Coefficient of thermal expansion (CTE)

Related to the dimension changes, the coefficient of thermal expansion (CTE) has also been calculated. This is the degree of expansion divided by the change in temperature. It was concluded that CTE fluctuations with temperature are due to the variations in the thermal expansion of crystallites, and not to the other changes in structural parameters. This explains why in bulk graphite, changes in volume are lower compared to the volume of crystallites expansion, considering that the nuclear graphite is a porous structure that gives space to accommodate expansion of crystallites.

It was concluded that bellow 300°C, the CTE is dependent upon dose and temperature in both **c** (⊥ to extrusion) and **a** (‖ to extrusion) directions. Unfortunately the lack of data explaining what exactly is happening above 300°C, gives rise to suspicions that the already calculated data below 300°C is influenced by the crystal strain due to the cooling of the material [57]. However it was observed that the CTE in the both **c** and **a** has the tendency first to increase and saturate at a specific dose and temperature, and then decreases, (Figure 2.25) [8,28,65].

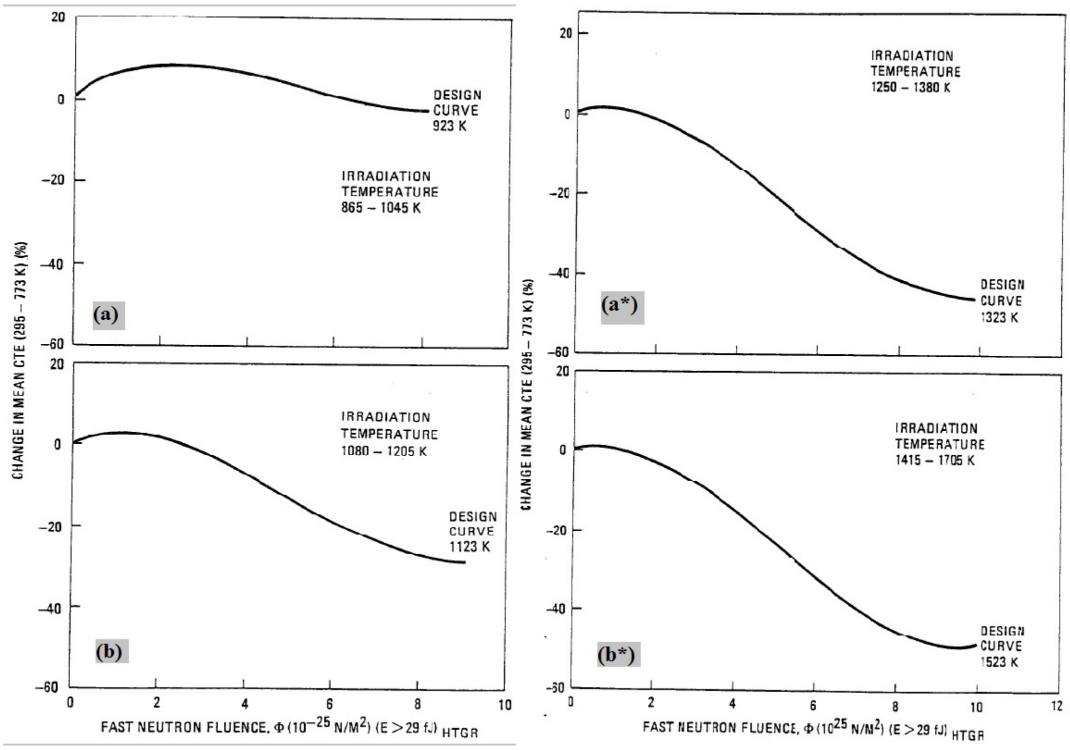

Figure 2.25 Varian of the mean coefficient of thermal expansion with irradiation for both high (denoted by *) and low temperatures [28]; a, a* denoted for the axial measurement; b,b* -radial measurement-

D. Thermal conductivity

Another important property of graphite, which has been studied, is *thermal conductivity* of graphite (although it still remains an incomplete set of data). The thermal conductivity is dependent on the temperature as well as the dose, and when measuring the thermal conductivity one has to consider the value of thermal conductivity of the material before and after irradiation [8]. In graphite thermal conductivity is due to the vibrations in the lattice, vibration that rise as a result of point defects and grain boundaries presented in the basal plane.

Kelly made a theoretical estimation (Figure 2.26) of thermal conductivity change for pile grade A graphite (PGA) as a function of dose and temperature. His calculations were based on accumulation of basal point defects in the lattice due to irradiation. His results were compared to empirical measurements on reactor graphite and were in good agreement with Rappeneau *et al.* [66].

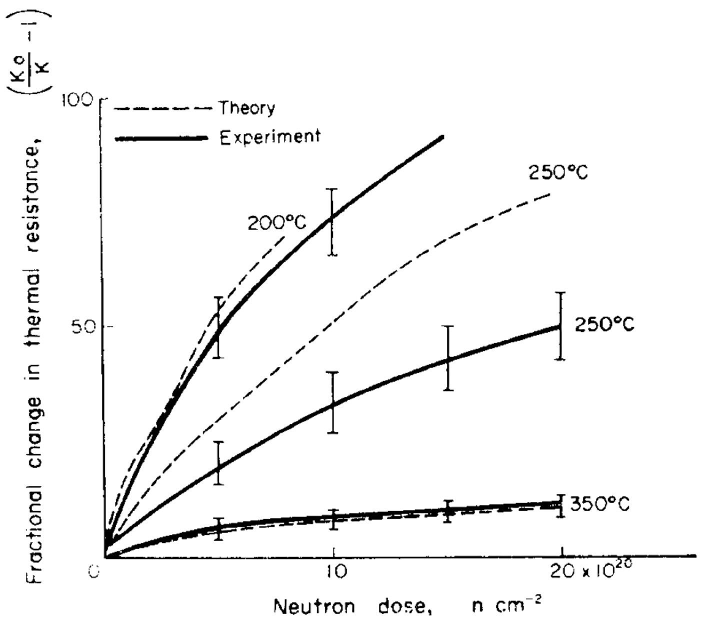

Figure 2.26 Comparison between theoretical and empirical values of the thermal resistance as a function of neutron dose [172]; where K^0 and K are the thermal conductivity values, before and after irradiation, respectively

E. Young's modulus

Previous work suggested that the dimensional change correlates with change in other properties. In 1994, based on previous work stating that for polycrystalline graphite the elastic moduli is dependent on the structure factor, which itself depends on the X_T, the evolution of crystallite dimension factor previously introduced (Figure 2.27).

X_T makes a good connection between the dimensional changes, and how this is related to other properties. Correlations were made by Oak Ridge National Laboratory for HOPG, irradiated at 600 °C, and another synthetic near –isotropic and fined-grained graphite, irradiated at 875 °C (Figure 2.27) [46]. Physical properties change as a function of X_T, were also correlated for PGA irradiated at temperatures in the range of 430 - 600 °C [46].

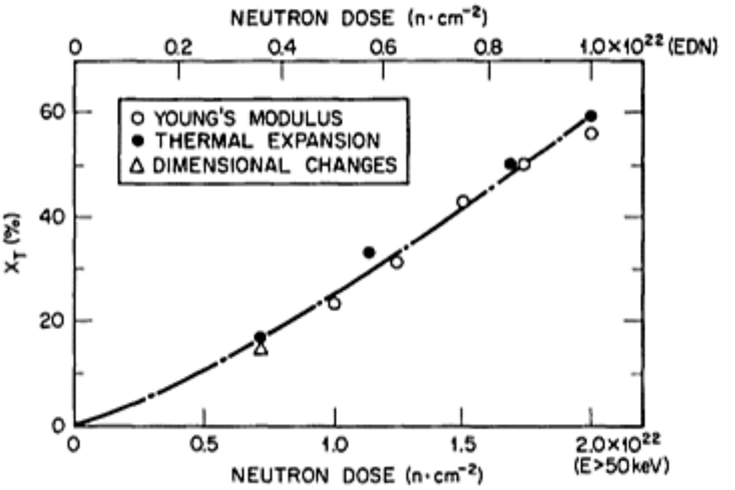

Figure 2.27 Comparison of X_T with dose obtained from Young Modulus, thermal expansion coefficient changes at 875°C on near-isotropic synthetic graphite [59].

2.3.2. Electron Irradiation

The lack of understanding and viewing in real time of the dynamics of structural changes produced by neutron irradiation required the help of more convenient experiments. Ions and electron seemed a good substitute of neutron irradiation, with both inducing damage together with a more easy control of experimental parameters. Electrons were preferred against ions, as the latter produce a damage cascade that was not easy to control, whilst electron irradiation could be done *in situ* in a TEM.

Over the years, several experiments were done and observations were made based on the different parameters that are influencing the irradiation damage: dose, temperature, and duration of experiments.

It was established that the calculated dose in dpa (displacement per atom) for electron irradiation and neutron irradiation should not be directly compared because of the difference in dose rates ($1x10^{-4}$ - $1x10^{-3}$ dpa/s for electrons against $1x10^{-7}$ dpa/s for neutrons) [67]. It was observed that the electron irradiation causes point defect damage, whereas the higher mass and lower dose rate of neutrons causes cascade damage.

Accounting for the relatively wide spacing of graphite's lattice planes results in low density collision cascades, and the low neutron dose rates (10^{-7} dpa s^{-1}) and high temperatures (~450 °C) in the nuclear reactor allow this cascade damage to partially anneal between cascade events [8]. The net effect is point defect damage, making high temperature neutron irradiation damage arguably comparable to higher dose (10^{-4} - 10^{-3} dpa s^{-1}) electron beam induced damage [62,68].

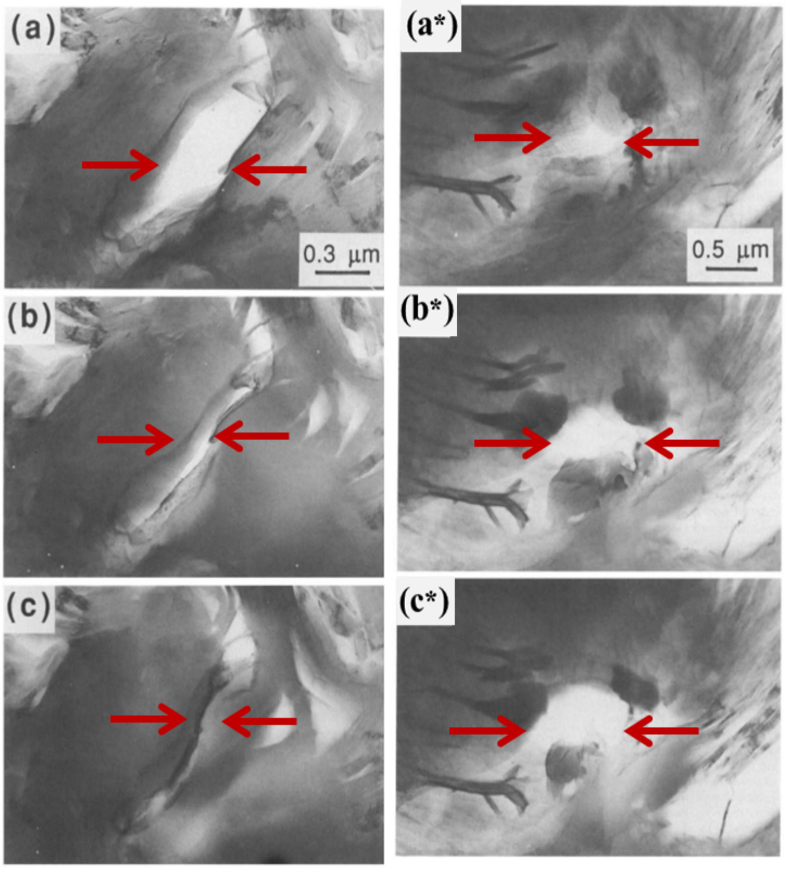

Figure 2.28 Elongated pores closing due to irradiation : (a) 0dpa; (b) 0.02dpa; (c) 0.24dpa; and round pores opening up due to irradiation : (a*) 0; (b*) 0.4dpa; (c*) 0.6dpa; [67].

In 1994 Pedraza *et al.* [67] reported evidence supporting the theoretical supposition of the dimensional changes in nuclear graphite due to irradiation. The experiment was made in a TEM, and the samples were *in situ* irradiated with the electron beam receiving a dose of up to 1.1 dpa/s. The observation highlighted the fact that the existence of micro-pores were accommodating the dimensional change by allowing the elongated pores inside the crystal to close at higher irradiation doses, suggesting an expansion in the c-axis, while round pores (which were surrounded by crystallites) exhibited opening due to low irradiation evidence of **a**-axis shrinkage (Figure 2.28).

Following the same irradiation procedure and experimental parameters, the same authors investigated the structure of irradiate graphite by analysing the carbon K-edge EEL spectra. They concluded that the structure of graphite after electron irradiation was resembled amorphous graphite which has predominantly sp^2 bonding and in which irradiation induced interstitials were located in non-six member ring's [69] (suggesting migration of atoms and formation of interstitials in loops). This change in bonding was confirmed by others [70].

Tanabe intensely investigated neutron [51,71], ion and electron beam irradiation damage in graphite [72–74]. He claimed that the mechanism of dimensional change proposed before was unsustainable. Based on the lack of evidence supporting the assumption made in the past, according to which dimensional change is due to be formation of new extra basal planes caused by interstitial that were migrating and were forming interstitials loops. Moreover their theory was supported by TEM investigations highlighting plane buckling (Figure 2.29) and fragmentation of the crystallites, agreeing with previous ideas of the formation of amorphous graphite (or nanocrystalline graphite) [51,75–77].

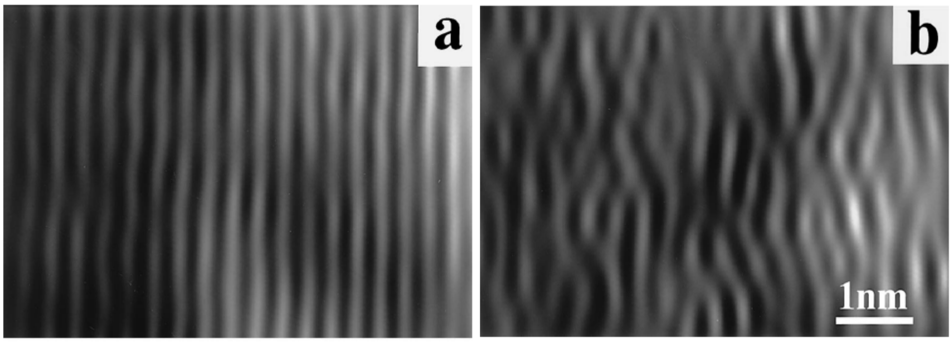

Figure 2.29 Processed images of graphite plane under no irradiation (a) and with buckling planes under electron irradiation of 1.2 dpa at 94K (b), similar behaviour of graphite under electron irradiation at room temperature [77].

Tanabe & Muto assessed also the change in damage rate and behaviour of graphite due to irradiation temperature. At temperature of irradiation bellow 327 °C, the structure tries to heal itself by reordering the displaced atoms in the basal plane into non-hexagonal rings. Above 377 °C, the damage is on a higher scale, and it occurs by fragmentation of crystallites but keeping the hexagonal rings intact in the basal planes [78].

In 2011 Karthik *et al*. [62] managed to record the formation of dislocations in graphite when irradiated with electrons. Their experiment was undertaken *in situ* in a TEM, and provided an irradiation dose of ~0.25 - 1dpa. The examined graphite presented a well-known behaviour when irradiated with electrons (e.g. lattice swelling, crack-closing). According to the authors, the experiment provided empirical evidence for the existence of interstitial loops. However, the results were obtained by Fourier filter, which could have been given rise to artefacts.

Chapter 3 Methods and methodology

Structural characterisation can link properties at the macroscopic scale to the microscopic atomic construction of a desired material. The next sections of this chapter present three of the most common and powerful structural analysis techniques: X-Ray Diffraction (XRD), discussed in section 3.2; Raman Spectroscopy (RS) presented in section 3.3; and Electron Microscopy – Transmission Electron Microscopy (TEM), Electron Energy Loss Spectroscopy (EELS) and Scanning Electron Microscopy (SEM), discussed in section 3.4

3.1. Materials used

Different types of nuclear graphite were analysed by XRD, Raman Spectroscopy, TEM-EELS and SEM. They had different grain sizes, and some were pre-neutron irradiated at different temperatures and doses. Because the irradiated nuclear graphite was not available from the beginning of the study, several virgin nuclear graphites were used instead: two PGA graphites from Wylfa and Oldbury from the decommissioned reactors of the same name, Gilsocarbon, IG-110, NBG-18, PCEA and PCIB (background information about those samples can be found in section 2.2.2).

The five irradiated samples used, PCIB and PCEA type, are shown in (Figure 3.1) and listed together with their properties in **Table 3.1.** The sample were provided by Idaho National Laboratory (INL) US, and for more information regarding the irradiation procedure of the samples the reader is advised to read Appendix B, or the associated INL report where the samples are referred as "Piggy-Back" specimens [2,79].

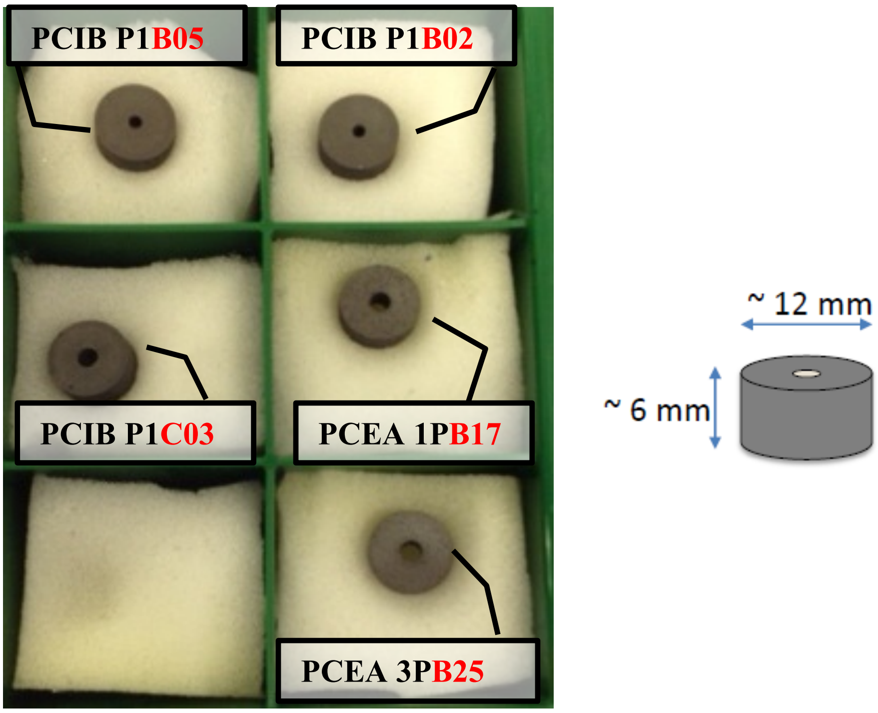

Figure 3.1 Irradiated samples available (left) and their dimension (right)

For an easy identification, the samples are referred by the "NAME" referenced in **Table 3.1.**

Table 3.1 Information on the irradiated samples used ·

ID	NAME	Est. dose (dpa)	Activity (kBq)	Est. Temperature (°C)
PCIB P2C03	**PCIB C03**	**1.5**	**30**	**350.9**
PCIB P1B02	**PCIB B02**	**4.1**	**330**	**534.5**
PCIB P3B05	**PCIB B05**	**6.8**	**175**	**656.9**
PCEA DW15C01	**PCEA B25**	**1.5**	**15**	**350.9**
PCEA DW14C01	**PCEA B17**	**6.8**	**30**	**670.9**

The samples were prepared differently, in accordance with each technique. For XRD and Raman spectroscopy some samples were cut with a Strauers Accutome-2

· Irradiation data provided by INL

cutting machine at a speed of 1200rpm/sec into samples of dimensions approximately 15mm (length) x15mm (width) x 1mm (height) (PCIB, PCEA and GILSO). The other samples were used as received – each of them having the geometry of ~ 6mm (height) x 12mm (diameter) cylinders: virgin Wylfa, Oldbury, IG-110, NBG-18, and irradiated PCIB –C03, B02, B05, PCEA- B25, and B17.

For TEM/EELS all samples were prepared abrading each sample with a piece of Aluminium Oxide P1200, grinding paper, in a liquid environment - isopropanol in this case. A drop of isopropanol mixed with the exfoliated graphite was drop cast on to holey carbon film supported on a copper TEM grid.

3.2. X-Ray Diffraction (XRD)

3.2.1. XRD methodology

X-ray diffraction consists of elastic scattering of X-rays by parallel planes of atoms which share the same Miller indices [80,81] as depicted in Figure 3.2, equivalent to reflection (with no change in phase) at a specific angle creating intense peaks by constructive interference which correlates with the inter-planar distances (d_{hkl}), explained by Bragg's law:

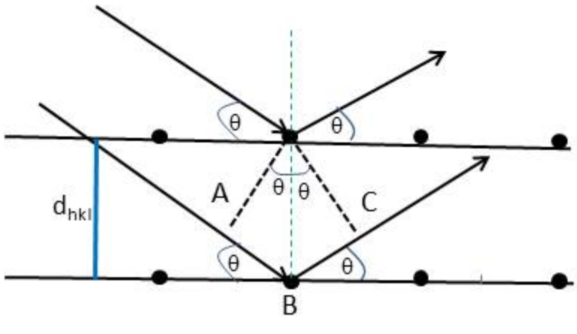

Figure 3.2 Diffraction on parallel atomic satisfying Bragg's law.

$$n\lambda = d_{hkl}\sin\theta \qquad \text{Eq. 3.1}$$

where: n - is the diffraction index; λ – is the wavelength of the X-Ray used (Å); d_{hkl} – is the inter-planar distance corresponding to the hkl Miller indices; θ – is the scattering angle.

XRD can provide information about the coherence lengths of crystallites via Scherrer's (Eq. 3.2):

$$L = \frac{\kappa\lambda}{\beta\cos\theta} \qquad \text{Eq. 3.2}$$

where: k – is the shape factor; λ – is the wavelength of X-rays used (Å); β – is the full width of Bragg XRD peak at half-maximum height; θ – is the scattering peak in radians corresponding to Bragg XRD peak.

Most commercial XRD equipment used today are semi-circular diffractometers, in which the X-ray tube and the detector move at the same time (Figure 3.3), and the DP is given in 2θ.

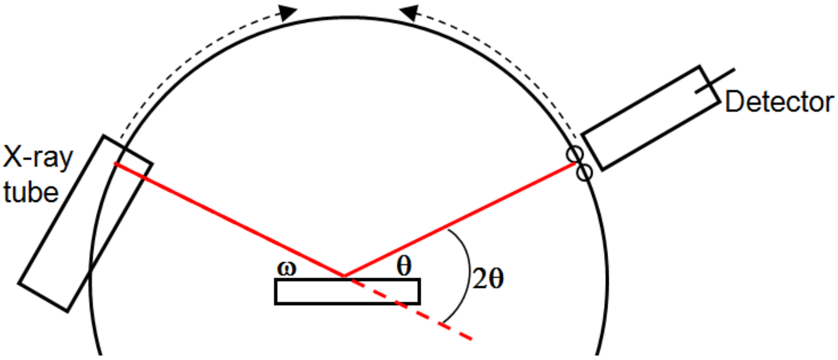

Figure 3.3 Diffractometer geometry.

XRD does not only give the d-spacing and the coherence lengths of crystallites, it can also offer information about the unit cell and symmetry of a material.

For the case of graphite, which has an hexagonal unit cell, the lattice parameters **a** and **c**, can be found from the following equation:

$$\frac{1}{d_{hkl}^2} = \frac{4}{3}\left(\frac{h^2 + hk + k^2}{a^2}\right) + \frac{l^2}{c^2} \qquad \text{Eq. 3.3}$$

where: d_{hkl} – is the interplanar distance; **a, c** – are the lattice parameters ; h, k, l – are the Miller indices corresponding to Bragg XRD peak.

In 1942 B. E. Warren proposed [82] that for the heat treated black carbon materials which exhibits needle-shaped crystals, the **k** value used for calculating L_a and L_c from Scherrer's equation (Eq. 3.2) is different for each of the two cases. This arises from rotations and translations in the layers, which give, rise to lattice misorientations, which can result in (hk) reflections.

3.2.2. XRD experimental details

Low angle scattering of X-rays can provide information about the defects produced by irradiation, and the presence of inter-crystalline pores in unirradiated graphite [8].

In the case of graphite there are established specific reflections for calculating the unit cell parameters: for the **a**-spacing the (100), (110) and (112) reflections are used; for the **c**-direction, the d-spacing (the distance between consecutive basal layers) is calculated from the (002), (004) and (006) reflections [3].

In the begging of the nuclear graphite "era", researchers (e.g. Nightingale, Goggin, Reynold, Simmons [3,60,61,83]) were giving as indicative the (002) and (110) rings (or peaks for XRD) for subtracting the **c-** and **a**-constant for nuclear graphite. If for (002) peak the situation remained clear over the years the situation, for (110) the situation changed and it became more costumed to consider (100) peak as more appropriate to be used in calculating the value of the **a**-constant in carbonaceous materials [84–86].

For both direction (100) and (110), a factor of correction is needs in order to obtain the **a** constant of the lattice, 4/3 for (100) and 2 for (110) (Figure 3.4), which means that neither of them is providing the direct **a** value, nor it represents the real peak for subtracting the **a** constant. Furthermore in the diffraction patters of graphite, the (100) peak is at lower 2θ (~42 2θ), while (110) peak is at higher 2θ (~78 2θ), the letter being more susceptible for broadening errors due to the angular position (e.g. strain).

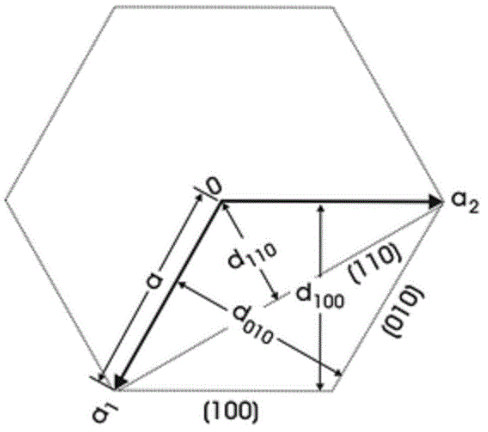

Figure 3.4 2D hexagonal crystal structur

Considering both situations for the **a** constant (old and recent) it was decided that (100) peak was the best option to be used in obtaining **a** an calculating L_a.

By using the Scherrer equation (Eq. 3.2), an average of the out-of-plane crystallite size (coherence length in the **c**-direction) - L_c, can be estimated from the broadening of (002) peak, while the in-place crystallite size (coherent length in the **a**-direction) – L_a from the broadening of (100).

XRD data analysis

The majority of the XRD measurements in this thesis were obtained from solid samples (bulk as received) with a Panalytical X'pert Pro diffractometer working in 2θ Bragg geometry. The machine uses X-ray radiation from a Cu anode (40 keV, 40 mA, λ= 1.545 Å). The XRD pattern for 2θ was collected from 20° to 90° in continuous scanning mode with interval of 0.066° at a speed of 300 s (time/step).

The diffractogram analysis was done using X´pert High Score Plus software where background determination and peak positions were considered in addition to instrumental broadening. The d-spacing was automatically provided by the software, while the lattice parameters **a** and **c** were calculated with Eq. 3.3. As reference, the file number 00-056-0159 was used, from the International Centre for Diffraction Data (ICDD) library , which was accessed through the X´pert High Score Plus software [87].

The instrumental broadening was measured from the line profile of a standard silicon specimen, using the same experimental set-up as for the other samples. It was subtracted in quadrature manually from each peak position that was of interest as the instrumental broadening increases with the 2θ [88].

The strain broadening was subtracted (where possible) using a Williams and Hall plot [88] (Figure 3.5).

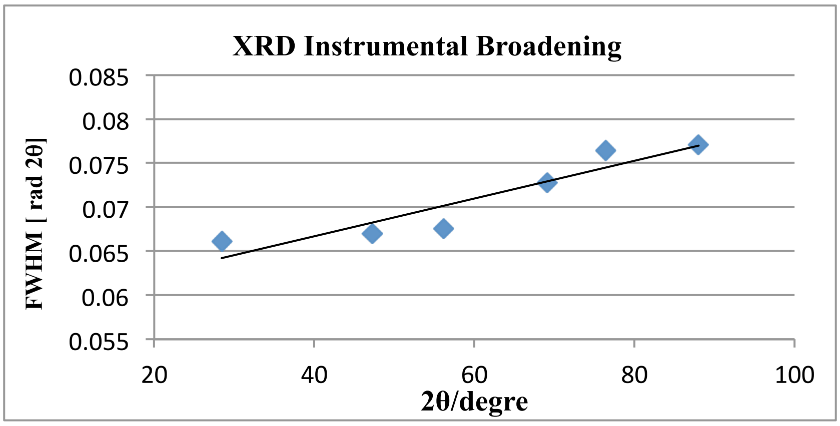

Figure 3.5 FWHM in radians versus 2θ in degrees, of the Si peaks from XRD pattern

Finally, the coherence lengths were determined from the remaining broadening by means of Scherrer's equation (Eq. 3.2), with the following shape factors: for L_a - k=1.84, and for L_c - the usual value was used k = 0.9.

3.3. Raman spectroscopy

Raman spectroscopy is one of the most classical, non-destructive spectroscopy techniques known. It was improved by the discovery and use of lasers as source of monochromatic light, and it is based on the principle of scattering and absorption of photons as a result of interaction with matter. The scattered photons can have different forms: 1. Rayleigh scattering - or the elastically scattered photons (having the same energy as the incident photons); 2. Stokes and anti-Stokes scattering, with inelastically scattered photons of a lower or higher energy than the incident photons, conditioned by the transfer of vibrational energy between the incident photon and the illuminated system, which can be initially either in ground or excited state (Figure 3.6).

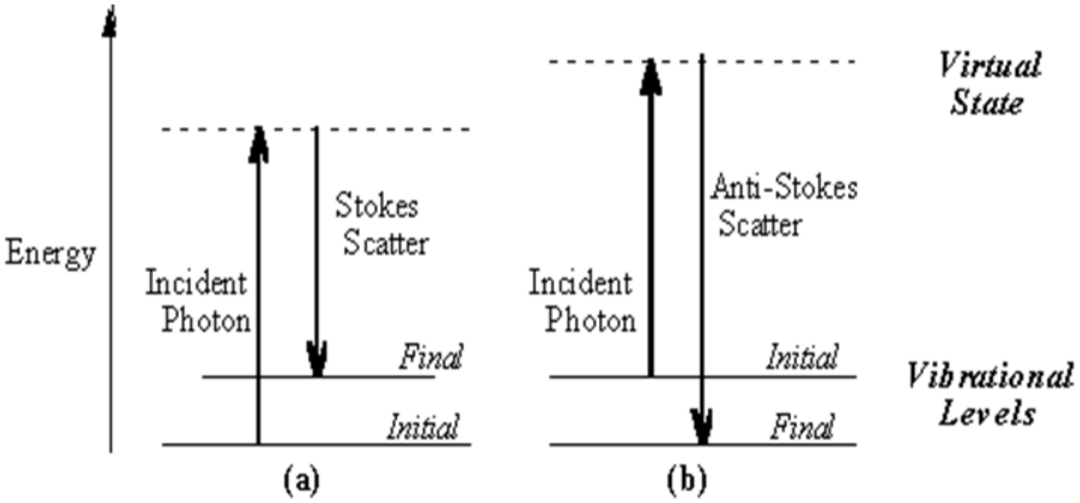

Figure 3.6 Raman scattering energy level diagram; (a) Stokes Raman scattering; (b) anti-Stokes Raman Scattering.

3.3.1. Raman spectroscopy methodology

When carrying out Raman spectroscopy, the sample is illuminated by a laser beam, which can emit light either in UV, visible or near IR range. The beam reaches the sample through the lens system of an optical microscope, the scattered beam is returned back through the same system, where finally the Raman spectrum is measured with a high-sensitivity, multichannel energy detector. The predominant signal comes from Rayleigh scattering, and the detector needs the signal to be filtered, in order not to saturate the detector, as the Rayleigh energy is much higher intensity than the Raman scattering. Therefore, the Raman systems have Notch filters that stop or attenuate the unwanted signal (e.g. fluorescence or reflectance signal from the sample). Shown in Figure 3.7 is the optics behind the acquisition of spectra.

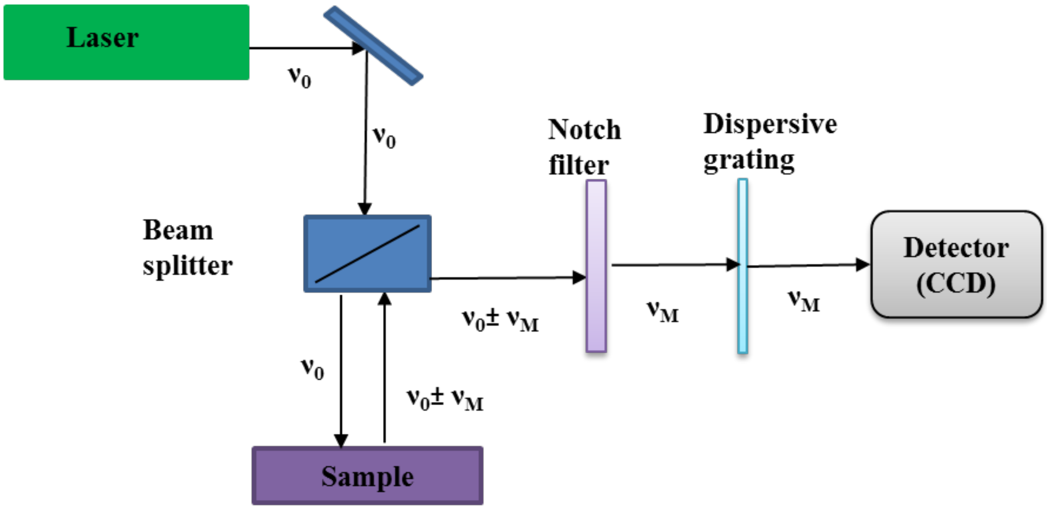

Figure 3.7 Schematic of the Raman spectroscope equipment; where ν_0 is the Rayleigh scattering and ν_M is the Raman Stokes or anti Stokes scattering

The remaining signal is filtered by a dispersion array which separates the signal into different wavelengths before being counted by a detector, which records the intensity of inelastically scattered light as a function of frequency (wavenumber). From this vibrational (phonon) energies can be inferred.

3.3.2. Raman spectroscopy of Carbon

Over the years Raman spectroscopy has become an important tool for characterizing such as amorphous carbon, black carbons and commercial graphite (from which nuclear graphite was derived).

For diamond, only one peak can be seen in the first order of Raman spectra, which appears at ~1332 cm^{-1} (Figure 3.8), with an overtone at ~ 2667 cm^{-1}. The Raman spectra of diamond is due to the longitudinal vibration mode F_{2g} and represents the only Raman active vibration for cubic diamond, as suggested by Solin in 1970 [89], and agreed further on by other researchers like Ramdas in 2000 [90] or Nemanich in 2004 [91]

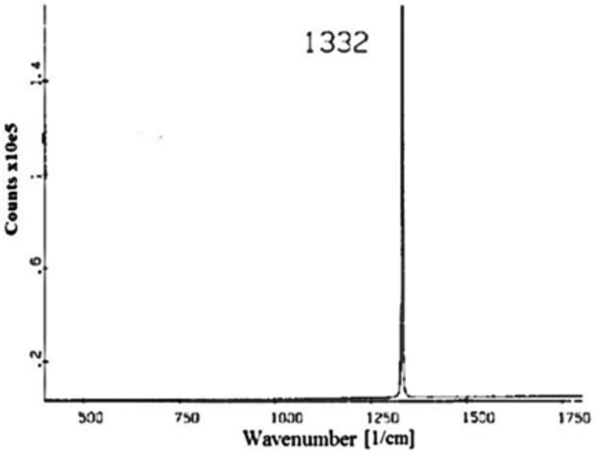

Figure 3.8 Raman spectra of diamond [114]

In 1979, the normal vibrational modes of graphite where defined by Nemanich & Solin, using Eq. 3.4 [92], corresponding to Figure 3.9:

$$\Gamma_{vib}=2A_{2u} \oplus 2B_{2g} \oplus 2E_{1u} \oplus 2E_{2g} \qquad \text{Eq. 3.4}$$

where A_{2u} and E_{1u} represent the translations of the plane; B_{1g} is the optical vibration mode where the carbon atoms move normal to the graphene plane; and E_{2g} which is an optical vibration that describes the in-plane movement of the atoms.

In Raman, the only active vibrational mode is the E_{2g}, which can be seen at ~42 cm^{-1} and 1582 cm^{-1}. Even though the graphite basal planes are bonded by weak Van der Waals forces, their energy is big enough to change the symmetry in the way that the ~42 cm^{-1} peak is seen in graphite but not in graphene, as it is an in-plane vibration mode active due the graphene layers gliding over each other [93].

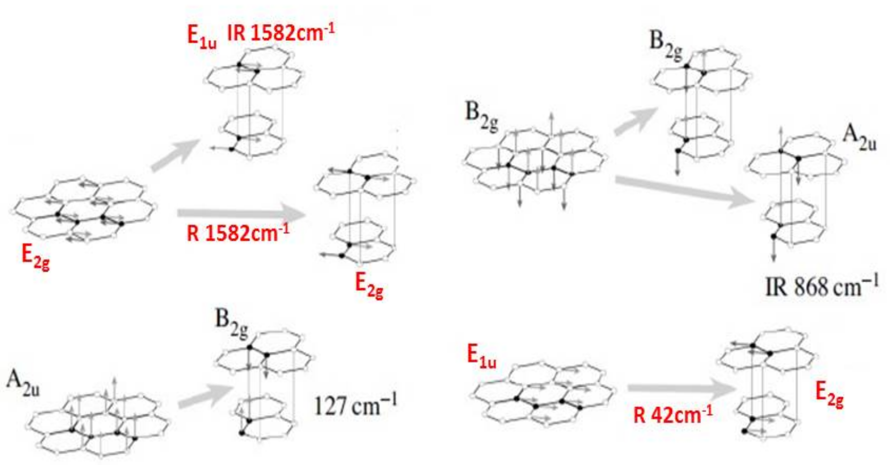

Figure 3.9 Graphite vibrational modes, highlighted in red the E_{2g} vibration mode with the two specific vibrations E_{1u}, infrared (IR) visible, and E_{2g} which is Raman visible [93].

Raman spectra of graphite and amorphous carbons

In graphite, the most prominent feature, considered its finger print peak [92,94,95], can be seen at ~1580 cm^{-1} (Figure 3.10), the G peak. According to Dresselhaus *et al.*, and supported by other authors, this peak is attributed to the first-order Raman scattering, and it is due to double degenerate phonon mode of in-plane (basal plane) vibrations - the E_{2g} mode [96–100]. The name "first order" comes from the number of scattering events, which involve only one phonon emission.

The G peak can be seen in all the poly-aromatic hydrocarbons materials and is due to the stretching of all pairs of sp^2 atoms in both chain or rings [101].

The second most important peak is the D peak, at ~1357cm^{-1} (Figure 3.10). It appears sometimes only in the small particles (~2-5nm) of crystallised graphites or disordered graphites, and disappears in perfect crystals [102–104]. The D peak is a feature due to the double-resonance Raman scattering, and compared to the G peak, it has a dispersive nature (its position can move with the change of excitation energy) [103].

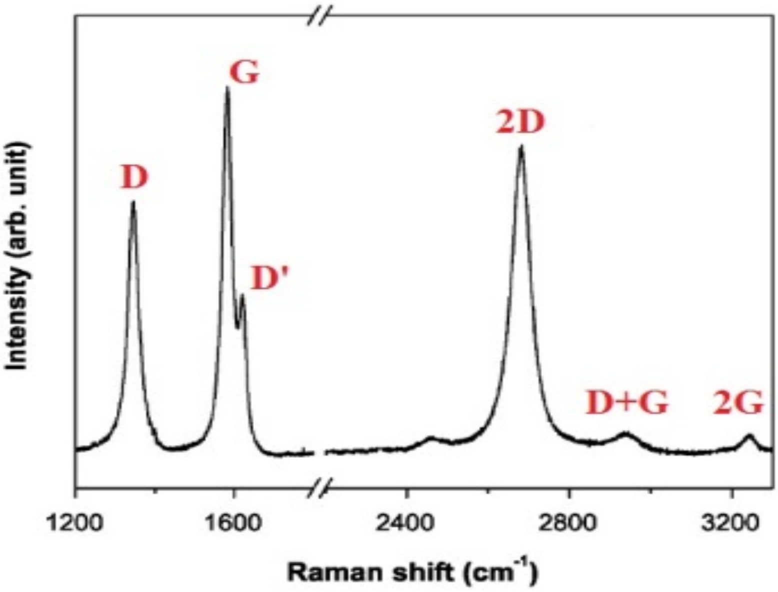

Figure 3.10 Raman spectra found in graphitic materials.

During the years, people attributed the presence of this D band to the existence of defects in the lattice, and as a result of the breathing mode of the phonon [98,105]. The optical mode believed to be responsible for the breathing mode of phonons is A_{1g}, a mode which is Raman active but not for graphite which has the $D6_h$ symmetry [106–108]. The latter groups acknowledge the D band as arising a result of some intercalations or disorder in the lattice (e.g. vacancies and interstitials), and according to [93] the D band appears regardless of the type of defect that is distorting the lattice/ symmetry.

In some cases another peak is present in the Raman spectra of carbons, namely D', at ~1620 cm^{-1}. The D' peak is an overtone of the D peak, and some state that its appearance is due to the electron being backscattered by a second phonon and not by a defect (as a result of double resonance of the D peak [93]). However, during the years, other explanations for the D' peak were considered: it appears only in the imperfect graphites and disordered carbons [92], such as intercalated graphite compounds or oxidized carbons [109]; or its appearance is connected to the loss of basal plane translational symmetry [110] that might be found at the edges of crystallites [111].

At the end of the carbon Raman spectra of carbon (Figure 3.10), second order phonon scattering, the 2D peak at ~2710cm^{-1} - this is the overtone of the D peak; and the 2G peak at ~3300cm^{-1} - the overtone of the G peak. During the years, researchers focused on the 2D peak, since it can provide evidence of micro-crystallinity [112]. Another peak can be seen at ~2950 cm^{-1}, namely the D+G peak, which according to Wang *et al*. [109] can be attributed to the influence of both E_{2g} and D modes.

Compared to graphitic carbons, which have an ordered structure (Figure 3.11 (a)), amorphous carbon does not have a crystallographic order. In amorphous carbon the structure has only short range order [113]. The differences between the Raman spectra of amorphous carbons are not large, as can be seen in Figure 3.11 (b). However, the G and the D peak can still be seen, but the broadening of the peaks is bigger and in some cases they even overlap, and in other cases the intensity of the D peak is larger than the G peak, opposite to the case of graphite spectra.

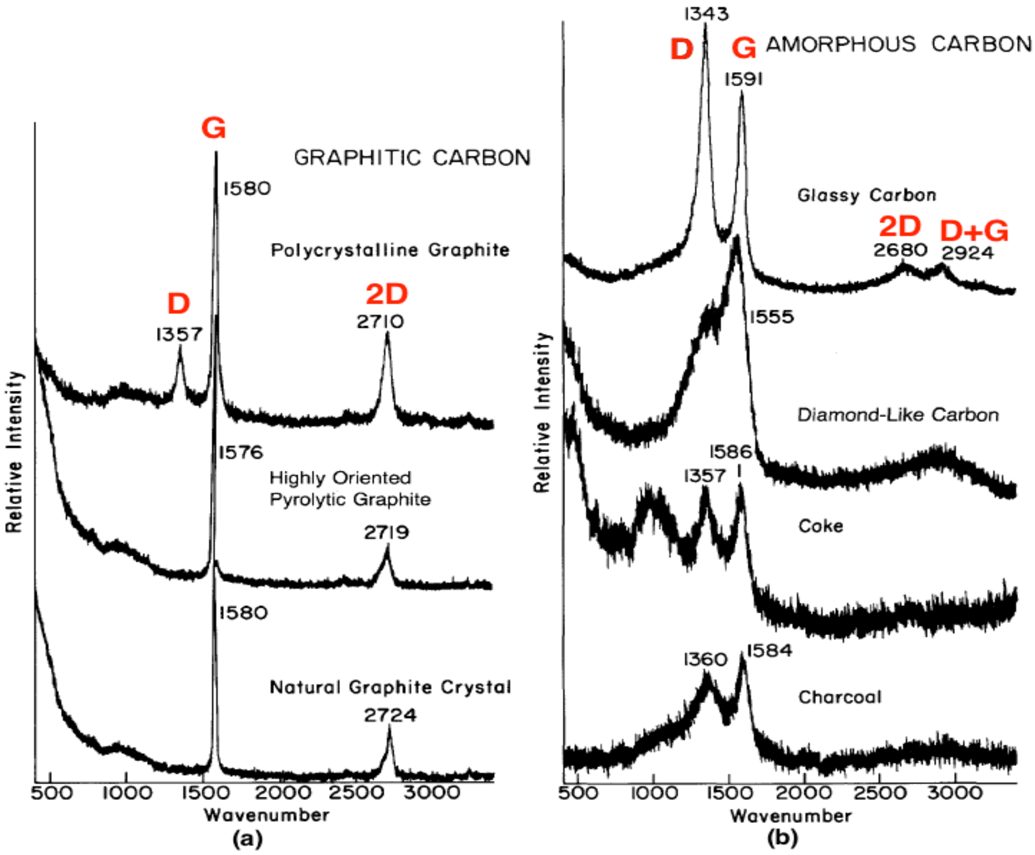

Figure 3.11 Raman spectra of different carbonaceous materials [114].

From using known information on the atomic and electronic structure of disordered carbons Ferrari proposed a theoretical model for the course of amorphization of carbon (Figure 3.12) in terms of the corresponding changes in spectra [101]: a) graphite change to nano-crystalline graphite; b) nano-crystalline graphite transforms to low sp^3 content amorphous carbon; c) low sp^3 content amorphous carbon transforms to high sp^3 content amorphous carbon. According to him the easiest way to keep track of change in the course of amorphisation is by following the evolution of the position of the G peak or the I_D/I_G ratio.

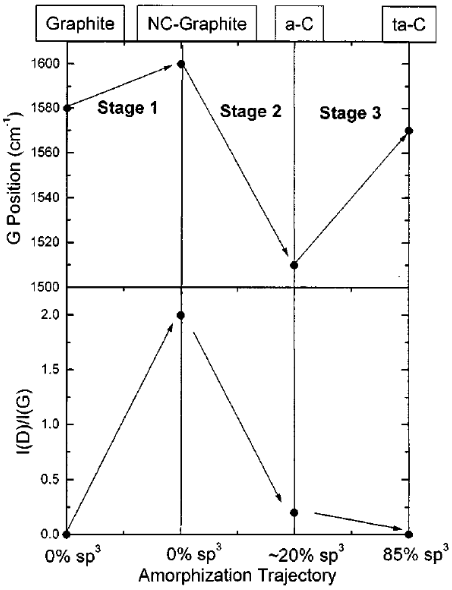

Figure 3.12 Schematic variation of G peak and I_D/I_G, corresponding to different stages of disorder [113].

Since 1970, when Tuinstra & Koening's (TK) first introduced an empirical relationship [95] correlating the value of coherence length in the **a**-direction L_a, found by XRD, with the intensity ratios of the Raman D and G peaks, it was widely used to define microcrystalline domains in graphitic carbons. Over the years, there has been no general agreement concerning this correlation: similar results from XRD for L_a [112,114–116] were reported, and some results one order of magnitude higher than the ones reported by TK [117] were found.

Those proposing the validity of the TK correlation $I_D/I_G \sim L_a$ admit that special care has to be taken in finding the L_a value, and suggest, for better accuracy, that XRD should be the first technique considered instead of Raman [116]. Others [98,114] have applied a correction factor to the TK relationship based on the energy of the Raman laser, to the TK formula:

$$L_a(\mathrm{nm}) = \frac{560}{E_{\mathrm{photon}}^4}\left(\frac{I_D}{I_G}\right)^{-1} \qquad \text{Eq. 3.5}$$

where: L_a – is the coherence length in the **a** direction; E_{photon}- is the energy of the laser photon; $\lambda_{\mathrm{photon}}$ – is the wavelength of photon; I_D, I_G – are the intensities of disorder and order Raman peaks, respectively.

Because the TK formula has a limited application for the domain size of crystallites [117], and also its applicability is debatable for all the nuclear graphites, in this thesis the ratio I_D/I_G will be used only to compare the graphitization degree/disorder between samples alongside several other parameters.

During the years, different attempts were made to make a classification system for measuring the degree of graphitization/disorder in carbonaceous materials with the help of Raman Spectroscopy [109,114,118,119]. In the following analysis section of this thesis, only the parameters extracted from the first part of the Raman graphite spectra will be used to establish the perfection or lack thereof: (a) The position of the G peak; (b) The D/G intensity ratio; (c) The FWHM of the G peak.

3.3.3. Raman spectroscopy experimental details

Raman investigation was carried out at room temperature, using a commercial Renishaw Spectrometer. The equipment is composed of a Raman Spectrometer equipped with a CCD detector, and a modified optical microscope, having a resolution of the beam of ~1μm.

The spectra were recorded using an Ar/Kr ion laser of λ=514.5nm and a 50X objective was used to focus the laser light onto the samples. The laser power was adjusted to 24mW, and the spectral integration time was 30s with two spectra per accumulation. The Raman Shift spectral range 1000 - 3200 cm^{-1} was recorded, although the machine has the capability to work between 200 - 3200cm^{-1} or even lower, down to 20 cm^{-1}, if a filter is changed.

The specimens used were analysed as received, or prepared in a similar fashion to the specimens for the XRD investigation, by using a Struers Accutome-2 cutting machine at a speed of 1200rpm/sec.

Raman spectroscopy data analysis

In 1984 Dillon *et al.* [120] while investigating the disorder and crystallite formation in as-deposited and annealed carbon films, observed that the G peak exhibits an asymmetric shape under thermal treatment. While the peaks in the first order scattering of Raman spectra (D and G) could be described with two Gaussians, the asymmetric shape observed in the annealed carbons could not. The established procedure in this case is to use Breit-Wigner-Fano (BWF) function for the fitting of the G peak, and a Lorentzian fit for the D peak [113,120–122] .

The BWF can be described as in Eq. 3.6, where ω_0 is the G peak position with Γ being the FWHM of the same peak. 1/Q is the BWF coupling coefficient (coupling of the phonon-phonon modes), with the constraint that if 1/Q->0, the line shape transforms to a symmetrical Lorentzian.

$$I(\omega) = \frac{I_0\left[1 + \frac{2(\omega - \omega_0)}{Q\Gamma}\right]^2}{1 + \left[\frac{2(\omega - \omega_0)}{Q\Gamma}\right]^2} \qquad \text{Eq. 3.6}$$

The Raman data presented in this thesis was fitted using Origin lab 9.1, using the procedure described above, with the remark that a linear fitting was used for the background subtraction, and the initial ω_0 was introduced by the user to be the value usually found for nuclear graphite, $\omega_0 \sim 1583$ cm^{-1}. No other constraints were imposed, and the program was able to find the best fit determined by minimising the R^2 value.

3.4. Electron Microscopy

The interaction of high energy electrons with a sample is summarised below (Figure 3.13):

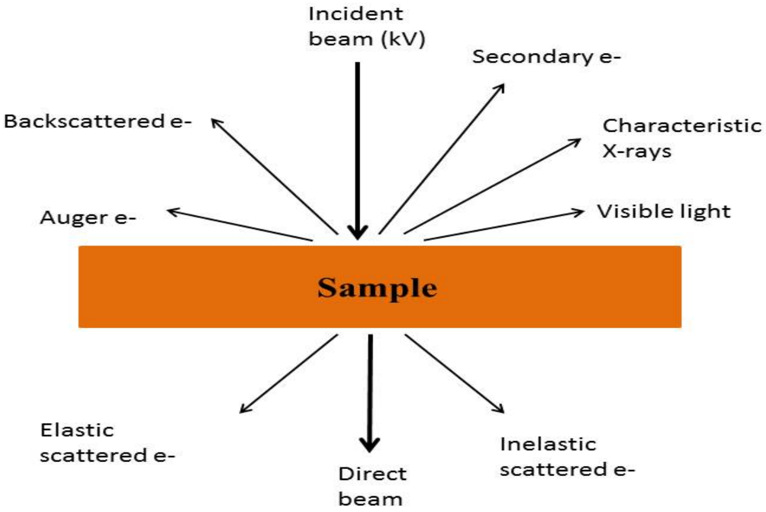

Figure 3.13 Different characteristic scattered signals generated when electrons interact with matter.

3.4.1. Scanning electron microscope (SEM)

SEM represents an important morphology study technique of a sample. In a SEM (Figure 3.14), accelerated electrons are focused into a small beam using a system of magnetic and electric fields, scanned across the sample surface. The incident electrons interact with the atoms from the sample, and scatter either inelastically or elastically, producing different types of signals for imaging (Figure 3.13).

Backscattered and secondary electrons are the main imaging signals in a SEM, the latter providing information on surface topology. During inelastic scattering, other events can take place, like the ionization of the atoms by generating characteristic X-rays which can provide information about the elemental composition of a sample.

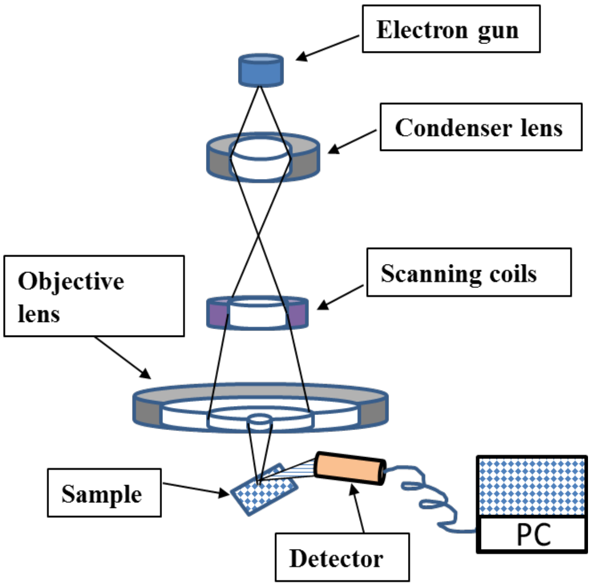

Figure 3.14 Schematic representation of a SEM device

In the present study, surfaces of the analyzed samples were examined using a LEO 1530 “Gemini” (Carl Zeiss, Cambridge) field emission gun scanning electron microscope (FEG-SEM) - for the virgin samples - or a FEI Nova 200 Nanolab dual-beam FEG-SEM/FIB (FEI Co.) –for the irradiated samples. For both SEMs, the secondary electron images were obtained using an in-lens detector at an operating voltage of 5keV. The samples were analyzed as received, and no coating was necessary as the samples were highly conductive.

3.4.2. Transmission electron microscope (TEM)

The electrons start to travel within the column with a uniform energy, given by the accelerating voltage. The accelerating voltage is in close relationship with the resolution of the microscope:

$$\boldsymbol{\lambda} = \frac{1.22}{\sqrt{E}} \qquad \text{Eq. 3.7}$$

where E (eV) is the energy of the electrons, and $\boldsymbol{\lambda}$ is their wavelength. For an accelerating voltage of E= 300 keV, the wavelength of the electrons can reach sub-angstrom dimension that are smaller to the diameter of an atom [123], while for 80 and

200 keV the wavelengths of the electrons are 4.17 x 10^{-3} nm and 2.51 x 10^{-3} nm respectively.

The development of the microscopes, and the improvement of the accelerating voltage did not come only with benefits, but also with the knowledge that some samples need specific settings for the working microscope, as the structure of a sample can be damaged very easily with the high accelerating voltage (due to inelastic scattering). Examples for electron damage can be the biological samples, which need specific cooling when are investigated via electron microscope, or the graphite, whose structure is easily damaged above 80 keV [70,124,125].

The transmitted signals form the basis for TEM. A basic instrument is shown schematically in Figure 3.15

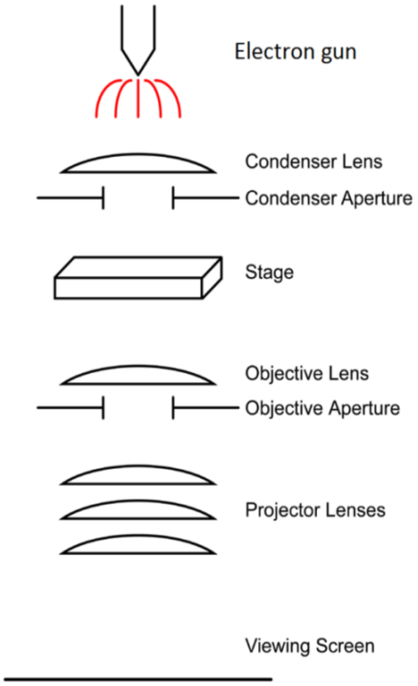

Figure 3.15 Typical construction of electron microscope column.

TEM has about 2 main working modes: image mode, and diffraction mode (Figure 3.16). Inside a TEM, electrons are transmitted through a very thin sample and, depending on the demands; the two working modes operate in different ways:

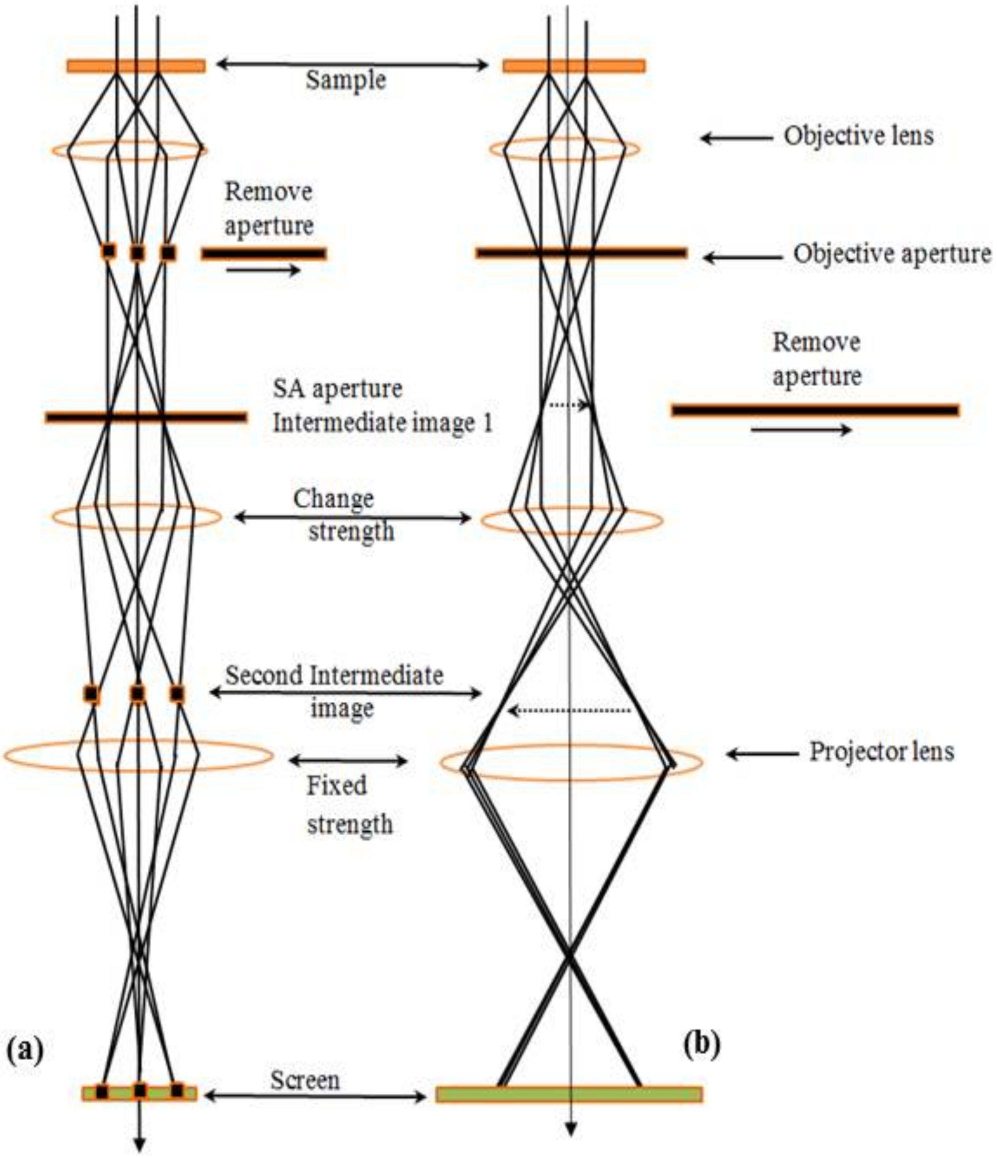

Figure 3.16 The two main operating modes in the TEM: (a) diffraction mode which provides DP and (b) image mode; (reproduced after [123].

(a) Diffraction mode - when the electrons are transmitted through the sample and diffracted by the internal structure. The diffracted electrons are converged by objective aperture in order to form the DP of the sample in the back focal plane.

(b) Image mode - when the electrons are traveling and transmitted through the sample, and the scattered electrons are converged by the objective aperture and meet in the focal plane, where the intermediate image is formed; a magnified image is then projected on the microscope screen showing the image of the sample.

I. Imaging modes

The imaging mode of the TEM is based on contrast: in a thick/dense sample, some areas will appear darker than the thinner areas due to the increased inelastic scattering/absorbed electrons; this is known as mass-thickness contrast.

Imaging using diffraction contrast can be performed in two ways. The first is the Bright Field method (BF) (Figure 3.17 (a)), where an aperture is inserted in order to let only unscattered beam to pass. The image is, based on the contrast in which the crystalline parts will appear darker if they diffract at the Bragg orientation or are amorphous areas. In crystals, the contrast is also given by the orientation of the crystal: for an orientation that satisfies the Bragg condition, the crystal will appear darker.

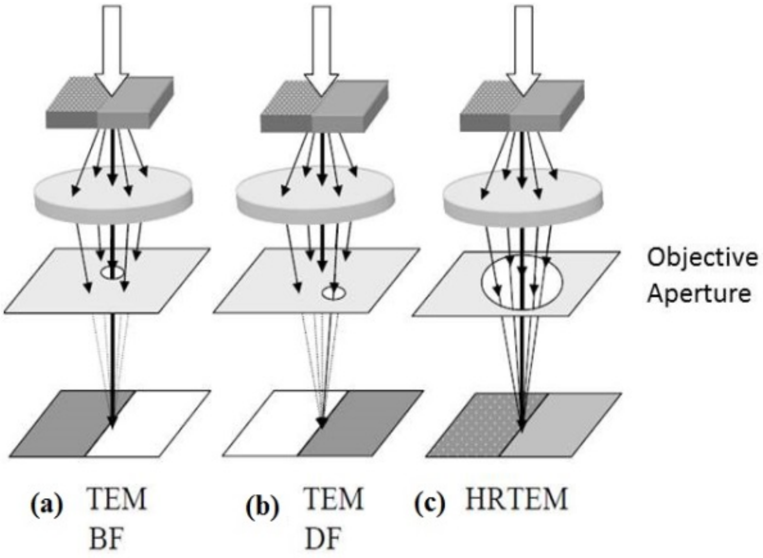

Figure 3.17 Image formation in the TEM, in different working modes: BF, DF and HREM.

The second image mode in which TEM works is the Dark Field mode (DF) (Figure 3.17. (b)). In this case, the aperture allows specific diffracted rays to pass, and stops the incident beam taking part in the image. The image contrast is opposite to BF. DF is applied when the defects or some specific structures in the specimen are of interest.

High Resolution mode (HREM) (Figure 3.17 (c)), permits the lattice image to be seen with atomic resolution. This mode uses both diffracted and undiffracted waves. The difference between this mode and the other two (BF and DF) is that it requires the information from several beams and not just from one. In fact, the more beams used, the greater the resolution. This type of imaging is called phase-contrast imaging. When the beam passes through a very thin sample, the phase changes by +/- π/2 because of scattering but maintains its amplitude. The difference in phase causes the recombined beams to exhibits an interference pattern that corresponds to the lattice.

II. Electron Diffraction mode

Electron diffraction is based in the elastic scattering of electrons by the crystallographic planes of a sample, and the formation of DP follows the same rules as for the X-ray diffraction presented in section 3.2 .

The region of the sample, which forms the diffraction pattern, can be defined by use of a selected area (SA) aperture located in a intermediate image plane (see Figure 3.16). This gives spatially resolved crystallographic information from areas ranging from 0.2 μm to a few microns.

III. Electron Energy Loss Spectroscopy (EELS)

In EELS mode, incident electrons interact with the specimen are inelastically scattered and lose part of their energy. These scattering events carry with them a huge amount of information about the electronic structure of the sample, and all aspects associated with it (e.g. atomic structure, free electron density and specimen thickness). The transmitted scattered electrons are dispersed using and magnetic electron spectrometer (Figure 3.18).

An electron from the incident beam can lose part of its energy to the sample in one of three ways: first (and most likely), it is the plasmon excitation event, which will happen by inducing a collective excitation of the outer shell electrons (the valence electrons); second, it is by ionising an individual atom up to the excitation of an electron from a core level to the conduction band (above the Fermi level); and third, it is by excitation of the entire atomic lattice by exciting phonons.

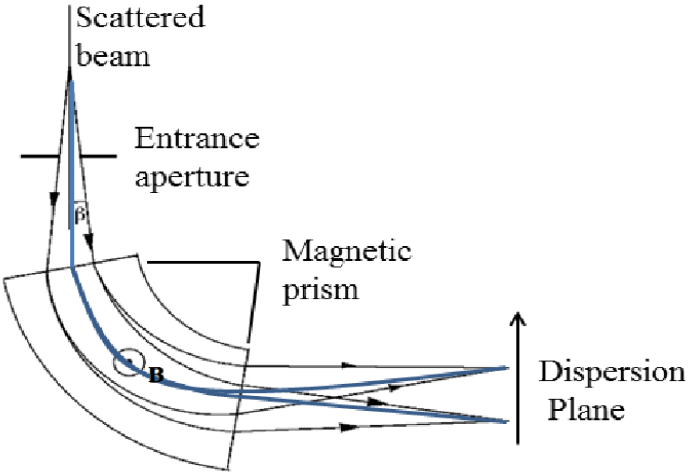

Figure 3.18 Geometric representation of the magnetic prism spectrometer and the focusing signal of energy-loss electrons in the image plane.

For a particular energy loss event (or energy loss electron) the characteristic scattering angle - θ_E is defined in mrads [123]. If the relativistic effect of the fast electrons is ignored the characteristic scattering angle may be approximated by:

$$\theta_E = \frac{E}{2E_0} \qquad \text{Eq. 3.8}$$

where E_0 is the primary beam energy [126].

As EELS is conducted in a TEM, which can provide a high spatial resolution, the collected spectra can give information from a small area of the sample. However, the technique is still very valuable as it provides structural information on chemical bonding, or nearest-neighbour distribution once the spectrum has been analysed [123].

The EELS spectrum is divided into two main regions, low-loss (energy losses below 50eV), and high-loss (energy loses above 50 keV) (Figure 3.19). The high energy loss region is further divided into the ELNES (electron energy near-edge structure) and EXELFS (extended electron energy loss fine structure) on specific ionisation edges associated with a particular event in the sample (each of which occur at a characteristic energy) [68,123,127]. For this thesis, the low-loss and ELNES regions are of interest.

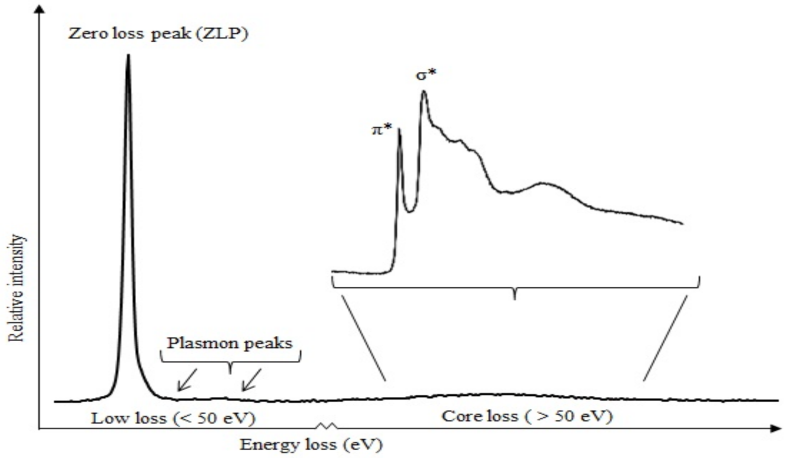

Figure 3.19 A characteristic EEL spectrum of a carbon sample. First part of the spectrum represents the low loss, followed by the core-loss at higher energies.

A. Low-loss region of carbon

The low-loss includes the most intense feature of the entire spectra, the zero-loss peak which contains the elastically scattered electrons. The zero low loss full width half maximum (FWHM) is also indicative of the energy spread of the electron source, or resolution of the spectrum. The second most intense feature of the low-loss part of the spectrum is the plasmon. This feature is split into two regions as illustrated in Figure 3.20.

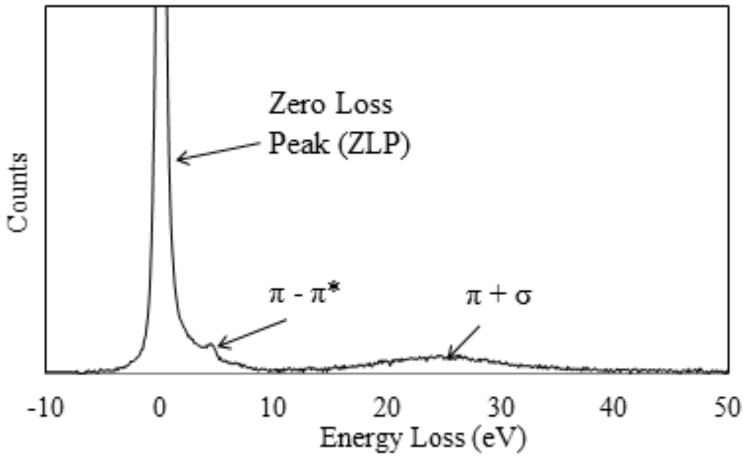

Figure 3.20 Low Loss spectra of a carbon sample with the π-π* peak, specific for graphitic material and π-σ bulk plasmon peak.

The first region of interest in this case is the π-π* interband transitions (and π plasmon) of around 6.5 eV [127] . This feature is due to the presence of π type bonds within a specimen, which in carbonaceous materials is due to the existence of sp^2 hybridised carbon. The second region is the valence plasmon peak, or π+σ, due to all the valence electrons. The position of the plasmon peak at ~27eV [126,127] is related to the changes in structural or chemical phase, crystallite size, and hence valence electron density (N), the latter of which can be calculated [128–130] by :

$$E_p = \frac{h}{2\pi}\left(\frac{Ne^2}{m_0\varepsilon_0}\right)^{\frac{1}{2}} \qquad \text{Eq. 3.9}$$

where h is the Planck's constant, e is the electron charge, m_0 is the electron mass, and ε_0 is the permittivity of free space (assuming a 'free electron' system) [127].

B. Carbon core-loss region

The ELNES carbon K - is due to the excitation of the 1s electrons to unoccupied p-states found above the Fermi level. It is dependent on the atomic structure [123,126,127]. For graphite the ELNES exhibits two main features: the π* peak (~284-285 eV), and the σ* peak (~288-291 eV) as illustrated in Figure 3.21 [131,132]. The C K ELNES presents interest not only for the bonding information which are contained by

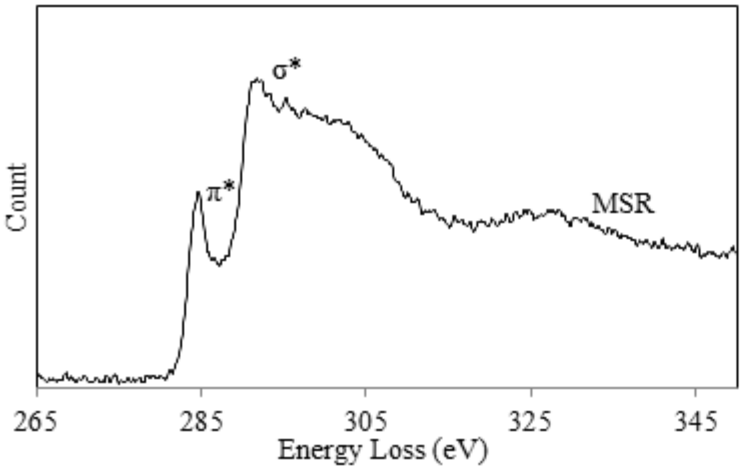

Figure 3.21 Representative typical crystalline graphitic core loss spectrum

the two main peaks (π* and σ*), but also for the ease of distinction between amorphous and crystalline materials [132,133].

C. Magic angle and the orientation independent conditions

Following Berger and McKenzie's proposal in 1988 of using the "two window method" to subtract the sp^2 content from isotropic carbonaceous materials, different methods have emerged to quantify the sp^2/sp^3 in more anisotropic materials, such as graphite [134,135]. During the years, the most significant improvement was acknowledging the spectral dependence of the intensity of ELNES features on sample orientation, which gave, rise to the use of specific working conditions at the orientation independent collection angle or 'magic collection angle' (MA). Researchers observed that not only the orientation of the sample relative to the incident beam can influence the output results, but also the acquisition parameters.

In 1998 N. Manon *et al.* [136] used graphite as study material (theoretical and empirical) to analyse the influence between the convergence and collection angles on the orientation dependence of the spectra. They concluded that the orientation independence should be achieved at MA = $4\theta_E$ (where θ_E represents the characteristic scattering angle defined by Eq. 3.8). C. Souche [137], found, by studying another hexagonal structure (boron nitride), a similar value for the orientation independence, $3.97\theta_E$. Theoretically Paxton [138] proposed a smaller value (MA = $1.34\theta_E$) than previously thought.

In 2003 H. Daniels [139] reported by experimental evidence, that at 200 keV the MA was ≈ $2\theta_E$. This was later confirmed by relativistic calculations [140]. P. Schattschneider done extensive theoretical calculation regarding the MA for a multitude of accelerating voltages (e.g. 0 – 400 keV), but unfortunately up to now, nobody proved empirically the theoretical calculations to be true besides the already known value at @ 200 keV [140–142].

D. Damage of carbon at high intensity voltage

TEM represents a useful technique to observe in real time the defects presented in the analysed material. The only problem is that electron irradiation can also produce atom displacements. Atom displacement can occur by two different processes: (a) through radiolytic processes associated with electron ionization and excitation or (b) through direct knock-on collisions with the nuclei [143]. In carbon materials such as graphite the main damage mechanism is knock-on - a ballistic event leaving the lattice with a Frenkel pair defect (vacancy plus interstitial). For an atom to get displaced the transferred energy should be higher that the displacement threshold energy. If the incident beam energy (E_{TEM}) is known, the damage threshold energy (E_D) can be calculated using

$$E_{TEM} = 0.25 \ \frac{m_c}{m_e} E_D \qquad \text{Eq. 3.10}$$

where $m_c = 1.994 \times 10^{-26}$ kg (the mass of carbon) and $m_e = 9.1 \times 10^{-31}$ kg (electron mass) [144].

During the years, the exact threshold energy for graphite was ill defined, with values ranging from 12 – 42 eV, resulting in a significant variation in the values for “safe” working voltages for TEM analysis. However Banhart has stated that energy threshold is in the range of 15 - 20 eV [145], corresponding to an electron energy of 82-100 keV.

3.4.3. TEM experimental details

Based on the discussion above, for non-damaging imaging and analysis of the graphitic structures, an accelerating voltage of 80 keV was chosen.

Generally the microscope is calibrated for operating at 200 keV. Hence, as part of this reason the microscope was fully calibrated at 80 keV in terms of collection and convergence angles, along with the magic angle. Details about the microscope calibrations and the magic angle found for 80 keV the reader is advised to see Appendix A).

Knowing the importance of the orientation independence for collection of the C K-edge data, the MA was checked and found to be 3.1 $\theta_{E,}$, in close agreement with the theoretical value of 2.6θ_E @80 keV found by Jouffrey *et al.* [142]. The working parameters of the microscope used when obtaining the MA at 80 keV are summarised in **Table 3.2,** where CL is the camera length, C2 is the lens current on the second condenser lens, β is the collection semi-angle, α is the convergence angle at 80 keV, β*is the effective collection semi-angle (the sum in in quadrature of β and α) and R is the spectrometer entrance aperture radius.

Table 3.2 Working parameters when obtaining MA at 80 keV.

Quoted CL (Real CL) (mm)	C_2 (mA)	β (mrads)	α (mrads)	β*(mrads)	R (mm)
115 (98)	**1107**	**5.40**	**1.13**	**5.52**	**2**

A. Imaging and diffraction modes – acquisition and data analysis

For the acquisition of the BF images and diffraction patterns a FEI Tecnai F20 field emission gun transmission electron microscope (FEG-TEM) was used, operating at 80 keV, and equipped a Gatan SC600 Orius CCD camera (Gatan Inc, Pleasanton, CA). All diffraction patterns were recorded using a camera length (CL) of 150mm at a magnification 50kX. For the HRTEM, the images were acquired at a magnification of 280k X.

Structural characterization of materials can be achieved by analysing the reciprocal space, using selected area electron diffraction (SAED). In addition to the high-resolution images, electron diffraction can provide structural information not only on the **c** lattice parameter but also the **a** lattice parameter.

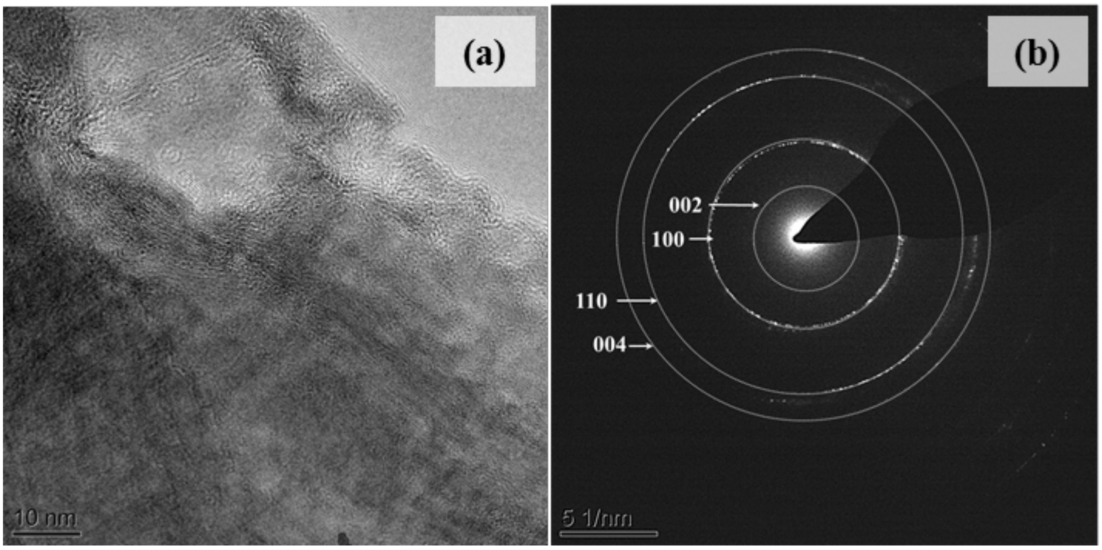

Figure 3.22 BF image of virgin PCEA (a) with its indexed DP(b)

Figure 3.22 (b) shows the typical indexed electron diffraction pattern of a polycrystalline graphite sample. For the purposed of this thesis the (002) and (100) were measure and used in calculation of the lattice constants **a** and **c** respectively.

The difficulty to find thin and large enough areas overhanging holes in the amorphous carbon film was high, as the grinding procedure for preparing the TEM samples had to take in consideration both the time of the β radiation exposure of the user, the radiation waste produced, and the fact that the graphene sheets tend to conglomerate.

Figure 3.23 (a) shows a high resolution TEM phase contrast image, clearly demonstrating the arrangement of the atomic columns within a near perfect PCEA graphite crystal. The stack of columns shown in yellow in Figure 3.23 (b) has been obtained by taking Fast Fourier Transforms (FFT) of an area from the original image (a procedure performed in Digital Micrograph). The FFT was filtered for the intensity of the first order spots from the diffraction pattern, which describes the spatial frequencies of the (002) planes contained in the original image, after which an inverse FFT function was used to return to real space.

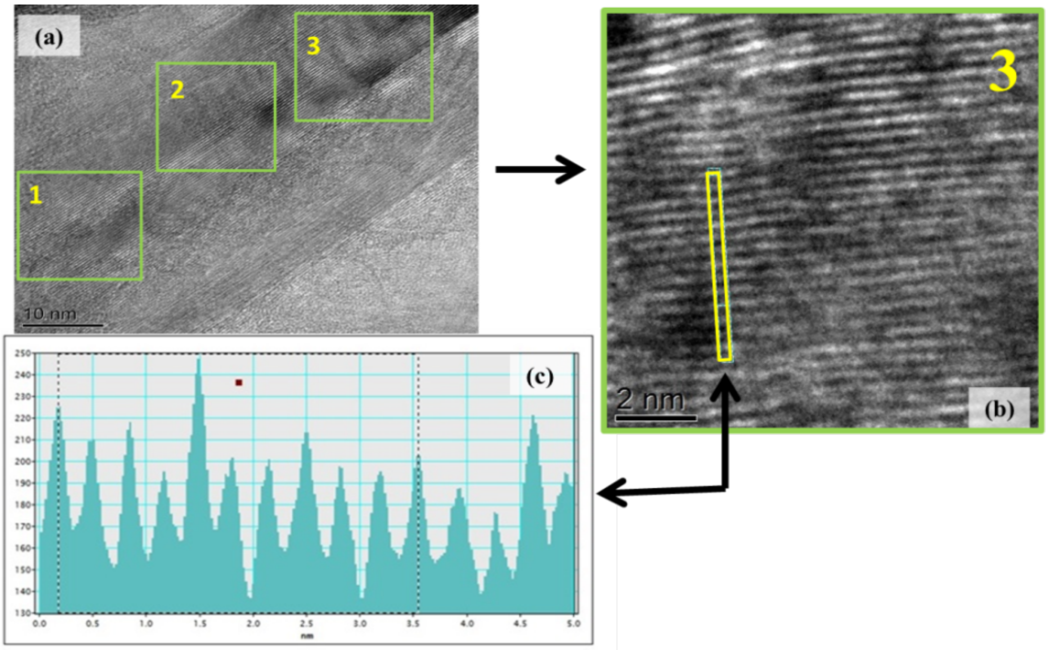

Figure 3.23 (a) HRTEM image of a long PCEA crystallite; (b) Fourier filtered image of the area of interest (highlighted in (a) in green square 3); (c) intensity profile of an integrated line profile (highlighted in (b) in yellow rectangle.

By following this procedure, no extra information was added to the resulting image, but it just allowed easier measurement of image intensity profiles (Figure 3.23 (c)) in the area integrated in the yellow rectangle in Figure 3.23 (b). Both original images and Fourier filtered images are shown in the thesis.

B. EELS data analysis

The EEL spectra were collected on a FEI CM200 FEG-TEM operating at 80 keV, equipped with a Gatan GIF 200 imaging filter camera. The used TEM working parameters when in EELS mode can be seen in **Table 3.2.**

The position of the π^* peak for all C K-edge spectra was energy calibrated to 285 eV following background subtraction. Each C K-edge spectrum was acquired along with the corresponding low-loss peak, which was used to deconvolute the K-edge spectrum to remove plural inelastic scattering. Data extracted from the spectrum acquired from a standard HOPG sample under the same experimental conditions, was used to normalise subsequent carbon sp^2 content using Eq. 3.11.

An improved automated fitting routine for was achieved by adding two Gaussian curves to the existing method proposed by Zhang [135] which involved the use of three Gaussian peaks (Figure 3.24 (a)). The additional two Gaussians were positioned under the initial "residual" peak (~286 - 288 eV) described by Zhang's method. This intensity was ascribed to either: from the asymmetric nature of the sp^2 planar component arising from curvature of the graphene planes, or from the presence of additional species (e.g. O or H). The three Gaussians had the following significance: G1 ~285 eV, was fitting the planar C=C π* component; G2 ~292 eV the C-C σ* component and G3 ~300 eV the C=C σ* component.

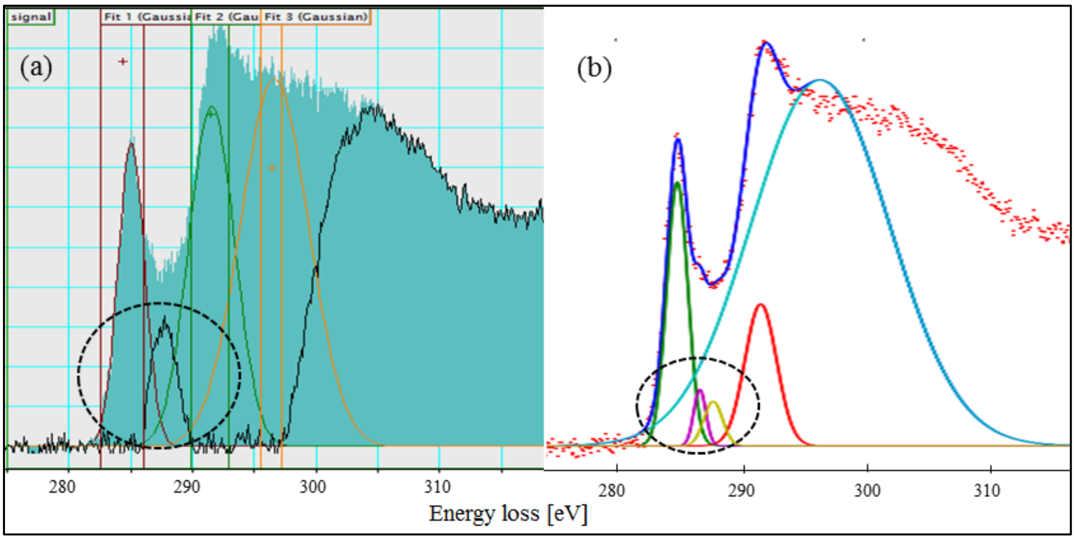

Figure 3.24 (a) Circled residual peak signal from 3 Gaussian fit performed in Gatan Digital Micrograph (b) Circled residual peak signal from 5 Gaussian fit performed in Hyperspy. The residual peak from (a) was deconvoluted into two separate peaks in (b).

All five Gaussians were fitted simultaneously using the following constraints:

- the first Gaussian (G1) centred at ~284.5 eV (with a constraint on the FWHM (X): 0.25 eV ≤ X ≤ 2 eV);

- second Gaussian (G2) centred at ~291.75 eV (2.1 eV ≤X ≤ 3.0 eV);

- third Gaussian (G3) centred at ~297.75 eV (11.2 eV ≤ X ≤ 13.1 eV).

While fitting the extra two Gaussians (G4 and G5), the script fixed the FWHM and the centre of G1, G2 and G3 along with the area of G2 and G3, but allowed the area of G1 to change in order to accommodate the new components, which were fitted using the following constraints:

- G4 centred at ~286.5 eV (0.2 eV $\leq$X $\leq$ 1.5 eV) ;
- G5 centred at ~288.5 eV (0.2 eV $\leq$X $\leq$ 1.5 eV).

It will be seen later, that in the analysed samples these two Gaussians (Figure 3.24 (b)) change not because of the presence in the sample of different species, but more because of the curvature of the graphitic basal planes.

The variation of planar sp^2 content was then calculated by comparing the ratio of the π^* intensity (G1) with the total C K-edge intensity (integrated over a 20 eV window from the edge onset at 282.5 eV) which is proportional to the total number of carbon atoms present in the probed volume:

$$\text{Planar sp}^2\text{ content} = \frac{\frac{I_{\pi*}}{I_{\pi*+\sigma*}}}{\left(\frac{I_{\pi*}}{I_{\pi*+\sigma*}}\right)_{\text{th}}} \qquad \text{Eq. 3.11}$$

where an average of 10 intensity values from different HOPG C K-edge spectra were used to calculate $(I_{\pi^*} / I_{\pi^*+\sigma^*})_{th}$, to ensure all spectral changes were relative to a “perfect” 100% sp^2 structure.

Chapter 4 Methodology of simulating neutron irradiation by in- situ electron irradiation of nuclear graphite

Throughout this section electron irradiation it will be referred in three ways: fluence refers to the number of electrons that intersect a unit area (e m^{-2}); flux is the fluence rate (e m^{-2} s^{-1}); and dose (dpa – displacements per atom) is the energy transferred fluence. To determine the dose experienced by a material in a transmission electron microscope, the electron intensity, I, must first be calculated using:

$$I = \frac{1875 \times 10^{12} \times \tau \times \varepsilon}{t_e \times C \times e} \qquad \text{Eq. 4.1}$$

where τ is a constant associated with the operating voltage (1.3 at 200 keV), ε is the emulsion setting (set to 2 during TEM operation), t_e is the exposure time, C is the screen size correction factor (≡1) and *e* is the electronic charge (FEI 2011). To convert this to an electron fluence, J, the beam area, A, must be determined to give

$$J = \frac{I}{A} \qquad \text{Eq. 4.2}$$

which involves an error of approximately ± 6.4% due to uncertainty associated with the exposure time reading (typically ± 5%) and beam radius measurement (typically ± 4%). The dose, D (in dpa), is then calculated using Eq. 4.3.

$$D = J \text{ x } \sigma_d \qquad \text{Eq. 4.3}$$

where σ_d is the displacement cross section, representing the quantitative analysis of the radiation damage induced by charged particles in crystalline materials and defining the displacements of atoms from the atomic layers, carbon atoms in the present case.

The displacement cross section varies with changing the electron energy and displacement threshold energy, E_{dt}. Displacement cross section was measured referring to Figure 18 from Oen (1965) [146] (Appendix C) and found to have a value of 16.25 barns assuming an electron energy of 200 keV and a displacement threshold energy of 20 eV [144]. A précises value of E_{dt} has not yet been agreed upon within the literature, with values ranging from 15 – 25 eV, resulting in a significant variation in σ_d and therefore in resultant dose calculations [62,127,144,145].

4.1. Electron irradiation data analysis

During EELS experiments, the intensity of the beam was varied considerably for the acquisition of the low loss and core loss regions, which resulted in an inconsistent electron flux. During the acquisition of low loss spectra the beam was spread over a large area to give a low intensity (so as to avoid saturating the detector) resulting in a near-negligible flux; when collecting the core loss however, the beam was focused to a smaller area giving a much higher intensity which is comparable to the intensity during imaging. The change in fluence was accounted for by measuring the electron flux at the two acquisition intensities and recording the time spent at each; the cumulative fluence was then determined and converted to dpa. The change in dose over time is illustrated

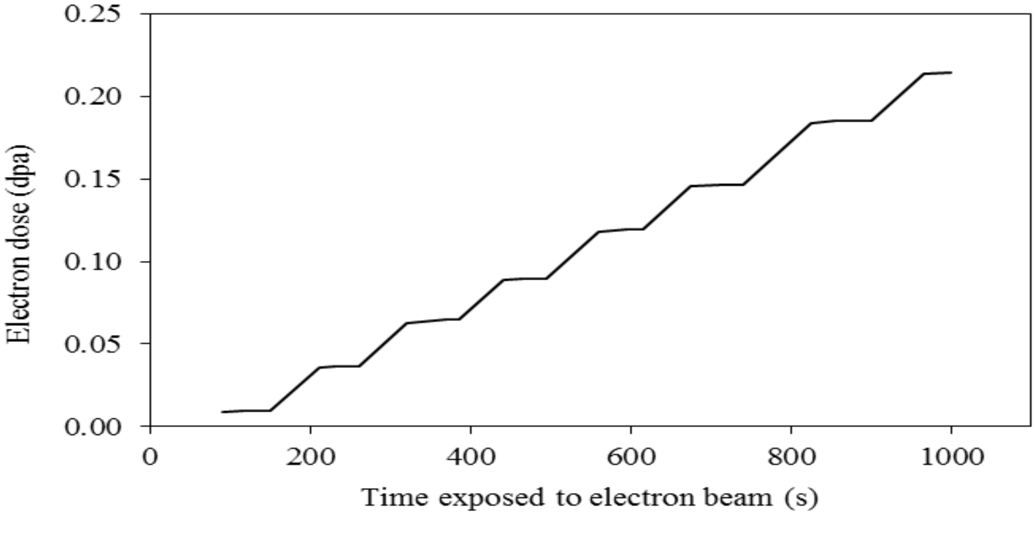

Figure 4.1 Change in dose with respect to time under the electron beam (dose error = ±6.4%). The plateaus and slopes respectively describe the dose rate during low loss and core loss acquisition periods

in Figure 4.1 where the plateaus and slopes respectively describe the dose rate during low loss and core loss acquisition periods.

Four areas of thin (<50 nm) PGA graphite were subjected to an average electron fluence of 4.2 x 10^{18} electrons cm^{-2} s^{-1} (2.4 x10^{-4} dpa s^{-1}). Electron micrographs and electron energy loss spectra were recorded periodically throughout.

The micrographs and their corresponding selected area electron diffraction (SAED) patterns shown in Figure 4.2 are typical of the damage produced by a 200 keV electron beam. These micrographs are comparable to those obtained by Karthik and Kane [62] and Muto [77] who also investigated the effects of electron irradiation to nuclear graphite.

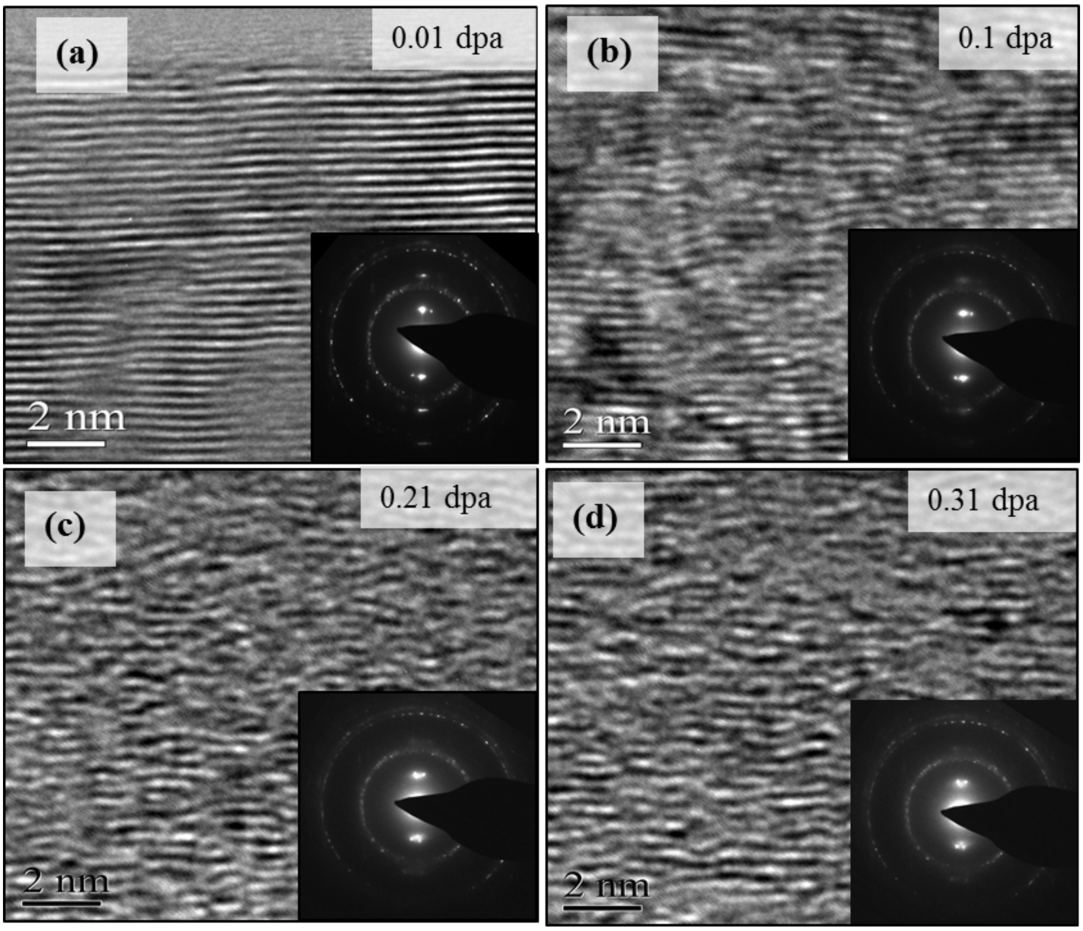

Figure 4.2 (a) – (d) Electron micrographs of PGA graphite with their corresponding SAED patterns during electron beam exposure at 200 keV and room temperature, receiving 4.2 x 10^{18} electrons cm^{-2} s^{-1} (2.4 x10^{-4} dpa s^{-1} ± 6.4%).

Diffraction patterns were also recorded at regular intervals during electron beam exposure. It was observed a change of the DP from defined spot rings (at t=0) to defuse spot rings at the end of the experiment, with the mention that even though the image changed from stuck of fringes to disordered material, the DP kept the arrangements of the graphite rings, which is a good correlation with the findings by EELS that will be seen further on in this thesis. The bulk π+σ valence plasmon peak in the low loss region of the spectrum was analysed; the position of the peak being determined by taking the first derivative of the spectrum. The widely agreed value for the bulk plasmon peak position of highly oriented pyrolytic graphite (HOPG) in the literature is 27 eV [68,129,147,148] (for comparison, the corresponding value for amorphous carbon is 23 eV).

As illustrated in Figure 4.3, the plasmon peak energy for PGA graphite is consistently lower than for HOPG. This situation may be due to the misorientation of the specimen's c-axis relative to the normal of the incident beam [149], in combination with the choice of the spectrometer collection angle [126,127]. During the experiments the position of the plasmon peak seems to be unchanged, or perhaps slightly decreases, as a function of dose to within experimental error.

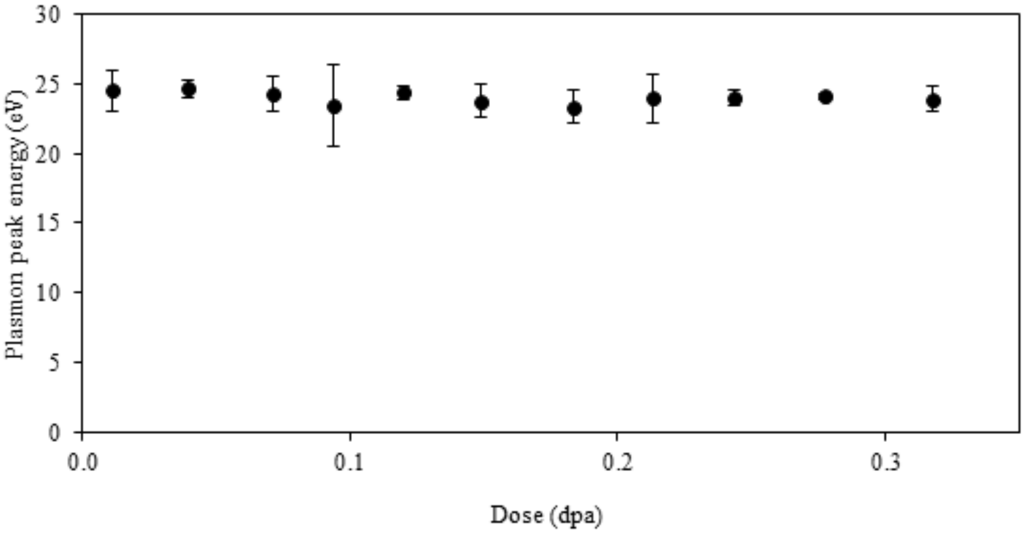

Figure 4.3 Change in plasmon peak position with dose. Data is averaged over two regions of electron transparent (002) oriented PGA graphite. The error bars reflect the experimental variance. Dose error = ± 6.4%

A representative set of EELS C K-edge spectra as a function of electron irradiation is presented in Figure 4.4 (a) - (d). The π* peak maximum of all spectra was calibrated to 285 eV, and a C K-edge spectrum was acquired every 90-100 seconds along with the corresponding low loss peak which was used to deconvolute the K-edge spectrum so as to remove plural scattering. The data extracted from the spectrum acquired at t=0 was used to normalise subsequent sp^2 content data. Note that even after extensive electron irradiation damage, and even though the σ* component appears to undergo considerable change with a reduction of the graphitic order, the presence of the π* peak indicates that the structure retains a distinct sp^2 character.

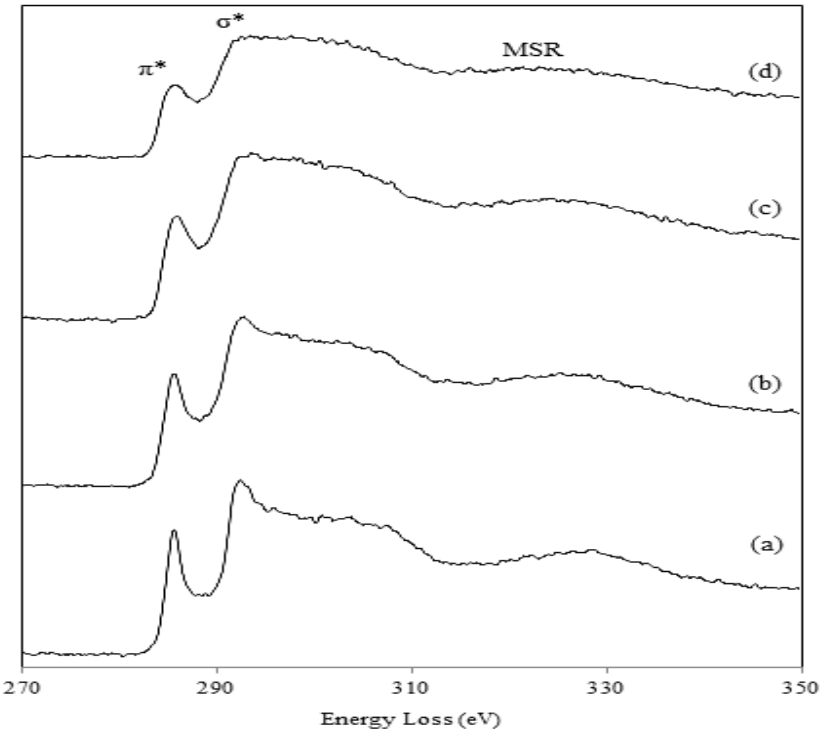

Figure 4.4 Change in EEL spectra with dose (D): (a) D = 0 dpa; (b) D = 0.113 dpa; (c) D = 0.209 dpa; (d) D = 0.267 dpa ± 6.4%.

To characterise the ratio of (planar) sp^2 bonded carbon to total carbon from the C K-edges the improved method described in the previous chapter was used.

The variation of planar sp^2 content was calculated by comparing the ratio of the π* intensity (G1) with the total C K-edge intensity (over a 20 eV window of onset 282.5 eV) which is proportional to the total number of carbon atoms present in the probed volume:

$$\text{Planar sp}^2\text{ content} = \frac{I_{\pi*}}{I_{\pi*+\sigma*}} \Big/ \left(\frac{I_{\pi*}}{I_{\pi*+\sigma*}}\right)_{t=0} \qquad \text{Eq. 4.4}$$

where the intensity values from the initial C K-edge spectrum were used to calculate $(I_{\pi*} / I_{\pi*+\sigma*})_{t=0}$ so as to ensure all spectral changes were relative to the initial structure.

As can be seen in Figure 4.5 the sp^2 content changed approximately linearly with respect to electron dose. The sp^2 content dropped to below 80% of its original value after a dose of at least 0.25 dpa. In the most extreme case the sp^2 content dropped to 76% following an exposure of 0.32 dpa, a value consistent with the typical value of 75% sp^2 derived for amorphous carbon using this fitting method. These changes provide evidence for the introduction of atomic disorder as a result of electron beam exposure.

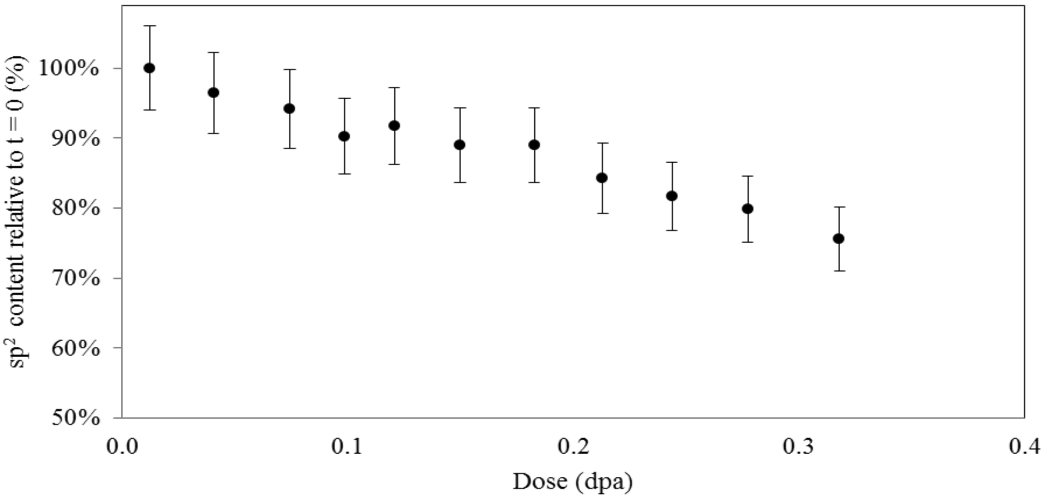

Figure 4.5 Change in sp^2 content with electron dose. Data was analysed using the 5 Gaussian fitting method and averaged over four regions of electron transparent (002) oriented PGA graphite. The error bars reflect the experimental variance and analytical error. Dose error = ± 6.4%.

The signals from the G4 and G5 peaks were analysed to provide information regarding the non-planar sp^2, or fullerene, content of the specimen by measuring the ratio between the combined intensity under G4+G5 signal integral (I_R) and the (I_R+sp^2) integral (the combined intensities under the G4, G5 and G1 peaks) detailed in 2.3.2.This ratio represents the proportion of sp^2-bonded carbon atoms which are bonded in a non-planar fashion and the increase in this quantity with increasing electron dose is plotted in Figure 4.6. Comparing the data in Figure 4.5 and Figure 4.6, it appears as though the loss of planar sp^2 bonding (very roughly a 20% decrease) is predominantly accounted for by an increase in non-planar sp^2 bonded carbon.

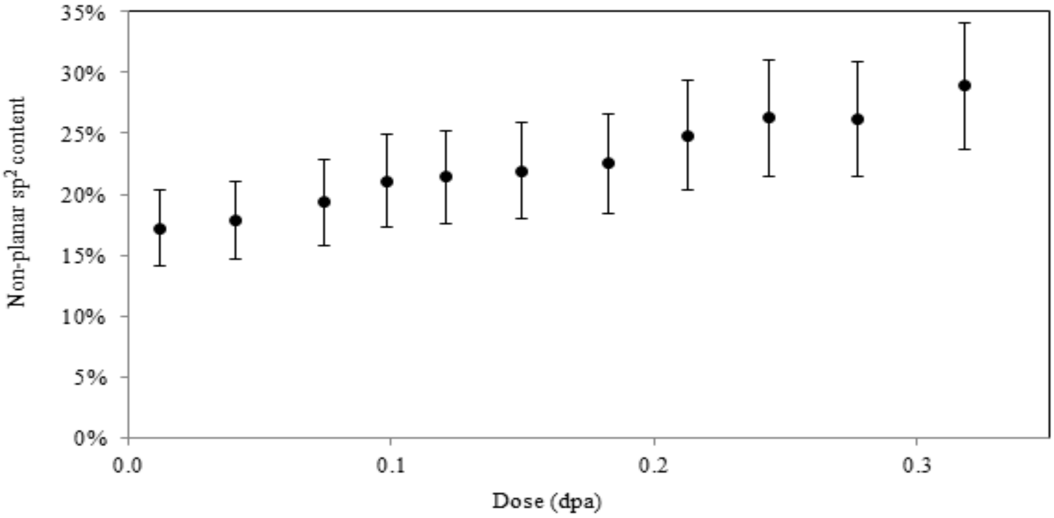

Figure 4.6 Change in non-planar sp^2 content with dose over two regions of electron transparent (002) oriented PGA graphite. Error bars reflect experimental variance and analytical error. Dose error = ± 6.4%.

The errors shown in Figure 4.5 and Figure 4.6 reflect an analytical error of ± 6%, determined by slightly varying the energy window (G1) to account for subjective discrepancy due to the operator's choice of constraints (no significant change in data with varying the constraints for the other major windows (G2 and G3) was noticed). The error values also take into consideration the small variation in data between four separate experiments. This proves that the subjective nature of EELS experimentation and analysis does not affect the outcome data significantly.

The findings revealed by the proposed fitting method, of the changes in the planar and non-planar sp^2 bonding, are supported by the HRTEM images collected simultaneously with the EEL spectra (Figure 4.2), highlighting an increased in the plane buckling with irradiation, due to the alteration in ratio of the planar to non-planar sp^2 content.

Taking the first derivative of the C K-edge spectrum to analyse the change in the Multiple Scattering Resonance (MSR) peak position during the electron beam damage series, it was observed a slight decrease in energy relating to an increase in C-C bond length (Figure 4.7).

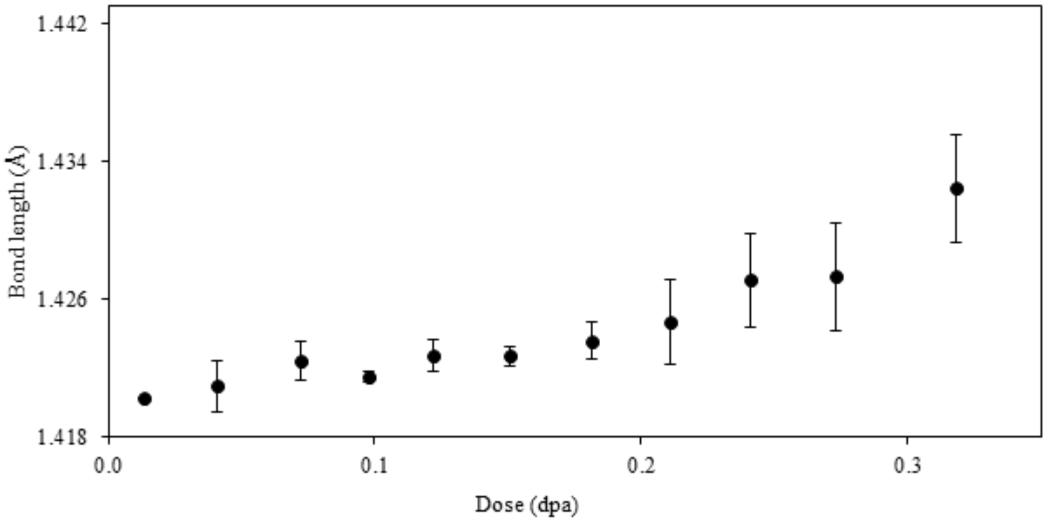

Figure 4.7 Change in MSR peak position with dose over two regions of electron transparent (002) oriented PGA graphite. Error bars reflect experimental variance and analytical error. Dose error = ± 6.4%.

The error associated with this data increases for higher doses where the MSR peak becomes wider leading to a degree of ambiguity; the error bars in Figure 4.7 represent experimental variation.

Results obtained by Daniels [134] following a series of graphitization experiments are analogous, whereby the graphite began as a highly disordered material with an average bond length of 1.435 Å and through annealing became a near-perfect structure with corresponding bond length 1.420 Å. In Daniels' case, the decrease in bond length during graphitization was attributed to a decrease in sp^3 bonding (bond length = 1.54 Å) and the removal of heteroatoms and aliphatic molecules (bond length > 1.42 Å). In the present case however, no heteroatoms and aliphatic molecules are introduced to the system and the high energy barrier between graphite and diamond phases makes sp^2 to sp^3 transformation unlikely unless at high temperature (~1000 K)

[150]. However, the electron irradiation induced atomic disorder, as observed in Figure 4.2, reduces the packing efficiency of carbon atoms which is thought to increase the average bond length (e.g. for the most extreme case of amorphous carbon, the bond length increases to 1.44 Å [151]). It is thus suggested that introduction of dislocations and defects along with the bending of planes following electron irradiation increases the average C-C bond length. Furthermore, it has been proposed that an increase in bond length could be attributed to a reduction in valence electron density (and thus the possible slight reduction in plasmon energy with increasing dose as shown in Figure 4.3) which may be associated with an increase in volume or the introduction of non-six-membered rings of carbon atoms [62].

Summary of electron irradiation of graphite

Using PGA graphite the damage produced at the atomic level has been studied, by using *in situ* electron irradiation at room temperature. This simulation method of neutron irradiation damage using electron irradiation, in addition with the use of an improved fitting data analysis, was used for a better understand of the behaviour of graphite moderators inside a nuclear reactor.

Analysis of the low and core loss of several EEL spectral series revealed little or no change in valence electron density, indicative of no change in phase of the investigated material due to irradiation. However a decrease in planar sp^2 content, to levels associated with amorphous carbon and an increase in non-planar sp^2 content, of inverse proportion to the planar sp^2 reduction, along with an increase in C-C bond length was observed, denoting a change in the physical structure of graphite due to electron irradiation with dose up to 0.3 dpa,

Chapter 5 Results and Discussions

Using the previously described methods and samples, different types of virgin nuclear graphites were analysed (PGA -Wylfa and Oldbury, Gilsocarbon, Ig-110, NBG-18) along with two series of irradiated and non-irradiated graphites, PCEA and PCIB. Primarily Raman spectroscopy and XRD techniques were used, in order to obtain initial details about the bulk structure of the virgin and irradiated materials. These methods are similar to those applied by researchers such as Niwase and Tanabe [50,51,75,76,78,152], who conducted studies on different types of irradiation (e.g. ion, electron and neutron irradiation) and their effects on nuclear graphite. For the irradiated materials and their virgin analogue, supplementary data was obtained by techniques such as electron diffraction, TEM image analysis and EELS (under the experimental conditions established in chapters 3, section 2.4.2.5.), providing additional information on the influence of neutron irradiation on graphite structure, and making possible the creation of a model on how the nuclear graphite behaves when irradiated at high temperatures and doses, which agrees with the studies of Muto and Tanabe [51,75,78].

5.1. X-ray Diffraction (XRD pattern)

XRD can provide information on the internal structure on both the crystallization and on the aggregation of the unit cell into crystallites. All the XRD data presented in this chapter was analysed using the reference file as described in Chapter 3.

5.1.1. XRD of virgin graphites

I. PGA

Figure 5.1 shows the two very similar indexed X-ray diffractograms obtained by XRD from the analysed graphite. Even though the samples were analysed as received, (bulk samples) and not crushed (as the reference data was), it can be seen that their structure has maintained a preferred orientation of the basal planes which are perpendicular to the (002).

In Figure 5.1 (b), the (101) peak presents a broader width compared to Oldbury, which can be due to the strain in the orientation due to smaller coherence lengths, as, can be seen in Table 5.1**.** Even if the analysed graphites graphite have similar d-spacing in both **a-** and **c**-directions, and are made from the same types of materials (pitch and petroleum coke), the different coherence lengths of the two can be translated into differences in porosity of the bulk materials hence a different response due to irradiation, as Simons, and Shtrombakh *et al*. suggested [8,54]. This hypothesis can be confirmed, only if further intensive analysis is done, to confirm the differences in coherence length and in porosity.

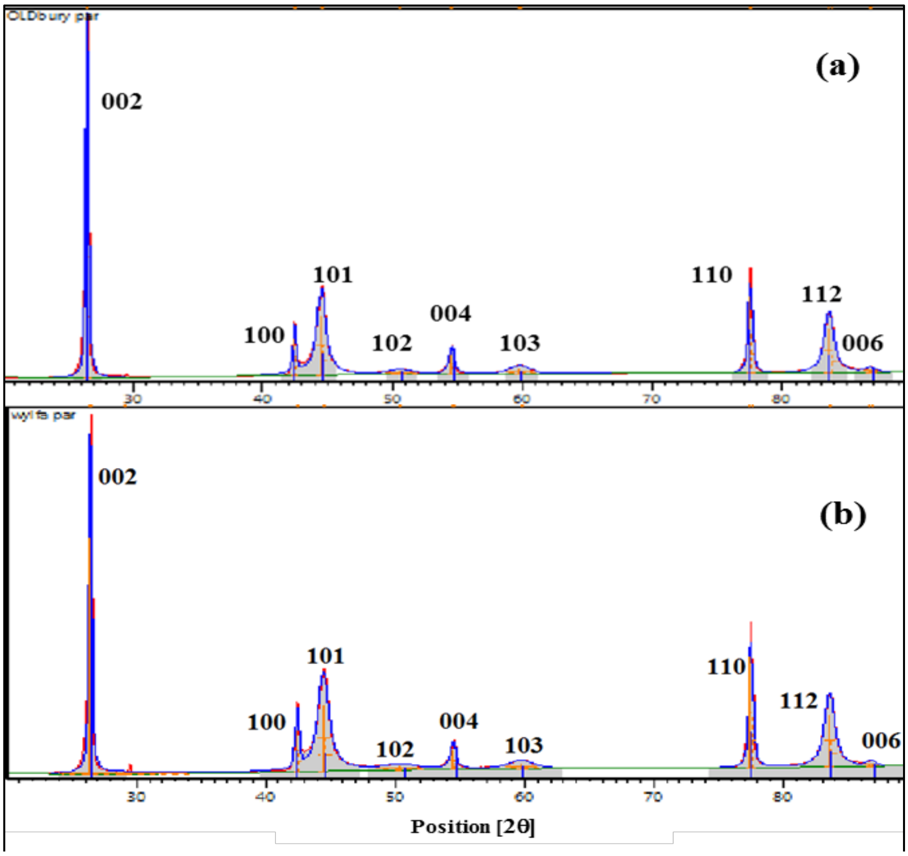

Figure 5.1 Diffraction patterns from the two PGA versions, (a) Oldbury and (b) Wylfa, with the fitting of the pattern applied in grey shading.

II. More XRD data on virgin nuclear graphite

Figure 5.2 shows the magnified X-ray diffractograms of five other virgin nuclear reactor graphites: PCEA, PCIB, GILSO, IG-110 and NBG-18 (see section 2.2.2).

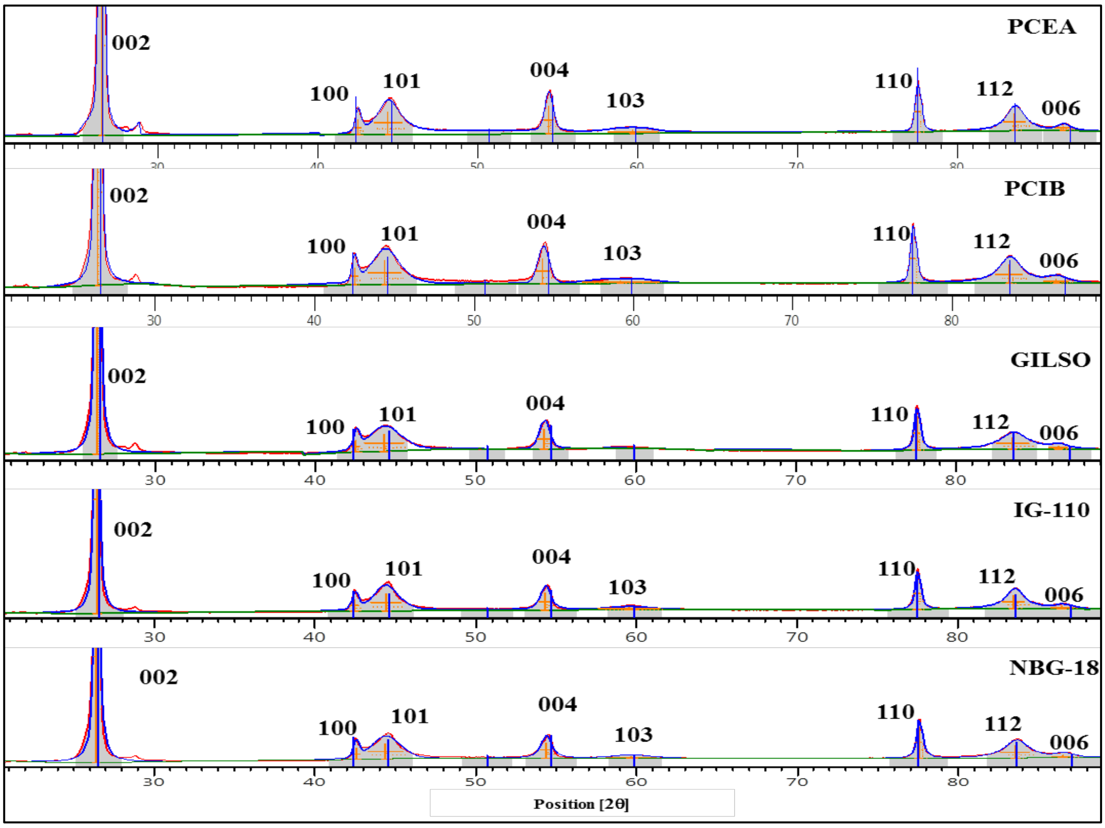

Figure 5.2 Comparison between XRD patterns of five different graphites with the fitting of the pattern applied in grey shading.

When comparing with the PGA graphites, all other analysed graphites in this section present a tendency to broaden and to loss intensity, all other peaks except the (00l) peak. This tendency is more noticeable in the (100) and (101) peaks, and the (103) peak, which for GILSO disappeared completely. The intensity of the (004) and (006) is increasing also, which means that all these types of graphite have a higher degree of orientation versus the old PGA. Also in Figure 5.1 and Figure 5.2, one can notice that the peak positions in Figure 5.2 are shifted towards lower 2θ relative to the peak positions of the theoretical value denoted in the patterns with a blue vertical line underneath each peak. This movement of the peaks can be noticed also in the lattice values obtained by fitting (Table 5.1).

Figure 5.3 is a comparison of the FWHM of the (002) peak versus the position of the same peak, measured from the X-ray diffraction pattern, through a range of different nuclear graphite grades. The analysis revealed that in comparison to HOPG, the most ordered and oriented graphite among the studied graphites, the other graphites had the tendency for an increase FWHM and moving towards lower 2θ, revealing a change in microstructure, more imperfect than HOPG's.

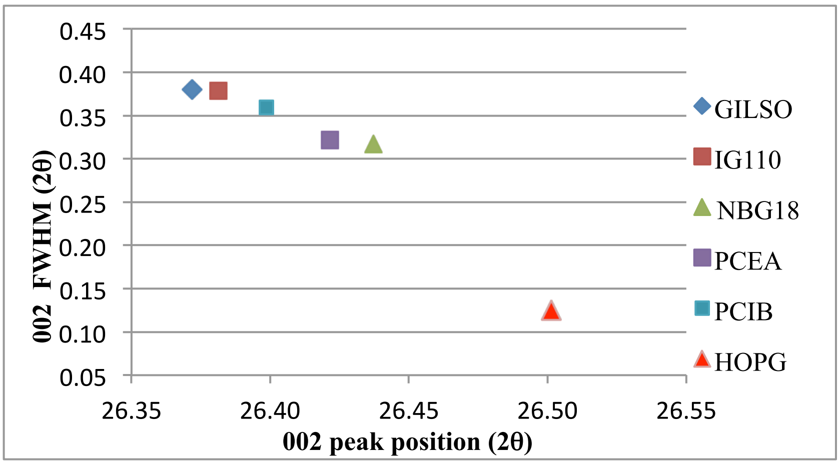

Figure 5.3 Comparison of (002) FWHM peak vs. the position of the (002) peak through a set of virgin nuclear graphites

The movement of the peak is not only due to a slight change in the lattice parameters, but could also be due to the strain in the lattice, from lowering the coherence length (crystallites) from ~2298.4 Å of the L_c of the HOPG, to ~ 206.8 Å of the Gilso, resulting in a larger fraction of atoms at the grain boundaries.

Figure 5.4 describes the variability within a sample of the interlayer spacing from three different graphites: Gilsocarbon (GIL), PCEA and PCIB. This variation in the crystallographic properties is following the expected trend described by Nigthingale [3]: the values obtained by measuring different points of the same graphite bar give distinctive values. For the PCIB and GIL in the **c**-direction, the d-spacing varies for similar values of the coherence length; for the **a** direction, the reverse is true, with the d-spacing keeping constant while the coherence lengths in the **a**-direction changes.

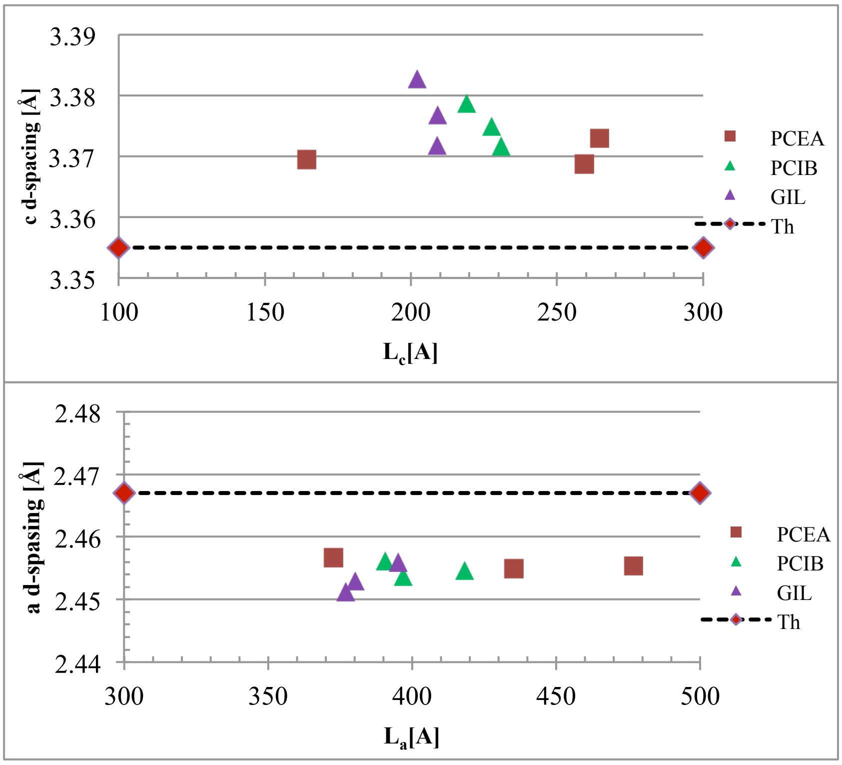

Figure 5.4 Variability within samples of the same graphite grade in: (a) (002) direction; (b) (100) direction

PCEA graphite exhibits in both cases, the **a-** and **c**-directions, a preservation of the d-spacing which could suggest a longer range isotropy and homogeneity compared to the other two analysed graphites. Despite the variability within a sample, it has to be noted that none of the three graphites sat down near the theoretical values of the perfect graphite, the (002) spacing is larger whilst the (100) spacing is smaller.

The obtained values for both crystallite sizes and lattice parameters are partially in agreement with the present literature: for PGA, PCEA and IG-110 even Zhou *et al.* [84] reported values of L_c higher than L_a, the L_c values being almost a perfect match with the calculated figures. Zheng *et al.* [153] reported data found for NBG 18 and IG 110, with the same agreement in the case of L_c, but underestimating the L_a. The L_c values and the lattice parameters are also in agreement with the extensive work that Seehra and Pavlovic have done on coal based graphites [154,155], but not the L_a value.

Nevertheless, according to Nightingale's research [3] L_a value has to be bigger compared to L_c, and from this point of view the values reported by him for PGA are in agreement with the obtained data for both L_a and L_c reported here. The calculations of

Nightingale's, on which this chapter is based, took into account a different shape factor when calculating the L_c and L_a values, as proposed by Warren in 1941 [82] but ignored by the authors mentioned before and hence their underestimations of L_a values.

Summary of XRD of virgin graphites

For all the analysed virgin graphites, a similarity of the lattice parameters was observed. However, the coherence lengths in both **a-** and **c**-direction vary. The ranges are 207 Å - 310 Å for the **c-**direction (excluding HOPG considered perfect graphite with $L_c > 2000$ Å**),** and 351 - 617 Å for the **a**-direction. The calculated values were partially in agreement with the literature, having the calculated L_a value consistently higher than the ones reported in the literature; this was understood to be due to the usage of different shape factor (k), the general used k value of 0.9 instead of 1.84, which should be used in the case of graphite. However if only $k = 0.9$ would be used, for both **a** and **c** direction, the obtained data for all the virgin graphite analysed will be in full agreement with the literature.

Table 5.1 Measured unit cell constants and coherence lengths for different NG.

Material	c-spacing (Å)	L_c (Å)	a-spacing (Å)	$L_a^{(100)}$(Å)	$L_a^{(110)}$ (Å)
HOPG	3.361 ± $6x10^{-4}$	2298.4	-	-	-
Oldbury	3.363 ± $2x10^{-4}$	310.2	2.458 ± $1x10^{-3}$	617.1	703.0
Wylfa	3.372 ± $3x10^{-4}$	300.4	2.460 ± $8x10^{-4}$	459.2	730.4
PCEA	3.370 ± $3x10^{-4}$	229.4 ± 56	2.456 ± $3x10^{-3}$	399.2 ± 49	646.6 ± 2
PCIB	3.375 ± $3x10^{-4}$	225.9 ± 6	2.455 ± $6x10^{-4}$	374.67 ± 14	618.9±38
GILSO	3.377 ± $4x10^{-4}$	206.8 ± 4	2.453 ± $3x10^{-3}$	384.2 ± 9	560.1±11
NBG-18	3.369 ± $5x10^{-4}$	207.7	2.452 ± $3x10^{-3}$	356.0	646.5
IG-110	3.375 ± $5x10^{-4}$	227.2	2.456 ± $3x10^{-3}$	351.3	612.1

5.1.2. XRD profile of irradiated graphite

Figure 5.5 shows the comparison between the magnified X-Ray diffractograms of the virgin PCIB, and the set of irradiated PCIB graphites. The irradiation dose (& temperature) increases from 1.5 dpa (C03) to ~6.8 dpa (B05). The diffraction profiles show that with irradiation, some peaks become broader or disappear completely (e.g. (103) or (006)). It can also be observed that the (100) peak is moving towards higher 2θ values with irradiation, and also changes its profile.

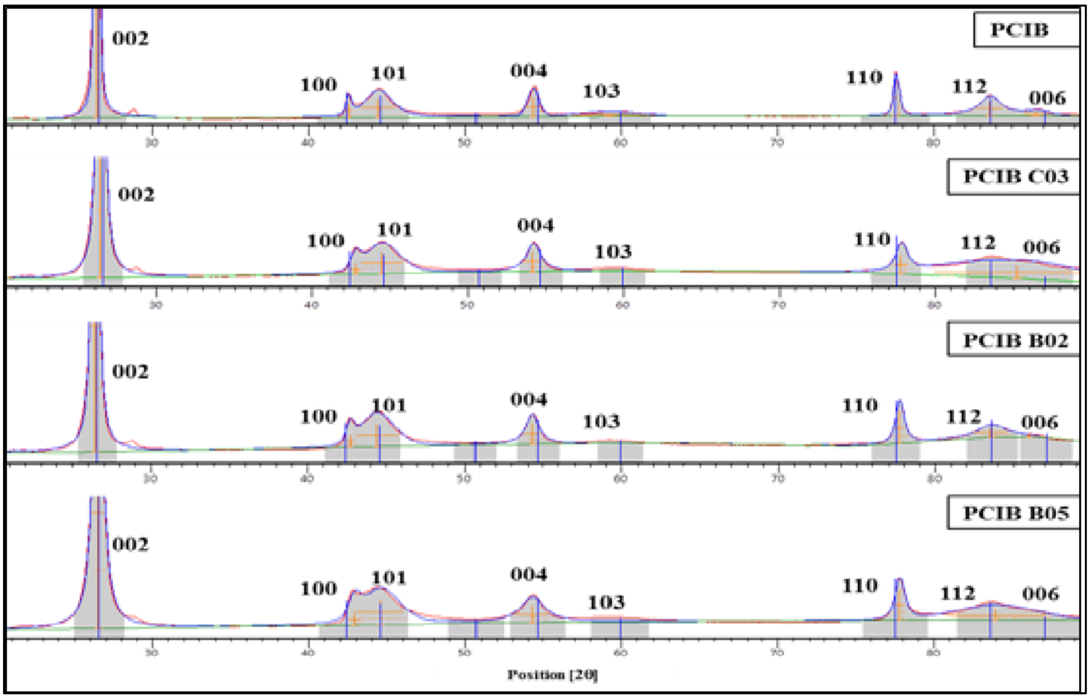

Figure 5.5 Comparison between XRD patterns of neutron irradiated series, starting from top with virgin PCIB, and following with increasing temperature and irradiation dose (~350,9 -> 657 C; 1,5 -> 6.5dpa).

The movement of the peak can be understood in terms of lowering of the lattice parameter (**Table 5.2**), and also in strain in the lattice, due to a decrease of the crystallites size L_a in particular.

For all the PCIB graphites analysed, the position of the (002) peak changes slightly, but similar to the other peaks for irradiated graphites, the (002) becomes broader with irradiation dose (with the highest FWHM at the highest dose – C03, 6.5 dpa), showing a decrease in the coherence lengths in the **c**-direction and a possible increase of strain in the lattice as a result of larger fraction of atoms at the grain boundaries Figure 5.6.

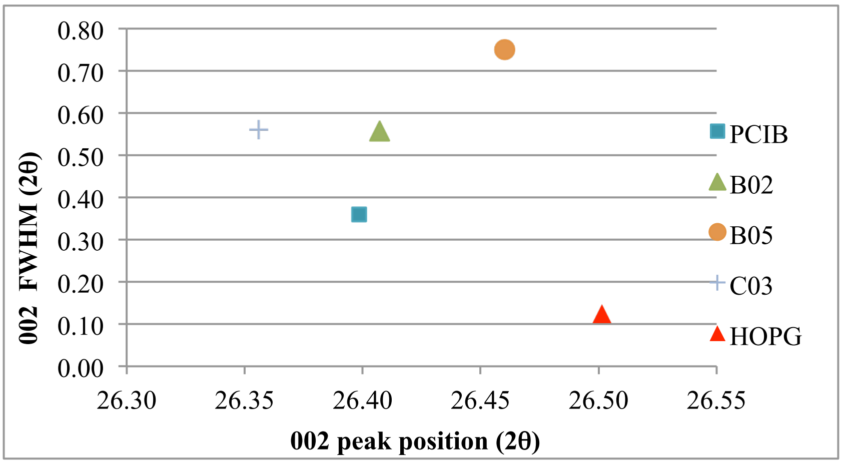

Figure 5.6 Comparison of PCIB (002) FWHM peak vs. the position of the (002) peak through the set of PCIB nuclear graphites, both irradiated and virgin.

The comparison between virgin PCEA and the set of irradiated PCEA graphites is shown in Figure 5. of the magnified X-ray diffractograms of all PCEA samples. The irradiation dose (/temperature) is increasing from 1.5 dpa (B25) to 6.8 dpa (B17). The refined parameters for PCEA graphites are shown in **Table 5.2.**

The X-ray diffractograms for the irradiated PCEA samples shows a movement lower 2θ of the (002) and (004) peaks and a broadening of all the (00l) peaks indicating an increase of the d-spacing, and a decrease in crystallite size in the **c**-direction.

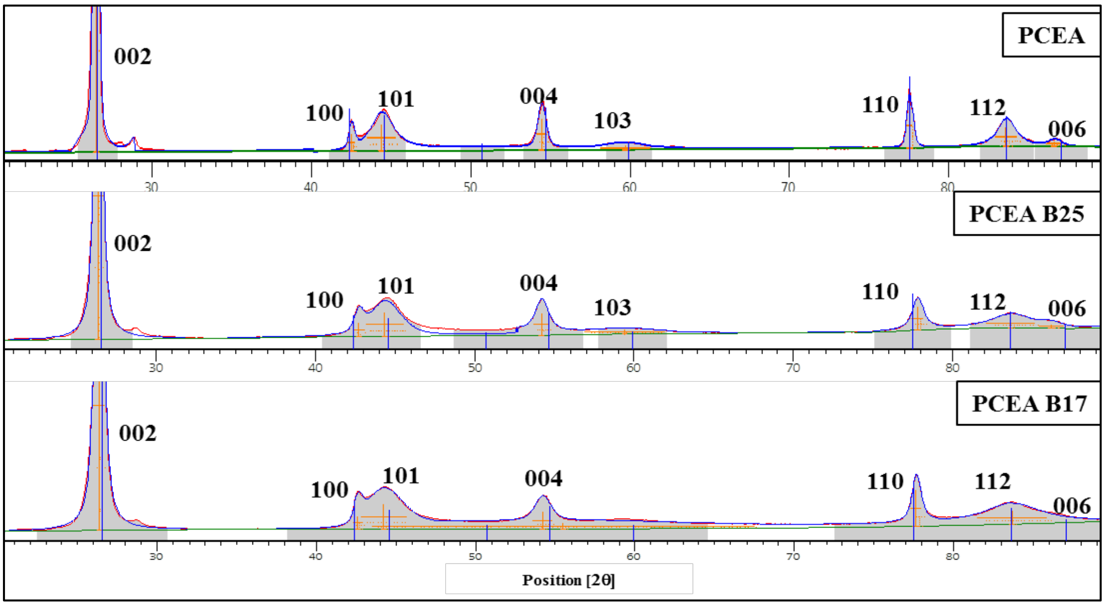

Figure 5.7 Comparison between XRD patterns of neutron irradiated series, starting from top with virgin PCEA and following with increasing temperature and irradiation dose (~350,9 -> 671 C;1,5 -> 6.8dpa).

Figure 5. represents the comparison between the (002) FWHM and the same peak positions through the set of PCEA sets of graphite, both irradiated and virgin. The change in microstructure due to irradiation is highlighted not by the peak position in PCEA case (which remains relatively constant), but by the FWHM increase with irradiation, presenting the highest value with the highest irradiation dose (6.8dpa) suggesting a fragmentation of the coherence length in the **c** direction (L_c) and a possible strain effect.

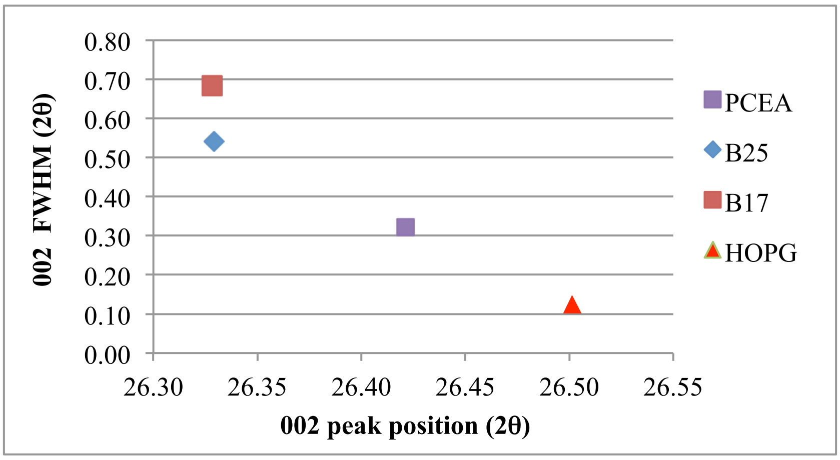

Figure 5.8 Comparison of PCEA (002) FWHM peak vs. the position of the (002) peak through the set of PCIB nuclear graphites, both irradiated or virgin.

A comparison between Figure 5.5 and Figure 5. shows a similarity between the response of PCEA and PCIB to irradiation environment. For both sets of irradiated graphites, all peaks get broader (relative to the virgin material) or disappear completely (e.g. (103)) and some peaks overlap entirely to each other (e.g. (006) and ((112)) or partially (the case of ((100) and (101)). Comparative plot of the two data sets analysed (PCEA and PCIB) in terms of the change in d-spacing with irradiation shown in Figure 5.7

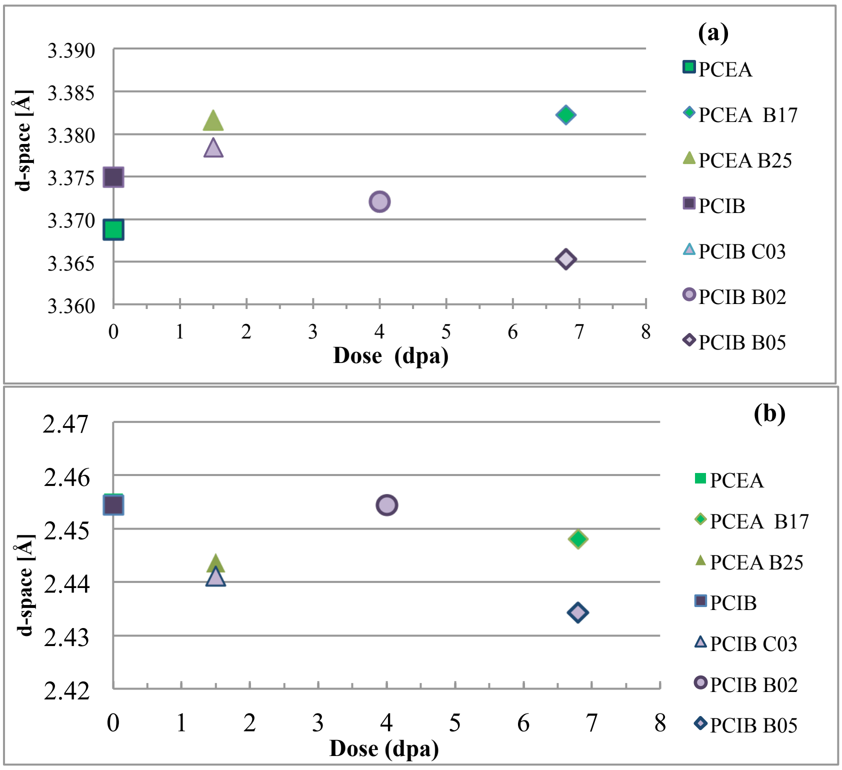

Figure 5.7 Change of d-spacing with dose (/temperature) in: (a) the c-direction and (b) the a-direction.

Figure 5.7 (a) shows the change of the d-spacing with the dose (/temperature) in the **c**-direction. For PCIB there is a swelling at the small dose of 1.5dpa (/~350 °C), followed by a continuous decrease at higher dose of 6.8 dpa (/~657 °C). For PCEA, the swelling started with 1.5dpa (/~350 °C), and decrease and then increased at 6.8 dpa (/~671°C). The decrease was not so evident as in the PCIB case. In Figure 5.7 (b) the d-spacing in the **a**-direction is presented: for PCIB the d-spacing decreased abruptly, then increased up to 4 dpa (/~534 °C) when it decreased again; for PCEA a similar behaviour was observed.

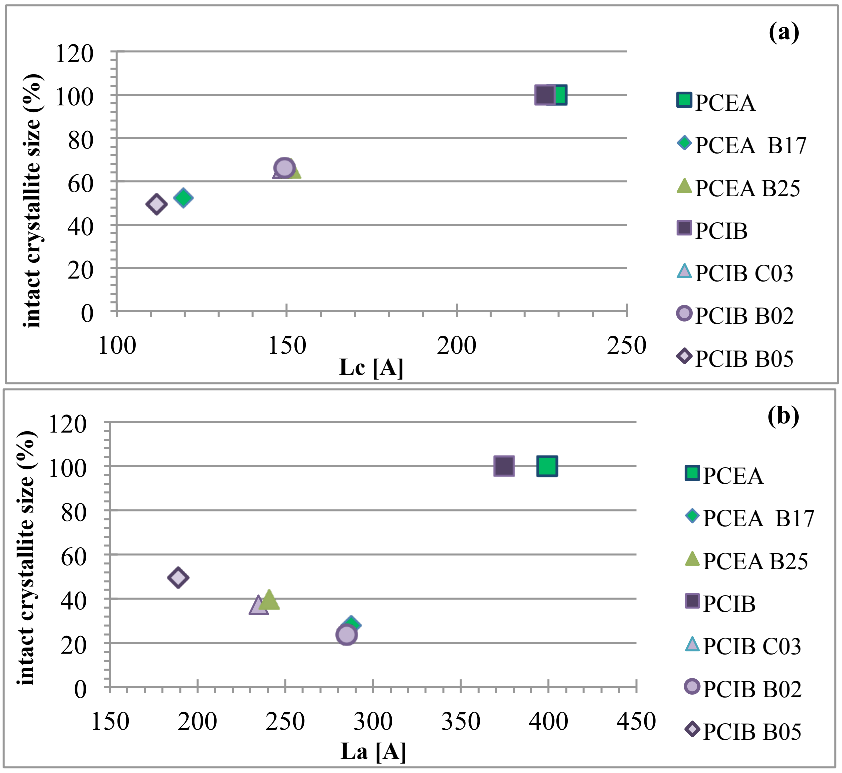

Figure 5.8 Coherence length change due to neutron irradiation; (dimension % kept from the initial value) (a) L_a dimensional change and (b) L_c dimensional change.

For both PCIB and PCEA a decrease in the coherence lengths (Figure 5.8) in the **c-** and **a-**directions of more than 50% was observed with increased dose (note y axes is representing the X_T parameter which was discussed in Chapter 2). These findings are in agreement with Tanabe and Muto [51], who studied the graphite response to neutron and ion irradiation at room temperature up to 1.9 dpa by TEM. Figure 5.8 presents the dimensions of the coherence lengths in both the **c-** (Figure 5.8 (a)) and **a-**directions (Figure 5.8 (b)).

For PCIB, the coherence length decreases abruptly at low temperature and dose (350 °C, 1.5 dpa), with an annealing behaviour evident with increasing temperature (537 °C, 4dpa – note that two points are overlapping on Figure 5.8 (a) but not in Figure 5.8 (b)), and continue decreasing with increasing dose (6.8 dpa) For PCEA the same abrupt decrease was observed, but the “recovery” action could not be observed due to the absence of the PCEA sample irradiated at the intermediated parameters for which the observation of recovery was made for PCIB.

Summary of XRD of irradiated graphites

XRD analysis on the irradiated graphites revealed a change in the lattice parameter due to neutron irradiation. It was shown that PCEA and PCIB have similar response due to irradiation: increasing the lattice parameter in the **c-**direction (swelling), and decreasing the lattice parameter in the **a**-direction (shrinking), in agreement with the literature. Conversely the coherence lengths and hence crystallite sizes in both directions (L_c and L_a) decrease due to irradiation (**Table 5.2**), showing a fragmentation of the initial crystallite size with increasing dose.

Table 5.2 XRD data for different irradiated NG. Unit cell constants and coherence lengths.

Material	DOSE[dpa], Temp[^{0}C]	c-spacing (Å)	L_c (Å)	a-spacing (Å)	$L_a^{(100)}$ (Å)	$L_a^{(110)}$ (Å)
PCEA	NA	$3.370 \pm 3\text{x}10^{-4}$	229.4 ± 56	$2.455 \pm 3\text{x}10^{-3}$	399.2 ± 49	646.6 ± 2
PCEA B25	1.5, 350.9	$3.381 \pm 8\text{x}10^{-4}$	151.2	$2.444 \pm 6\text{x}10^{-3}$	258.5	272.7
PCEA B17	6.8, 670.6	$3.382 \pm 7\text{x}10^{-4}$	119.7	$2.448 \pm 5\text{x}10^{-3}$	308.8	353.4
PCIB	NA	$3.375 \pm 4\text{x}10^{-4}$	225.9 ± 6	$2.454 \pm 3\text{x}10^{-3}$	374.7 ± 14	618.9 ± 38
PCIB C03	1.5, 350.9	$3.378 \pm 7\text{x}10^{-4}$	148.74	$2.441 \pm 6\text{x}10^{-3}$	252.2	263.6
PCIB B02	4.0, 537.5	$3.372 \pm 9\text{x}10^{-4}$	149.3	$2.454 \pm 5\text{x}10^{-3}$	306.1	661.6
PCIB B05	6.8, 656.9	$3.365 \pm 7\text{x}10^{-4}$	111.8	$2.434 \pm 7\text{x}10^{-3}$	203.0	311.8

5.2. Raman spectroscopy

5.2.1. Raman spectra of virgin graphites

I. Raman spectroscopy of PGA

During the Raman analysis, it was noticed that the filler particle sizes (Figure 5.9) were big enough to be analysed separately by Raman spectroscopy (having a beam size ~1μm). As for the XRD measurement, two PGA graphites were analysed in order to make a comparison of their properties.

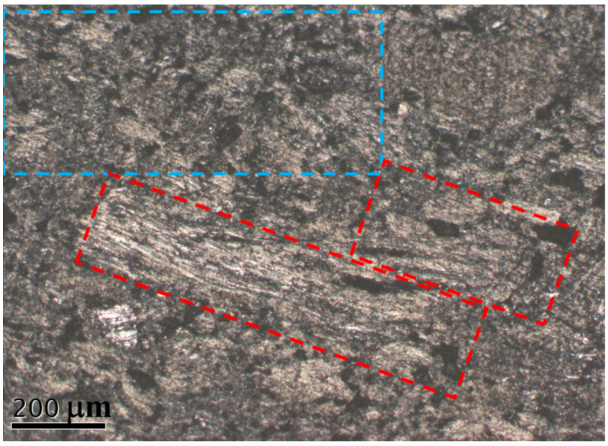

Figure 5.9 Optical micrograph of PGA (Oldbury) representing the two components of the nuclear graphite: binder (blue) and filler (red).

Figure 5.10 presents the Raman spectra of the two very similar (but not equal) phases found in PGA graphite, binder and filler ((a) and (b), respectively). The samples were analysed as received (bulk samples). Figure 5.10 (a*) and (b*) presents the fitting results (for details regarding fitting procedure see chapter 3).

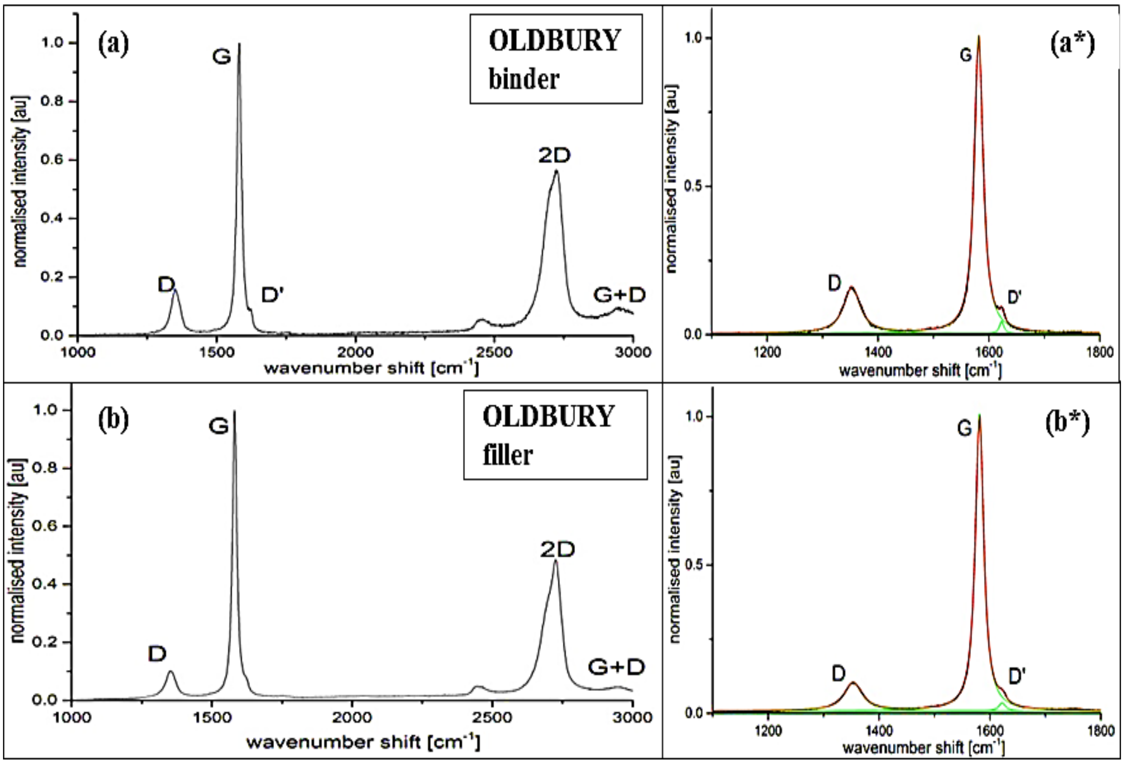

Figure 5.10 Illustrative first-order Raman spectra of Oldbury binder (a)-(a*) and filler (b)-(b*); with * representing the results of the fitting procedure; with: the green line the individual peak fitting, while the red line represents cumulative peak fitting when the fit converged.

The Raman spectra revealed a more prominent D' peak for all the areas established to be binder comparable to the filler (Figure 5.10 (a*) and (b*)). This behaviour could be due to the increase in grain boundaries as a result of the smaller crystallites present in the binder, comparable to the ones in the filler, or due to significant microporosity in the binder.

Table 5.3 Obtained I_D/I_G ratio and FWHM of the G peak for binder (B) and filler (F) of the two PGA graphites analysed (Oldbury and Wylfa).

Material	I_D/I_G	FWHM G [cm^{-1}]
Oldbury F	0.10 ± 0.03	19.2 ± 1.6
Oldbury B	0.19 ± 0.07	21.0 ± 1.5
Wylfa F	0.12 ± 0.07	19.7 ± 1.8
Wylfa B	**0.22** ± 0.07	23.1 ± 2.6

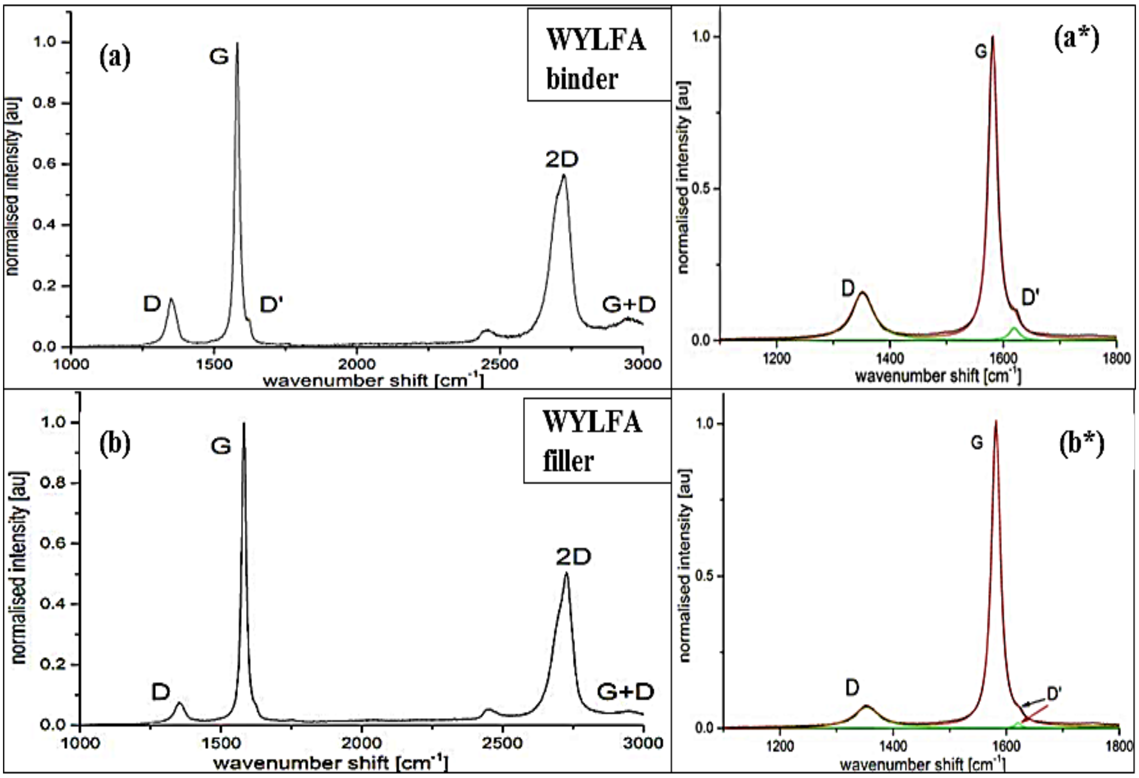

Figure 5.11 Representative first-order Raman spectra of Wylfa binder (a)-(a*) and filler (b)-(b*); with * representing the results of the fitting procedure; with: the green line the individual peak fitting, while the red line represents cumulative peak fitting when the fit converged.

Typical Raman spectra of binder and filler for PGA Wylfa graphite are shown in Figure 5.11 (a) and (b). Compared to Oldbury, in Wylfa D' exhibits a lower intensity relative to the G peak, but the overall intensity of the D peak is higher than in the Oldbury one, as can be seen in **Table 5.3.** The values quoted in the table were calculated by averaging values obtained by fitting over 40 spectra per sample.

Summary of Raman spectroscopy in PGA graphites

Raman Spectroscopy results for the two PGA graphites both show a higher I_D/I_G ratios for binder as opposed to filler. The results are also in agreement with the XRD findings, showing smaller size crystallites for Wylfa than Oldbury (**Table 5.1**), translated in Raman spectra as more grain boundaries and hence bigger intensity to the D peak.

II. Raman spectroscopy of different (filler-F) grain sized graphites

Figure 5.12 shows a typical Raman spectra from three types of graphite, each with a different filler size: NBG-18 ~ 300μm, IG-110 with ~ 20μm [31], and Gilsocarbon (GILSO) a big grain size, in the range of 0.3-1.3mm [156]. The extracted I_D/I_G, FWHM of the G peak, and the G position values of all analysed graphites were determined by averaging over 50 spectra / sample. **Table 5.4** shows their values, compared to a more perfect (even though anisotropic) graphite- HOPG. Up to now, it was thought that the D peak intensity is due to defects, which are present in the sample, and to the crystallite

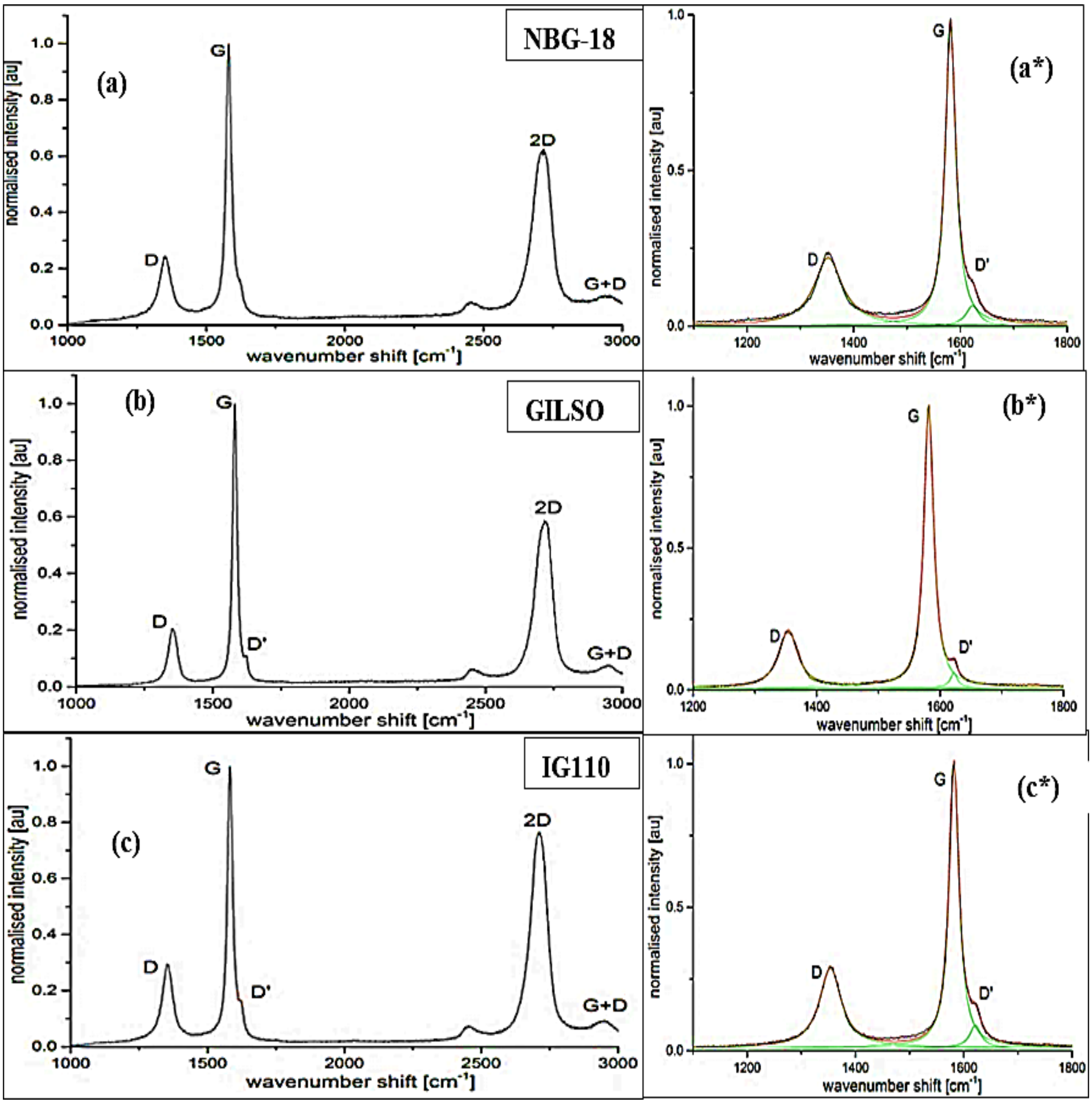

Figure 5.12 Illustrative first-order Raman spectra of NBG 18 (a)-(a*), GILSO (b)-(b*) and IG110 (c)-(c*); with * representing the results of the fitting procedure; with: the green line the individual peak fitting, while the red line represents cumulative peak fitting when the fit converged.

boundaries. The results for these three graphites, with different F grain sizes, show that the I_D/I_G ratio cannot be taken in consideration as a parameter when making a classification based on the F grain size of the graphite, but more considered as a parameter reflecting the disorder in the lattice, which comes from different types of defects (e.g. point defects or dislocations). If a classification based on the disorder in graphite is to be made, the FWHM of the G peak could be considered as the more significant parameter: the most perfect graphite would be HOPG, and the least perfect would be NBG-18.

III. Raman spectroscopy of new developed graphites (PCEA- PCIB)

In Figure 5.13 the Raman spectra of two newly developed graphites is shown. As mentioned in Chapter 2, these graphites are considered for the new generation of nuclear graphites. Because of this, any new information is a useful addition to the data library needed to assess and to improve their future behaviour when heavily irradiated at higher temperatures.

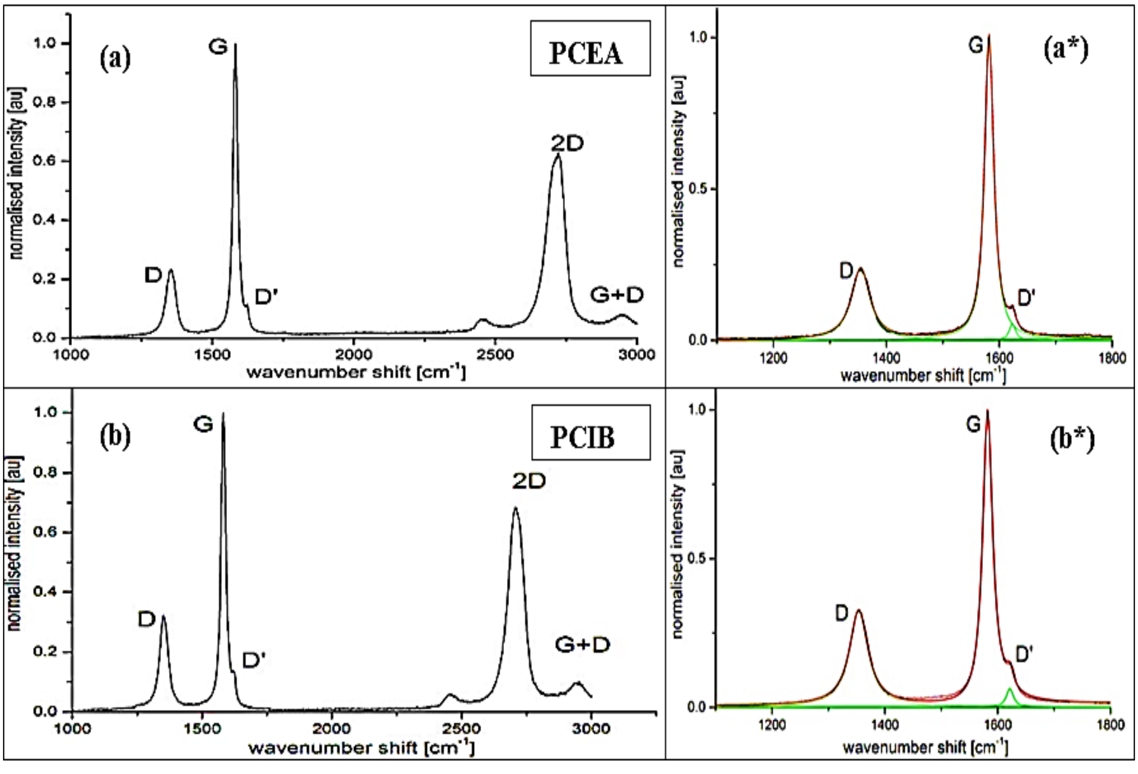

Figure 5.13 Representative first-order Raman spectra of PCEA (a)-(a*) and PCIB (b)-(b*); with * representing the results of the fitting procedure; with: the green line the individual peak fitting, while the red line represents cumulative peak fitting when the fit converged.

PCEA has a medium F grain size (<1mm) while PCIB has a smaller F grain size (~360µm). The analysis revealed a higher tendency for PCIB to have an increased intensity of the D peak, which makes the overall I_D/I_G ratio higher for PCIB than PCEA. However, the FWHM of the G peak is similar, which means that both of them are equally graphitised, but not equally populated by defects.

Summary of Raman spectroscopy of virgin nuclear graphites

The results have shown that the I_D/I_G ratio and the FWHM of the G peak can be useful parameters in the classification of nuclear graphites. Next, a comparison among all virgin graphites analysed will be made.

In Figure 5.14 the FWHM of the G peak is presented versus the I_D/I_G ratio, showing a positive linear correlation between FWHM of the G peak and I_D/I_G ratio for all area in the virgin graphites studied. However the slopes are slightly different for different graphites, which can be due to differences in the microstructure of the graphites by having a big influence in the spreading of the data. Hence even if a linear fit can be observed, the variation of I_D/I_G inside a samples makes the fitting r^2 have different values and also suggesting a non linear fitting, e.g. in Oldbury PGA case, has a very poor fitting r^2 even though Wylfa, the same grade graphite (but manufactured elsewhere) has more acceptable r^2. Still, none of the graphites have the I_D/I_G ratio bigger than 0.4 and/or the FWHM of the G peak outside the range of 14.5 – 29 cm^{-1}. For all Raman spectroscopy values the points were averaged over all the values measured/ sample, showed in Figure 5.14.

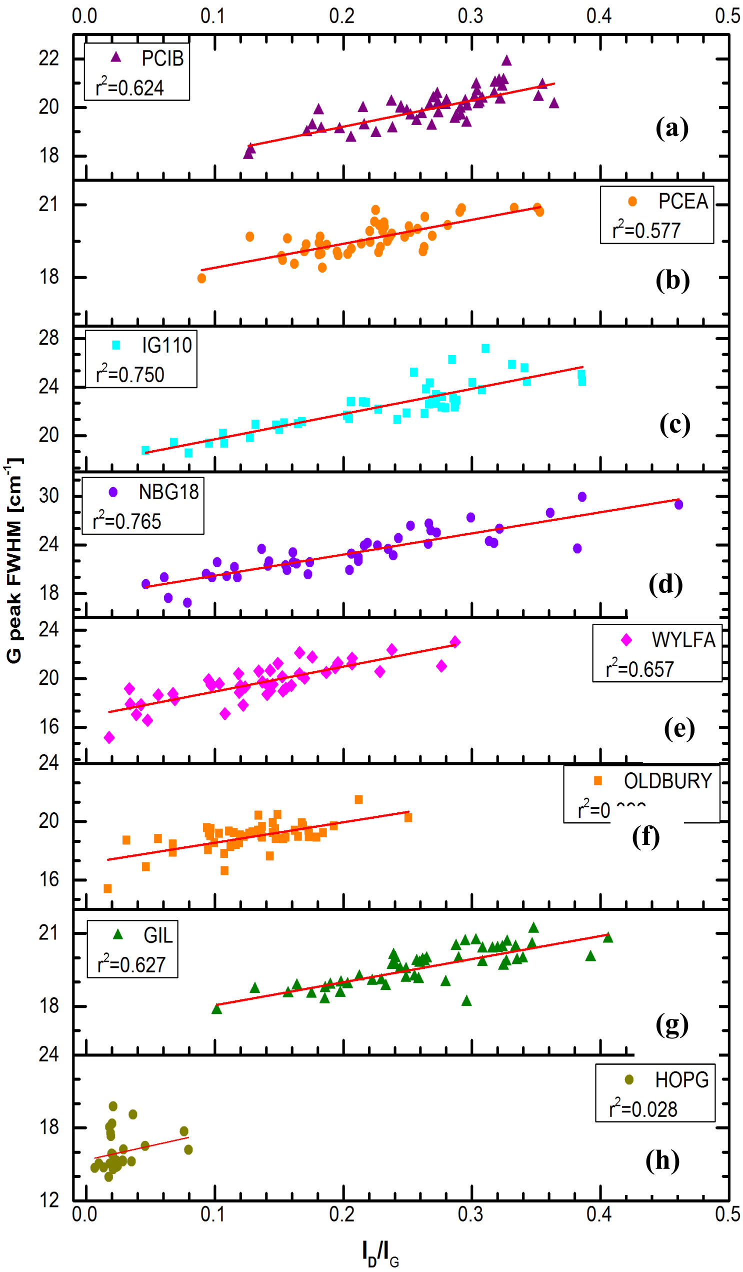

Figure 5.14 Width of the G peak versus the intensity ratio I_D/I_G in a linear scale for different types of virgin nuclear graphites.

The present results can be discussed in the context of previous work (Nikiel [117], Tanabe [73] or Niwase [50,52,76,152]) on the characterization of the response of graphite to different types of irradiation. This is done in order to find a correlation between the graphitization stage, the disorder in the lattice, and the coherence length in the **a**-direction, as it has been demonstrated that there is a close correlation exists between the I_D/I_G ratio and the length of the L_a value, or the abundance of crystallite edges. Figure 5.15 (a) shows the I_D/I_G ratio versus the L_a value found by XRD, while Figure 5.15 (b) shows the FWHM of the G peak versus the same L_a value found by XRD. In Figure 5.15 (c) the G peak position versus the L_a value is plotted.

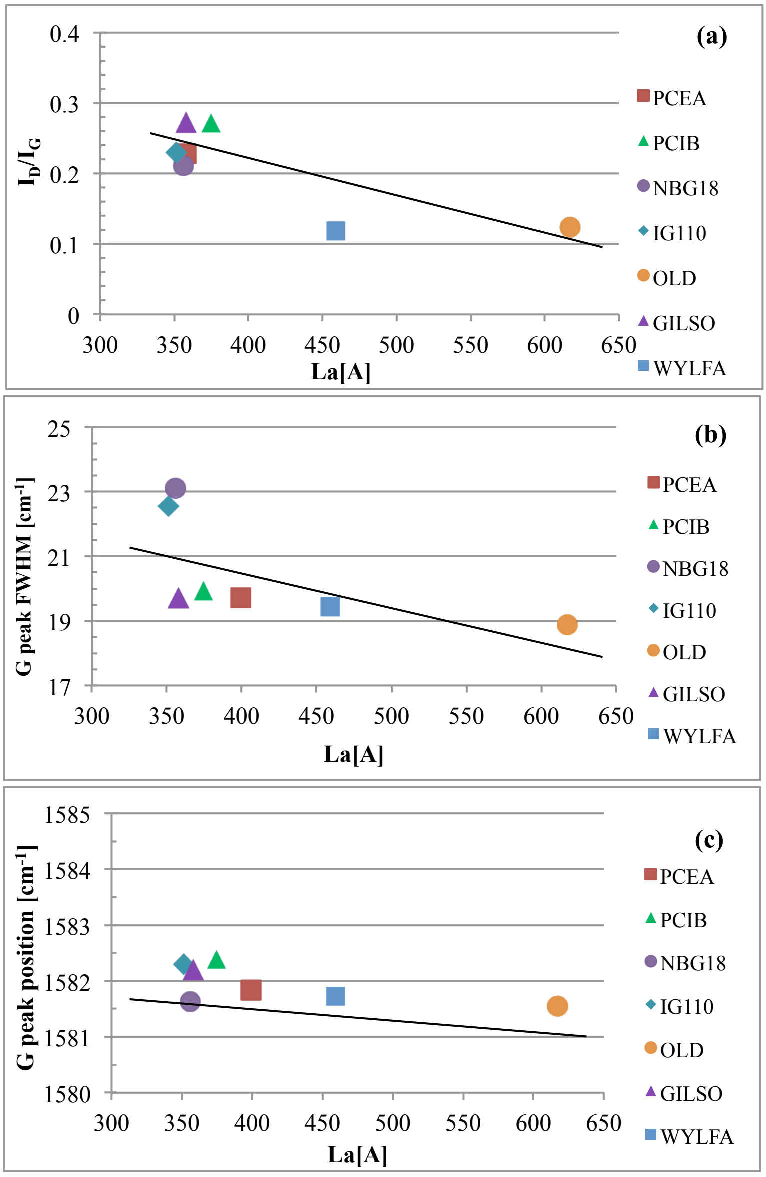

Figure 5.15 Plot of virgin graphites analysed of: (a) Raman intensity ratio I_D/I_G versus the coherence length (L_a) from X-ray data; (b) Width of the G peak versus the L_a from X-ray data; (c) G peak position versus the L_a value from X-ray data

Comparing all results in Figure 5.15, one notices that the I_D/I_G versus L_a shows a good correlation, due to the influence of edge boundaries of the D peak, while is no correlation between the position of the G peak versus the L_a from XRD, as the G peak contains information more from the internal structure of the crystallites not from the boundaries; a slight correlation can be observed between the FWHM of the G peak and the L_a. The linear fit of the graphites I_D/I_G ratio, or the FWHM of the G peak versus the L_a value are in agreement with Nikiel and Jagodzinski [117].

Considering the observed importance in establishing the graphitization/order observed in previous section, and also the correlation observed for the FWHM and the I_D/I_G ratio with the coherence length, it was decided that this parameters (I_D/I_G and FWHM versus the L_a), will be followed further one in assessing the damage found in damaged graphite (neutron irradiated graphite)

Table 5.4 presents an overview of all parameters obtained by Raman spectroscopy on virgin graphites in this thesis. All values are calculated by averaging data from ~50 spectra per sample.

Table 5.4 Raman spectroscopy data for various virgin graphites.

Material	I_D/I_G	FWHM G [cm^{-1}]	G peak position [cm^{-1}]	D peak position [cm^{-1}]
HOPG	0.03 ± 0.02	15.2 ± 1.0	1581.9 ± 0.6	1350.8 ± 16.2
Oldbury	0.12 ± 0.05	18.9 ± 1.0	1581.6 ± 0.4	1353.2 ± 0.8
Wylfa	0.14 ± 0.06	19.6 ± 1.6	1581.8 ± 0.5	1353.1 ± 1.3
PCEA	0.22 ± 0.05	19.6 ± 1.0	1581.8 ± 0.4	1354.3 ± 0.5
PCIB	0.27 ± 0.06	19.9 ± 1.0	1582.4 ± 0.3	1354.2 ± 0.4
GILSO	0.26 ± 0.06	19.5 ± 1.0	1582.1 ± 0.8	1353.7 ± 0.8
NBG-18	0.21 ± 0.1	22.9 ± 3.0	1581.6 ± 0.44	1352.7 ± 1.1
IG110	0.23 ± 0.08	22.5 ± 2.0	1582.3 ± 0.6	1353.7 ± 1.0

5.2.2. Raman spectra of neutron irradiated graphites

Figure 5.16 shows a collection of Raman spectra representative for the irradiated graphites from PCIB set of samples, compared to the virgin version of the same graphite grade. In the same figure, in the right hand side the fitted spectra are shown for each plot (denoted by *)

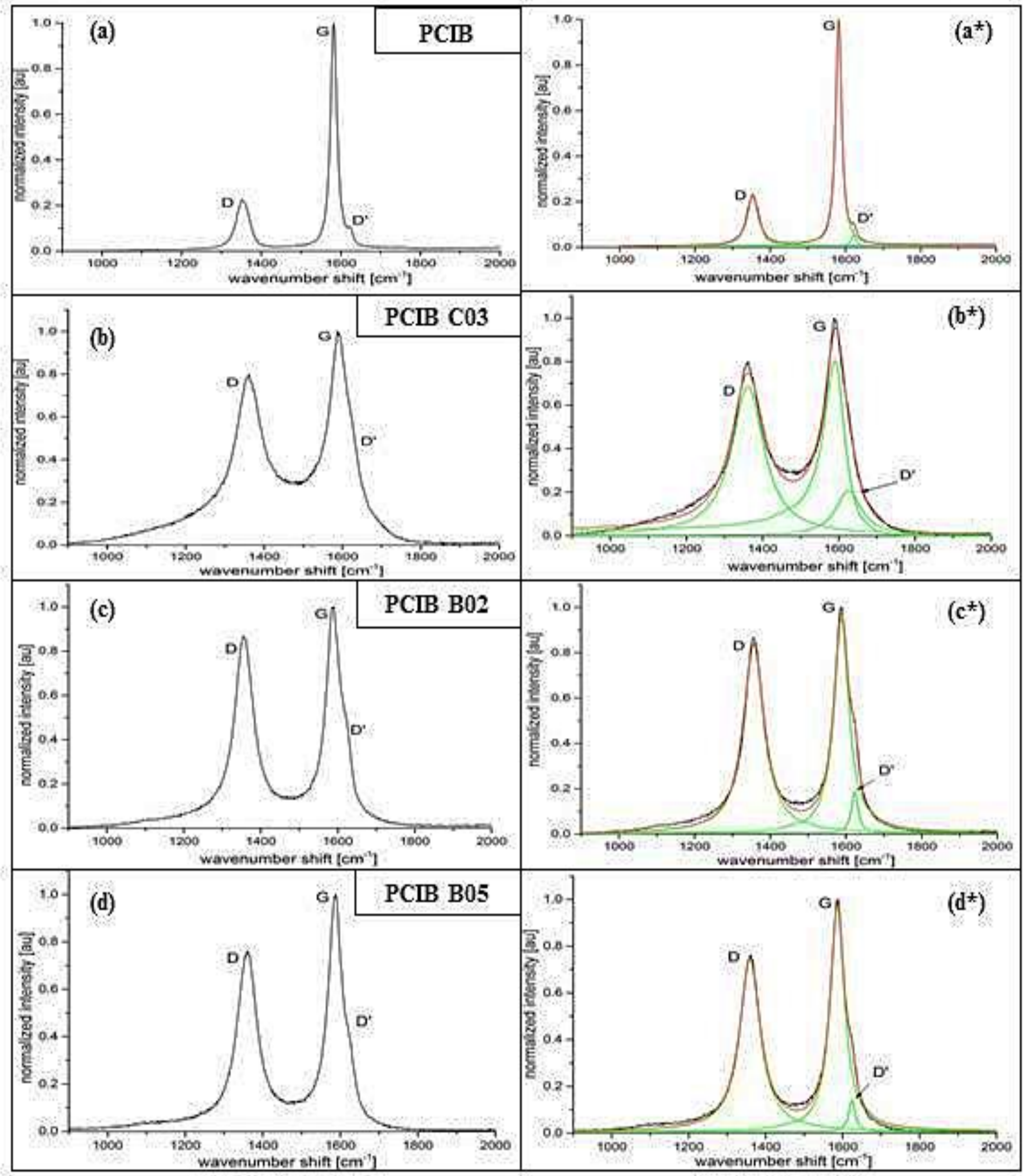

Figure 5.16 Representative first-order Raman spectra of irradiate PCIB: virgin PCIB (a)-(a*), C03 (b)-(b*), B02 (c)-(c*) and B05 (d)-(d*); with: the green line the individual peak fitting, while the red line represents cumulative peak fitting when the fit converged.

For all PCIB samples analysed, the fitting procedure presented an almost perfect fit with and average $R^2 \sim 0.99$ (+/-0.002). It was observed that on irradiation, the position of the G peak shifted towards higher wavenumber, showing a tendency of the irradiated graphites to transform from graphite to nano- crystalline graphite. Together with the position of the G peak change, the spectra at lower irradiation dose (and temperature) corresponding to C03, resembles the Raman Spectra of a disordered material such as carbon black (see Chapter 3). With increasing dose (and temperature), the normal appearance of the graphite spectra appears to recover, probably due to the temperature annealing of some in-plane defects as suggested by Tanabe *et al*. [71], these defects being easy to anneal out.

In Figure 5.17 a linear fit of all the sample areas in the PCIB irradiated graphites is shown, in comparison with the virgin version. It can be noticed, that even though C03 has an almost negative slope, it is still linear, and as predicted by Niwase [152] (who worked on He ion irradiation graphite) even when very amorphous, the plot of FWHM of the G peak versus the I_D/I_G, maintains its linear relation. When compared to the virgin graphite, all irradiated graphite had both the FWHM of the G peak, and the I_D/I_G ratios increased. This is compatible with published work [50,52,152], even though the values found were obtained using electron or ion irradiation, or neutron irradiation with lower irradiation parameters (e.g. dose, temperature) than the present samples.

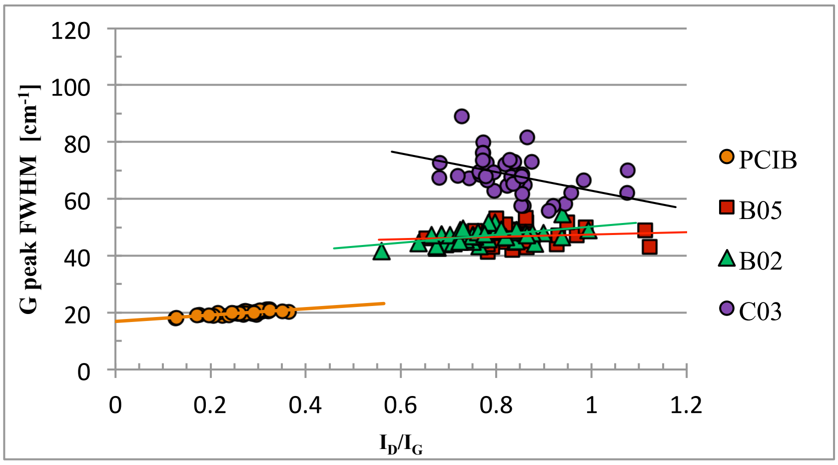

Figure 5.17 Width of the G peak versus the intensity ratio I_D/I_G for different samples of irradiate PCIB with their linear fitting.

For the other set of irradiated samples (PCEA), Figure 5.18 shows a collection of characteristic Raman spectra and fits.

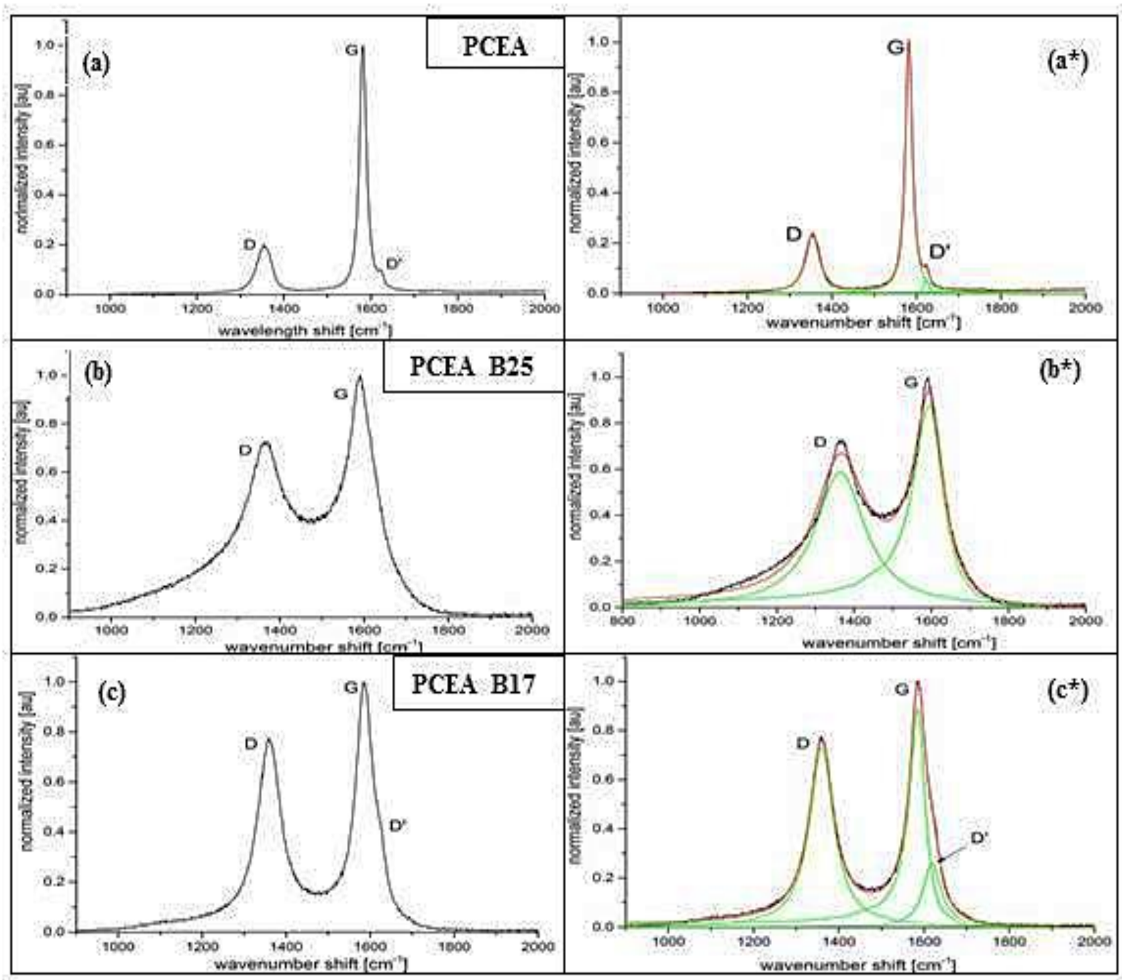

Figure 5.18 Representative first-order Raman spectra of irradiate PCEA: B25 (a)-(a*) and B17 (b)-(b*); with * representing the results of the fitting procedure. (with: the green line the individual peak fitting, while the red line represents cumulative peak fitting when the fit converged)

For all PCEA samples analysed, the fitting procedure presented an almost perfect fit with and average $R^2 \sim 0.99$ (+/-0.002). However for PCEA B25 the fitting procedure, the omission of the D’ peak was needed, as its presence made impossible the convergence of the fit. This situation might be due to the fact that, the D’ peak position might have been shadowed by the G peak, which moved towards higher wave number due to change in perfection of the lattice and in symmetry of the crystal. As in the PCIB sample case, when irradiated with low dose at low temperature PCEA B25 (1.5 dpa, ~350 °C) shows a Raman spectra with a more disordered appearance compared to the sample irradiated with higher dose at higher temperature (B17 – 6.8dpa, ~670 °C). The resulting averaged values are presented in Table 5.5**.**

In the case of the irradiated PCEA samples, the FWHM of the G peak versus the I_D/I_G ratio variation (Figure 5.19), shows a higher increase of the FWHM and of the I_D/I_G ratio as compared to the PCIB set (Figure 5.17). It might be concluded from this that PCEA is more affected by neutron irradiation, especially for the lower irradiation parameters.

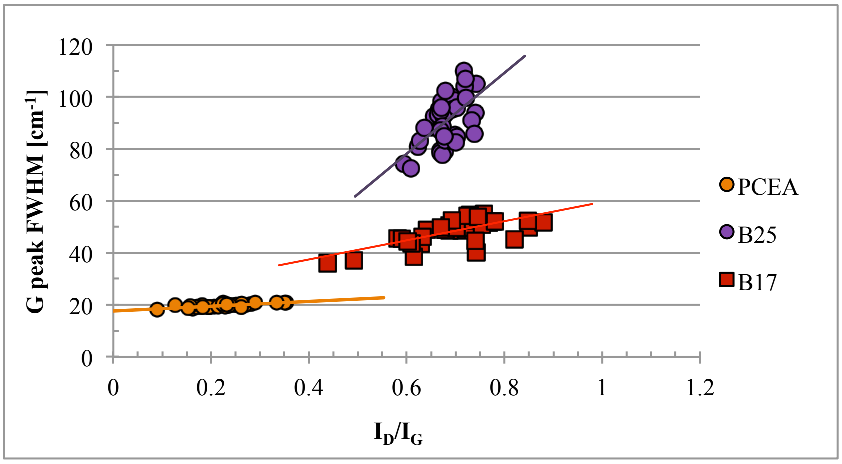

Figure 5.19 Width of the G peak versus the intensity ratio I_D/I_G for different samples of irradiate PCEA with their linear fitting.

Summary of Raman spectra of neutron irradiated graphites

For virgin graphites, it was established in previous section, that a linear correlation exists between the FWHM (a) or the I_D/I_G ratio (b).

Figure 5.20 shows the plot between the L_a value found by XRD, and the G peak FWHM (a) or the I_D/I_G ratio (b), containing the value of the L_a next to the obtained point on the plot, for the eye guidance.

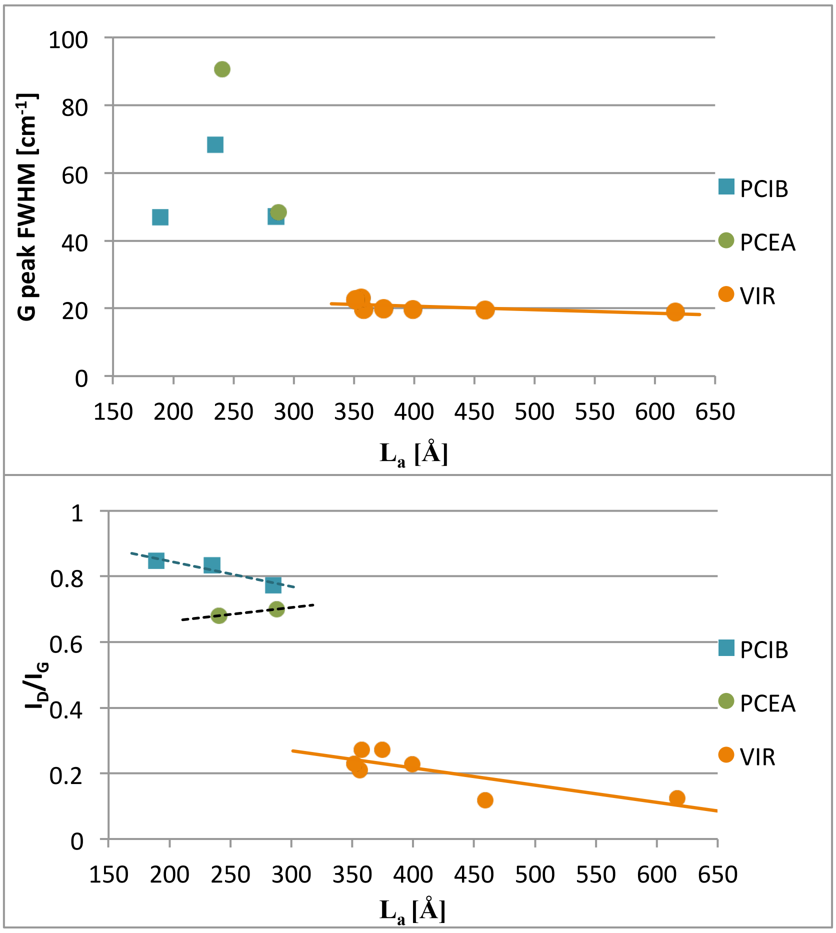

Figure 5.20 Irradiated graphites analyses: (a) Raman intensity ration I_D/I_G versus the coherence lengths (L_a) from X-ray data; (b) FWHM of the G peak versus the L_a from X-ray data. All sets contain the afferent linear fitting

The change in the slope for I_D/I_G fitting cases is obvious compared to the virgin graphite, and a correlation as was proposed by Tuinstra and Koenig for Raman versus XRD in obtaining the L_a value it was proven not to work for all cases, as it has been discussed in the literature [117]. There appears to be little correlation between FWHM of the G peak and L_a.

It was observed that in the case of I_D/I_G plot, the fitting have the same trend as virgin graphite. However, the fact that irradiated PCIB and PCEA have different trends suggests that each graphite grade behaves differently but, in order to confirm this, a more consistent analysis of different irradiation data has to be obtained.

Because the experiments were conducted with different types of irradiation parameters, these results could be used as an initial screening to different responses to neutron irradiation of the future graphite types.

Figure 5.21 (a) shows the variation of the intensity ratio I_D/I_G measured by Raman spectroscopy of PCIB and PCEA irradiated graphites with the irradiation dose. Figure 5.21 (b) illustrates the change of the G peak width for the same samples with the irradiation dose. It has to be noted that in the second plot, even though the dotted lines are to guide the eye, major increase of the FWHM of the G peak, at lower irradiation temperature, agrees with literature data for doses between 0.1–1 dpa at irradiation temperature lower than 200 °C [50].

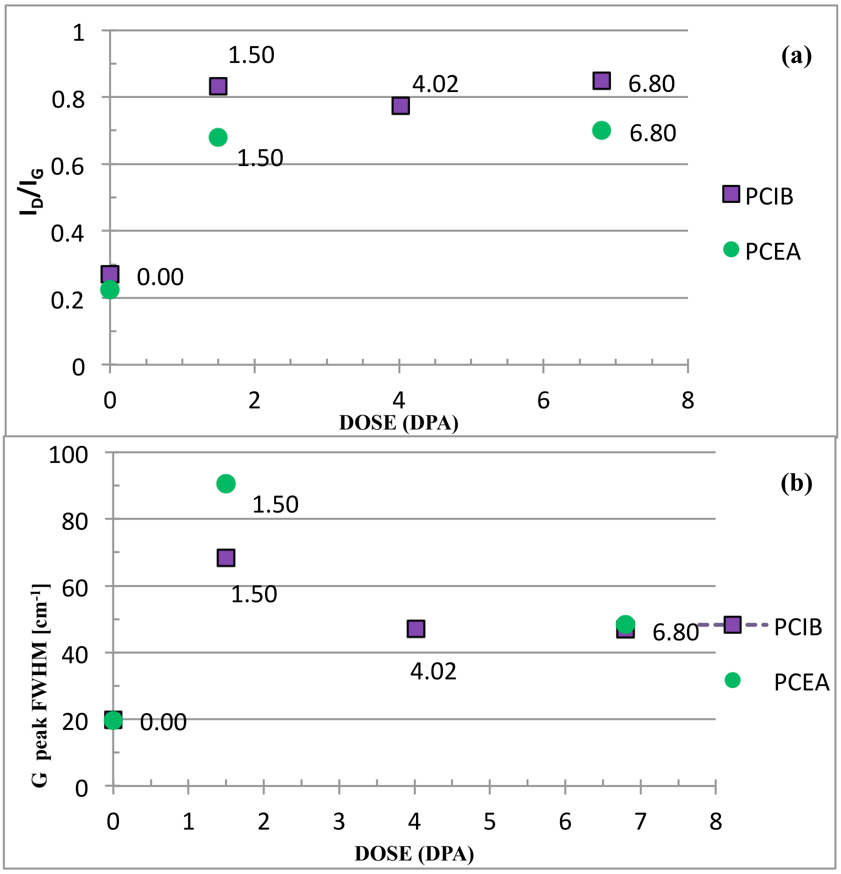

Figure 5.21 (a) Intensity ratio of I_D/I_G and (b) FWHM of the G peak versus de irradiation dose.

After all these, it is expected PCEA and PCIB to behave differently when irradiated, even though they have just a slight difference in structure. This was the prediction made also by Hall and Bradford [157,158] who suggested that the filler size particle has a high influence on the change in the physical properties of nuclear graphite when irradiated. The same effect is due, as studied by M. Morgan in 1960 [159], to the changes in mechanical properties because of the frequency of some turbostratic structures found in binder.

Table 5.5. Raman spectroscopy data for various virgin graphites, irradiated and non-irradiated.

Material	DOSE[dpa][·], Temp[^{0}C]	I_D/I_G	FWHM G [cm^{-1}]	G peak position [cm^{-1}]	D peak position [cm^{-1}]
PCEA	**NA**	0.22 ± 0.1	19.7 ± 1	1581.8 ± 1	1354.3 ± 1
PCEA B25	**1.52, 350.9**	0.68 ± 0.1	90.6 ± 9	1593.1 ± 2	1364.8 ± 2
PCEA B17	**6.8, 670.7**	0.70 ± 0.1	48.5 ± 5	1587.2 ± 1	1361.6 ± 1
PCIB	**NA**	0.27 ± 0.1	19.9 ± 1	1582.4 ± 1	1354.2 ± 1
PCIB C03	**1.52, 350.9**	0.83 ± 0.1	68.3 ± 7	1590.0 ± 2	1362.3 ± 3
PCIB B02	**4.04, 537.5**	0.78 ± 0.1	46.9 ± 3	1587.3 ± 1	1358.8 ± 2
PCIB B05	**6.8, 656.9**	0.85 ± 0.1	46.8 ± 3	1586.5 ± 2	1358.4 ± 2

Table 5.5 is a summary of all the Raman findings for the PCIB and PCEA irradiated samples. All the quoted values were obtained by averaging the data of more than 40 spectra per sample, with the fit having 0.98(+/-0.002) $< R^2 <$ 0.99(+/-0.003).

[·] down the column the dose is highlighted in red

5.3. Scanning electron microscopy

Figure 5.22 (a) showing the analysis of the Scanning Electron Microscope (SEM) images for virgin PCIB, the irradiated PCIB B05, irradiated with 6.8 dpa Figure 5.22 (b) and PCIB C03 Figure 5.22 (c), which received a dose of 1.5 dpa, revealed significant changes in morphology of the sample’s surfaces. The pores were evident in the SEM images of B05 and C03, and were of μm order, linked to each other by random shape, which made impossible the pore measurement. However their presence indicated that further work is needed to identify their nature, size and density, and more precise to

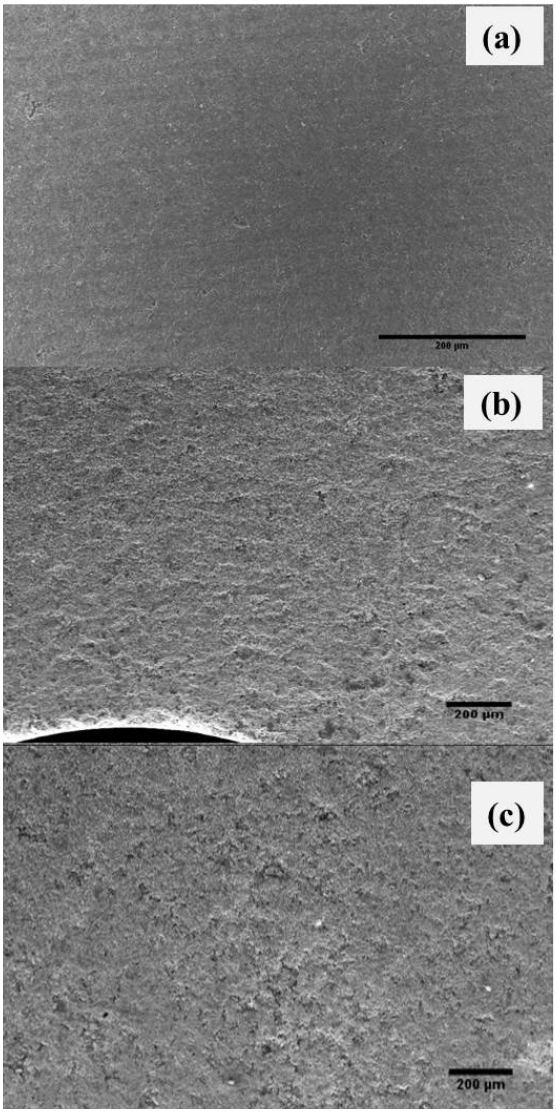

Figure 5.22 Collection of image showing SEM image of : (a) virgin PCIB, (b)irradiated PCIB B05 and (c) irradiated PCIB C03

see if the surface pores are due to irradiation or to the cutting procedure used when preparing the samples.

SEM images of virgin PCEA Figure 5.23 (a) revealed a surface with higher degree of porosity, in contrast with virgin PCIB Figure 5.22 (a). The measurements were done on four SEM images providing a surface area of 9.4 mm^2 each. It was calculated that the slit shaped pores had an area density of ~1 pore /mm^2 with area ranging from ~400 μm^2 to ~18 800 μm^2, with an average pore area of ~2500 μm^2 .The pores presented no preferred orientation being random in dimension and shape.

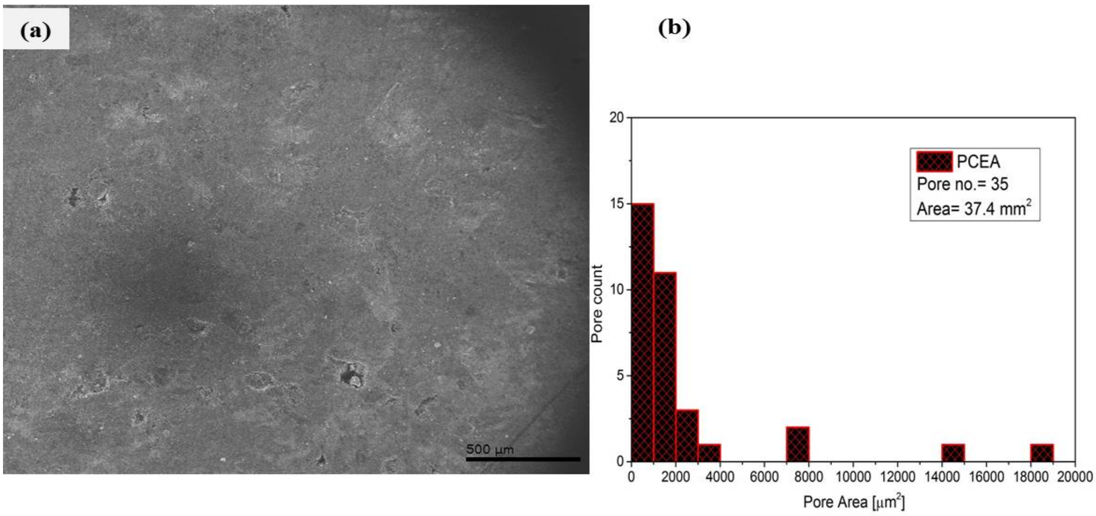

Figure 5.23 (a)SEM image of a sliced virgin PCEA; (b) histogram of the areas of the measured pores

Figure 5.24 and **Error! Reference source not found.** represents SEM images of irradiated PCEA B25 and PCEA B17 respectively. The measurements were done on SEM images providing a relative surface area of ~5.6 mm^2 each.

Based on a set of SEM images similar to Figure 5.24 (a) it was calculated that for the PCEA B25, the dimension of the pores had an density of ~9.5 pores/mm^2 with pore areas in the range of ~400 μm^2 to ~8700 μm^2 (with an average pore are of ~2000 μm^2).

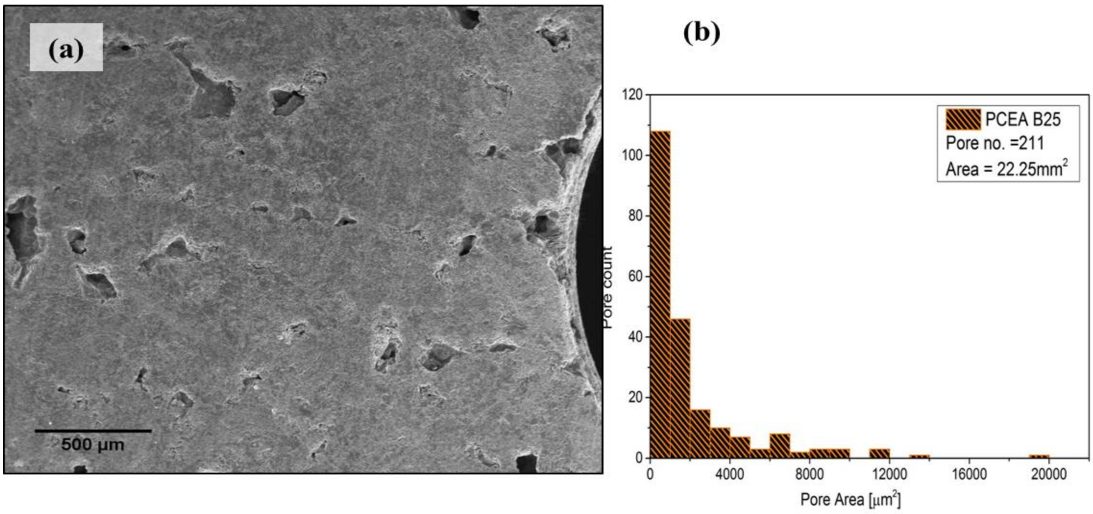

Figure 5.24 (a)Typical SEM image of the irradiated PCEA B25; (b) histograms of the areas of of the measured pore;

From PCEA B17 SEM images, similar to the one presented in **Error! Reference source not found.** (a), it was calculated that the dimension of the pores had an density of ~10 pores/mm^2 with pore areas in the range of ~400μm^2 to ~8700 μm^2 (with an average pore are of ~3200 μm^2).,

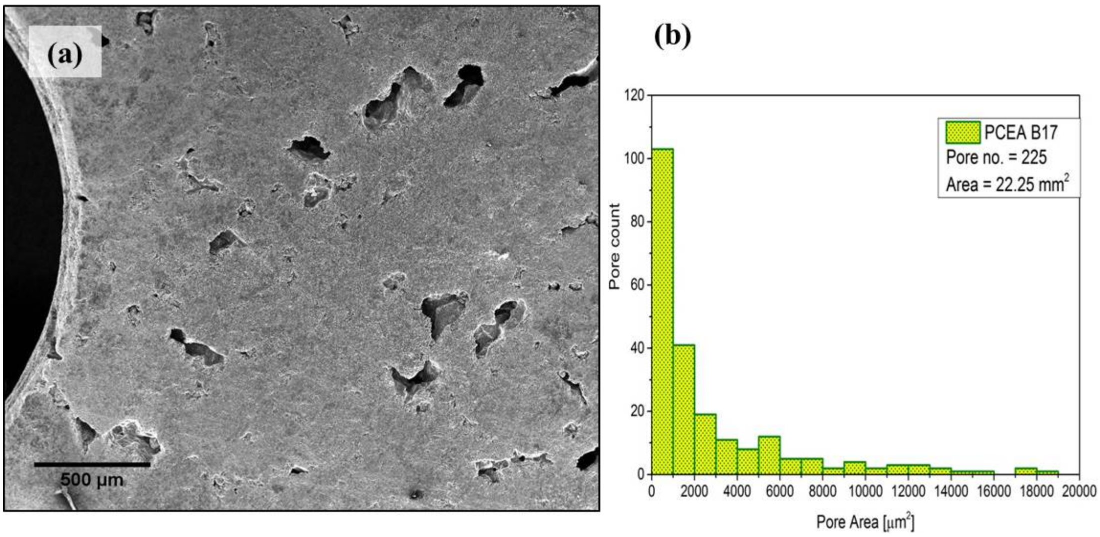

Figure 5.25 (a) SEM images of the irradiated PCEA B17; (b) histogram of the areas of of the measured pore;

Summary of SEM analysis

The PCEA set of samples revealed a higher surface porosity with the tendency of growing in pore population with irradiation. The density of pores increased from ~1 pores/mm^2 (for the virgin sample), to ~9 pores /mm^2 (for B25) and ~10 pores/mm^2 (for B17). The increase in density of surface pores came with the dimensional change of the pores as well reaching from a pore area of an average of ~2500 μm^2 to ~3200 μm^2, in the case of B17, while in the case of B25 the pores increased their number but decreased their average area dimension

All nuclear graphites showed increased slit shaped porosity following irradiation, this being more marked for PCEA as compared to PCIB. It has to be noted that the SEM analysis is a 2D analysis of the surface pores, revealing more a qualitative change in the surface porosity and not taking in consideration the internal structure or the internal dimension of pores and their number density (hidden pores). Also due to the resolution of the SEM equipment, the possible presence of the surface nano-pores was not taken in consideration.

5.4. Transmission electron microscopy

Past analyses on irradiated nuclear graphites used mostly electron, ion irradiation or neutron irradiation at less than 1 dpa, and most of them used as surrogate sample, HOPG, instead of real nuclear graphite. In the next sections, different techniques of electron microscopy were used, in order to crosscheck the findings from the other characterization techniques used in this thesis, and also add more information to the database of neutron irradiation in nuclear graphite.

5.4.1. HRTEM analysis of nuclear graphites

High-resolution images were used in order to obtain an immediate qualitative impression of the existing crystallinity within a sample. All images presented are representative of all the structures observed. All the data was acquired and analysed according to the procedures described in previously. The choice of the area to be analysed was subject to the microscopist decision and was most of the time influenced by the difficulty to find well-oriented areas.

The collection of images shown in Figure 5.26 displays the structural appearance of the PCEA graphite sets which covers the range of irradiation from virgin **PCEA** (Figure 5.26 (a)), to irradiated **PCEA B25** with 1.5 dpa at 350 °C (Figure 5.26 (b)), and **PCEA B17** which received 6.8 dpa at ~670 °C (Figure 5.26 (c)). The average over each set of data within the standard deviation of each other was PCEA: 3.40 ± 0.02 Å, PCEA B25: 3.44 ± 0.05 Å and PCEA B17: 3.36 ± 0.03 Å.

The same procedure described before (section 3.4.2.5), of using FFT filtering followed by intensity profiles measurements, was applied for the PCIB set of samples. The collection of images shown in Figure 5.27 displays the structural appearance of the PCIB graphite sets: virgin **PCIB** (Figure 5.27 (a), (a*)), irradiated **PCIB C03** with 1.5 dpa at ~350 °C (Figure 5.27 (b),(b*)), P**CIB B02** which received 4 dpa at ~537,5 °C (Figure 5.27 (c),(c*)), and **PCIB B05** which received 6.8 dpa at ~659.9 °C (Figure 5.27 (d),(d*)). Compared to PCEA set, in PCIB set, all samples analysed present similar values of the d-spacing in the (002) direction with the following averages: PCIB: 3.39 ± .04 Å; PCIB C03: 3.94 ± 0.03 Å, PCIB B02: 3.37 ± 0.01 and PCIB B05: 3.39 ± 0.02 Å.

For both PCEA and PCIB, the electron diffraction patterns provided values in agreement with the XRD derived values for the lattice parameter **c.**

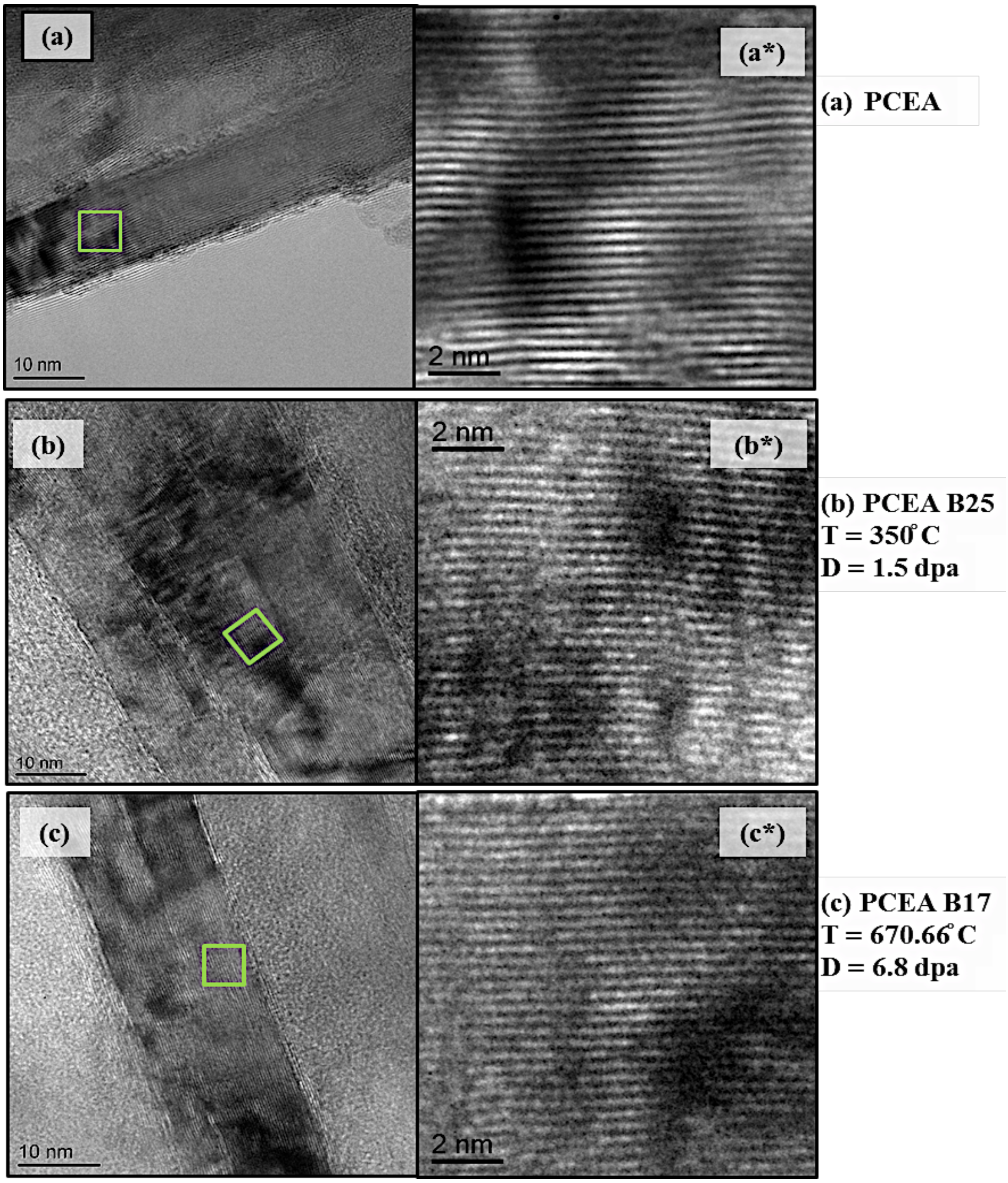

Figure 5.26 High resolution images of PCEA series along with the Fourier filtered images (denoted with * for each image and representing the green square from each image) showing preservation of long range order over neutreon irradiation at different parameters.

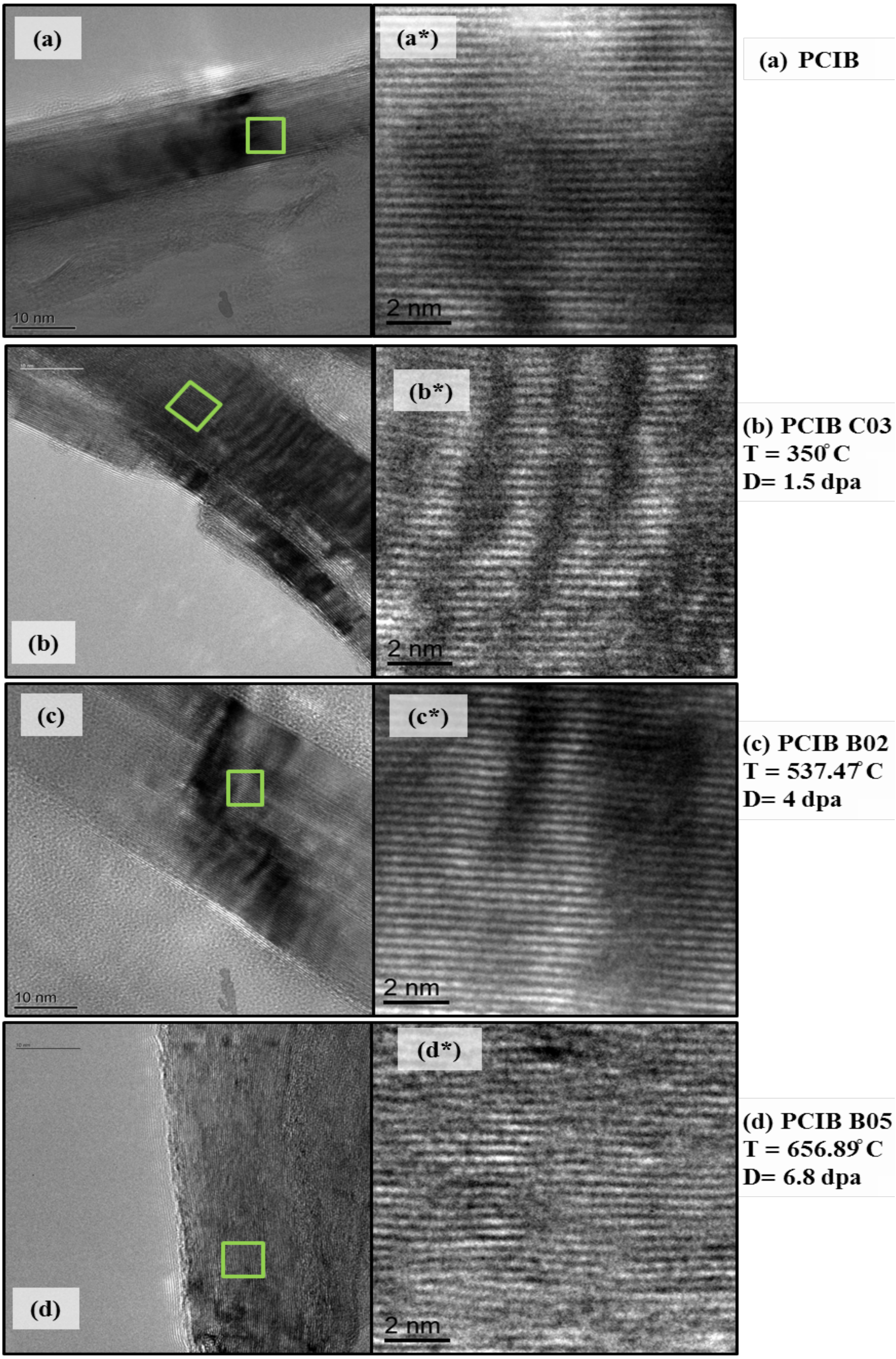

Figure 5.27 High resolution images of PCIB series(a) - (d), along with the Fourier filtered images(a*) - (d*) showing preservation of long range order over neutron irradiation at different parameters.

Even though the clarity of the images from the irradiated samples is less than for the virgin graphite, the images show little change with the irradiation conditions, and the clarity change could be due to the poor resolution of the microscope at 80 keV and/or to the difficulty to find suitable edges of crystallites showing the lattice fringes over the holes in the carbon film. However the change in contrast of the irradiated samples could be due also to the accumulations of point defects, which would have disorder the lattice.

5.4.2. Data subtracted from bright field electron diffraction

(100) ring from the SAED was used in order to find the **a** lattice parameter, while for the **c** direction (002) was used. The SAED presented for each BF TEM image in Figure 5.28 are typical appearances for all samples within the PCEA graphite series analysed.

The group of images, along with their diffraction patterns, shown in Figure 5.28, displays the structural appearance of the PCEA sets of graphites analysed: virgin **PCEA** (Figure 5.28 (a)), irradiated **PCEA B17** which received 6.8 dpa at ~670 °C (Figure 5.28 (b)), and **PCEA B25** with 1.5 dpa at ~350 °C (Figure 5.28 (c)).

Each set of data provided the following results for the **a**-direction: PCEA 2.34 ± 0.04 Å, PCEA B25 2.34 ± 0.06 Å, and PCEA B17 2.35 ± 0.06 Å. All the value are below the theoretical value of 2.46 Å and bellow the value obtained by XRD, which might be due to the basal plane defects accumulations, within the crystallites. For the **c**-direction, the average data gives: for PCEA ≈ 3.34 ± 0.07 Å, for PCEA B25 ≈3.34 ± 0.09 Å and for PCEA B17 ≈ 3.35 ± 0.06 Å, values in agreement with the XRD data and theoretical value.

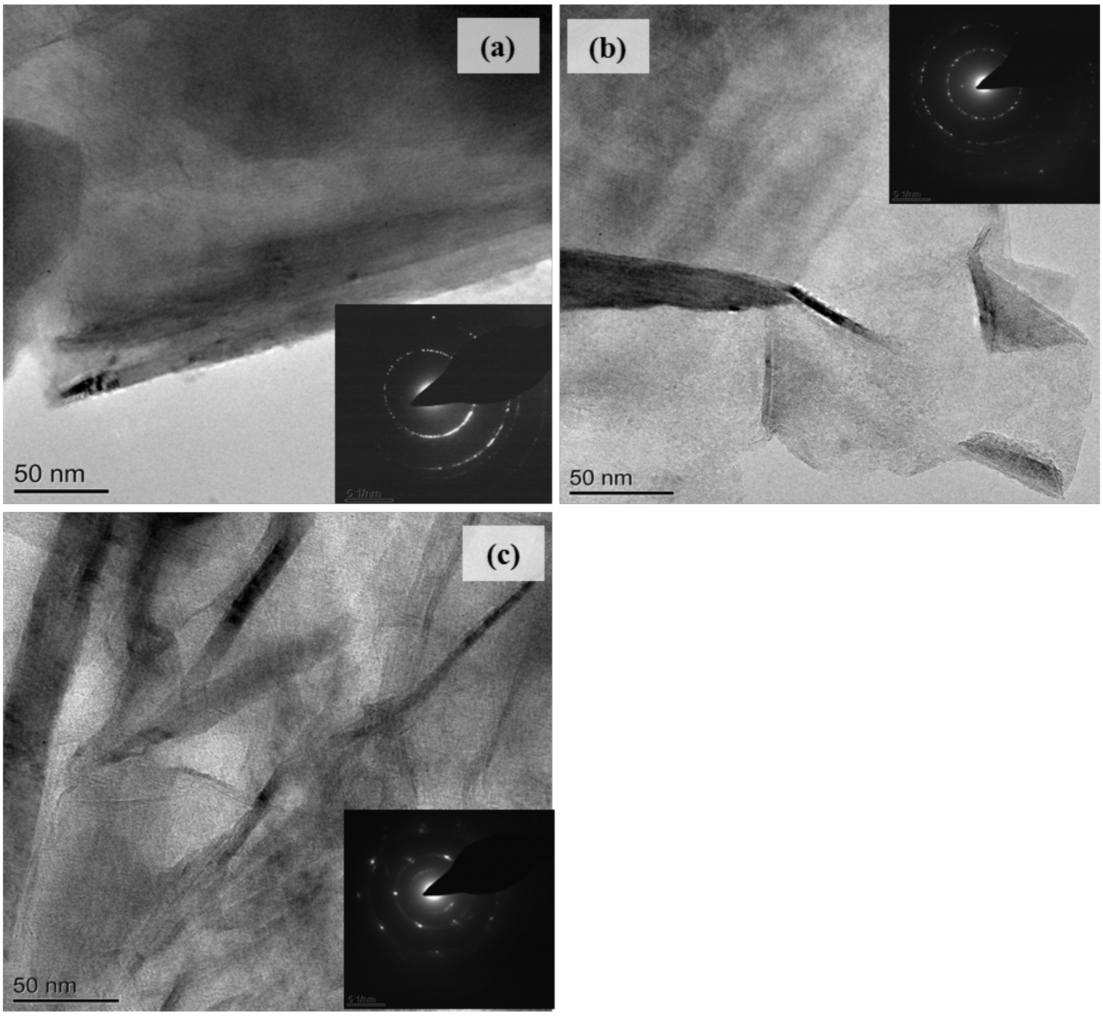

Figure 5.28 BF images with their SAED of: (a) virgin PCEA, (b) irradiated PCEA B17 and (c) irradiated PCEA B25.

The collection of images and their diffraction patterns, shown in Figure 5.29, displays the structural appearance of the PCIB sets of graphites analysed: virgin **PCIB** (Figure 5.29 (a)), irradiated **PCIB C03** with 1.5 dpa at ~350° C (Figure 5.29 (b)), **PCIB B02** which received 4 dpa at ~537,5 °C (Figure 5.29 (c)), and **PCIB B05** which received 6.8 dpa at ~659.9 °C (Figure 5.29 (d)).

For the **a**-direction, the constants values were as following: for PCIB ≈ 2.45 ± 0.04 Å, for PCIB C03 ≈ 2.39 ± 0.08 Å, for PCIB B02 ≈2.33 ± 0.05 Å, and for PCIB B05 ≈ 2.34 ± 0.05 Å. For the **c**-direction, the average data shows: PCIB ≈3.41 ± 0.1 Å, PCIB C03 ≈ 3.4 ± 0.08 Å, PCIB B02 ≈3.28 ± 0.06 Å, and PCIB B05 3.33 ± 0.06 Å. Comparing to the XRD data, for the **a-**direction the difference was lower by 0.09 Å, for the **c**-direction it was bigger for virgin PCIB and PCIB C03 by 0.06 Å, while for the other two, B02 and B05, the values measured by SAED were smaller in the range of 0.04 - 0.09 Å.

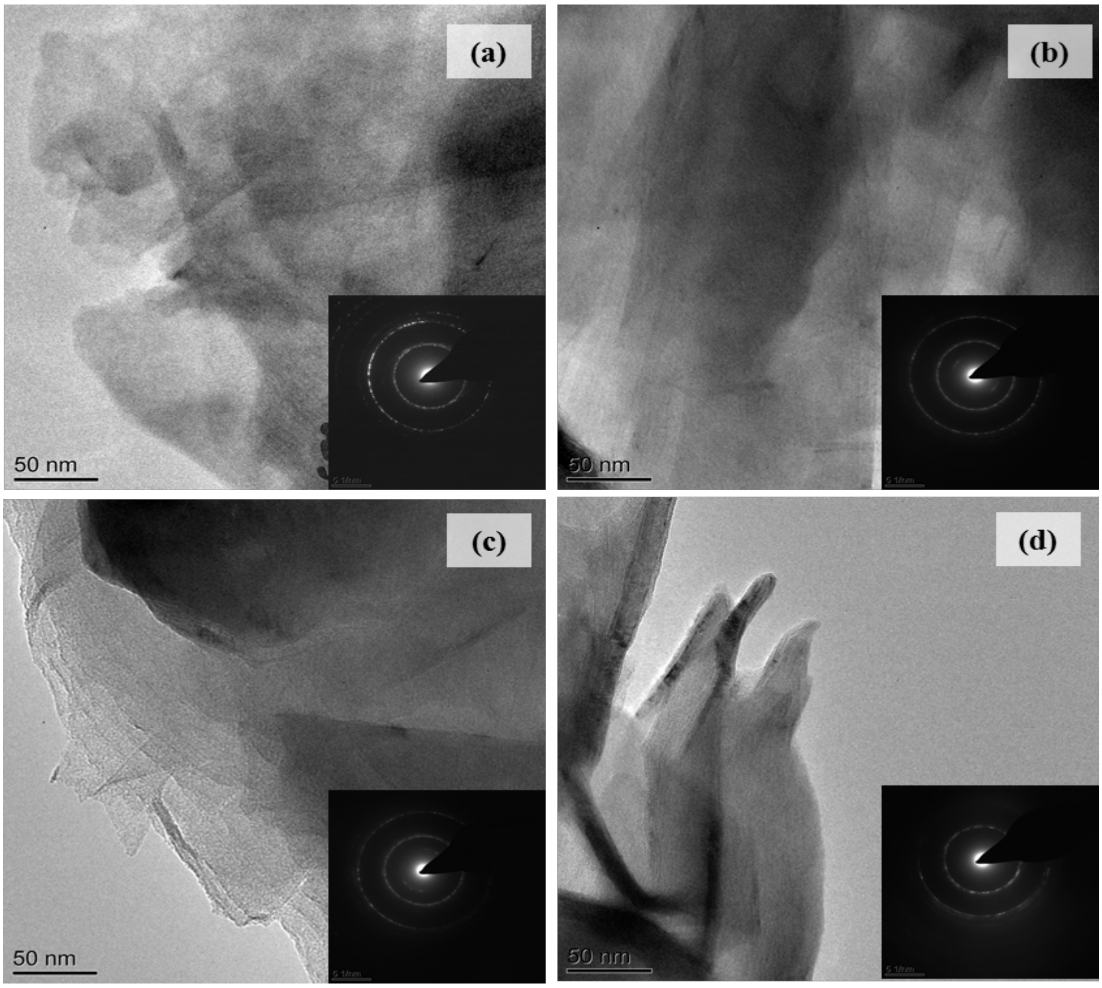

Figure 5.29 Typical BF images with their SAED of: (a) virgin PCIB, (b) irradiated PCIB C03, (c) irradiated PCIB B02 and irradiated PCIB B05.

The obtained values for PCIB set of materials for the **a** and **c** lattice parameters were lower for the irradiated graphite than the XRD and theoretical value suggesting a shrinkage of the plane due to accumulations of point defects within the lattice.

5.4.3. Electron energy loss spectroscopy

The PCEA and PCIB sets of irradiated graphites were analysed by using the proper parameters necessary for obtaining orientation independent EELS spectra from anisotropic specimens @80 keV (parameters established and described in the Chapter 3.

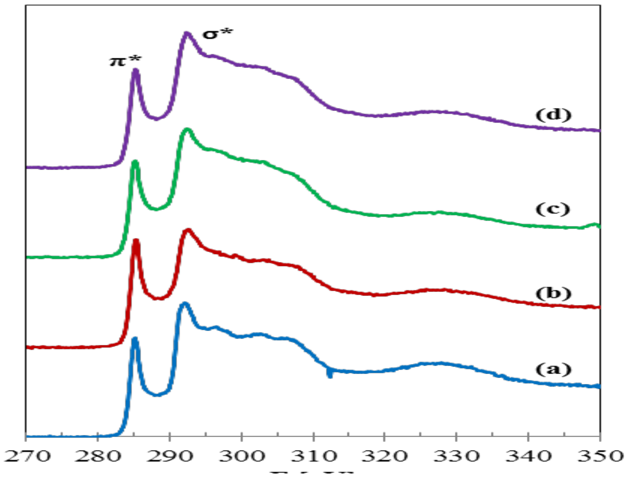

Figure 5.31 Characteristic EEL spectra of PCIB series representing the C K-edge of: (a) virgin PCIB; (b) C03 (1.5dpa, 350C); (c) B02 (4dpa, ~534C) ; (d) B05(6.dpa,~670C).

The information provided by EELS justifies the development of an irradiation damage mechanism on graphite. The stack of EEL spectra shown in Figure 5.31 are typical representation of the PCIB set of irradiated samples, while Figure 5.30 are representative spectra of PCEA set of irradiated samples.

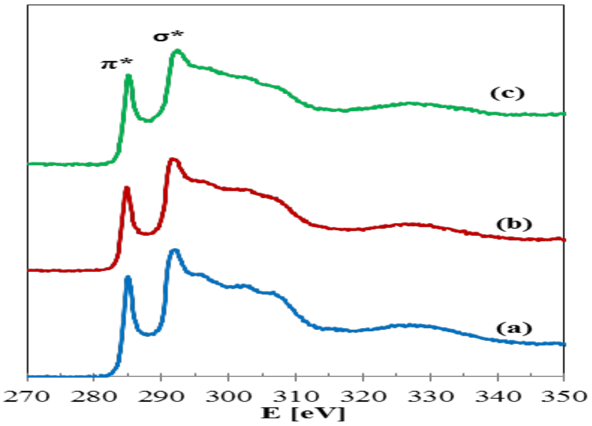

Figure 5.30 Characteristic EEL spectra of PCEA series representing the C K-edge of: (a) virgin PCEA; (b) B25 (1.5dpa, 350C); (c) B17 (6.8dpa~656C).

Considering the possible data biasing scenario which was assumed in the previous chapter, when choosing the regions to be used for EELS analysis, for every analysed sample shown within this section, at least 30 measurements/ sample were made.

I. Low loss region information of the analysed specimen

The bulk π+σ valence plasmon peak in the low loss region of the spectrum was analysed; the position of the peak being determined by taking the first derivative of the spectrum. The widely agreed value for the bulk plasmon peak position of highly oriented pyrolytic graphite (HOPG) in the literature is 27 eV [68,129,147,148] and for comparison, the corresponding value for amorphous carbon is 23 eV.

As illustrated in Figure 5.32 the plasmon peak energy for all analysed areas is consistently within the standard deviation limits of HOPG, but even so all have lower plasmon peak position compared to the theoretical value of 27eV.

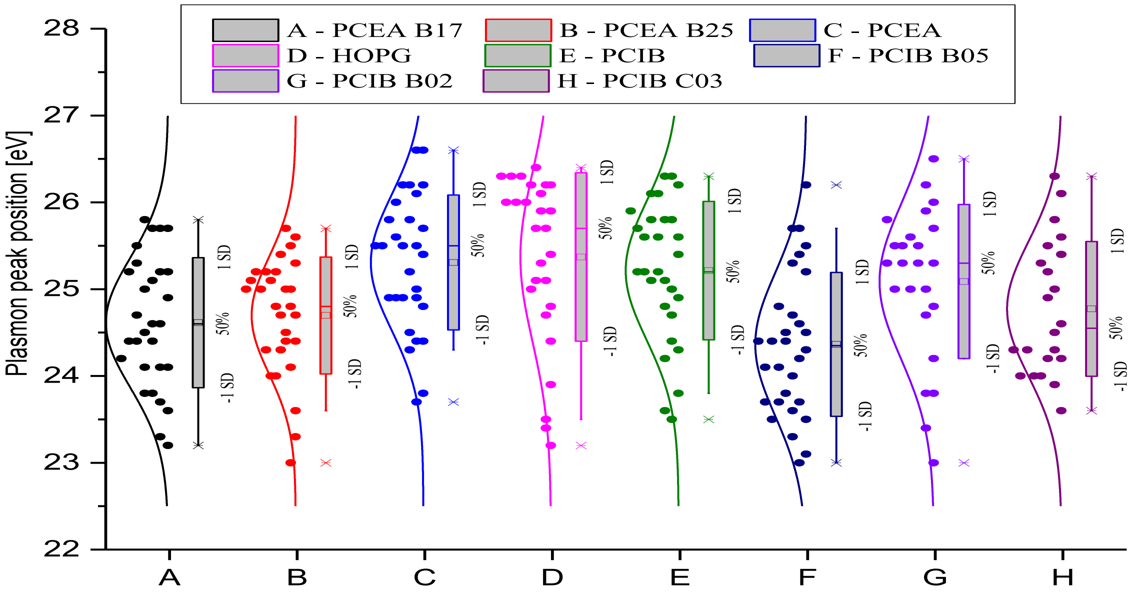

Figure 5.32 Box plot of the change in plasmon peak position. Data was collected from regions of electron transparent graphite oriented with the [002] direction perpendicular to the electron beam direction.

This situation may be due to the misorientation of the specimen's **c**-axis relative to the normal of the incident beam [149], in combination with the choice of the spectrometer collection angle [126,127] and again with the operator biasing choice. The comparison from the plot above of the plasmon peaks shows no significant change in plasmon peak position and hence density of the material.

II. Core Loss Region information of the analysed specimens

The position of the π* peak for all spectra was calibrated to 285 eV, and each C K-edge spectrum was acquired along with the corresponding low loss peak which was used to deconvolute the K-edge spectrum so as to remove plural scattering. Data extracted from the spectrum acquired from a standard HOPG sample was used to normalise subsequent sp^2 content data (procedure described in previous chapter). Note that even after intense neutron irradiation; the calculated sp^2 content for all analysed samples seems to have little change (Figure 5.33). This is thought to be from the sample preparation method, or from the bias choice of the analysed area of the operator.

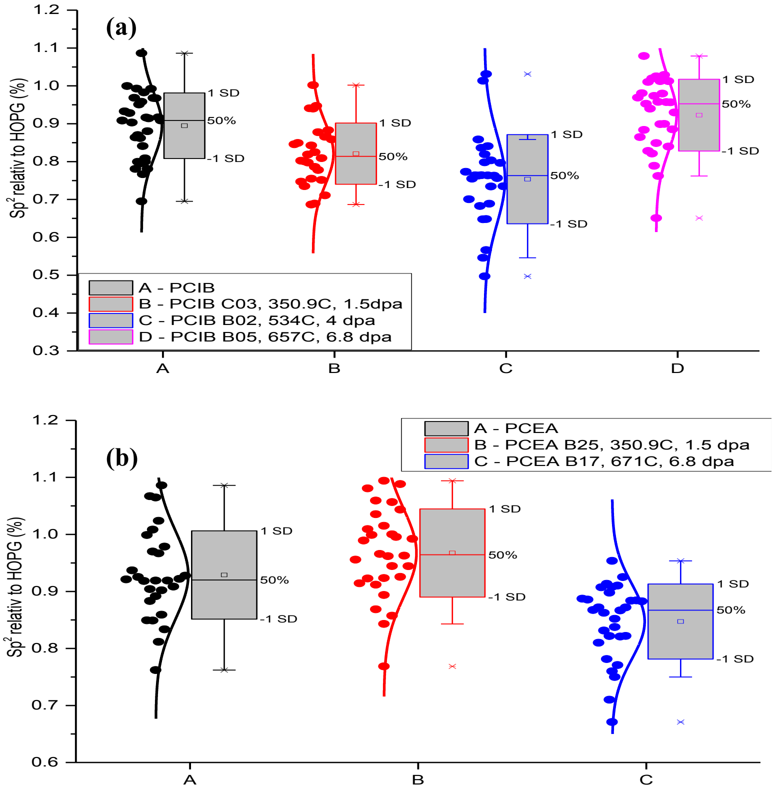

Figure 5.33 Box plot of the: (a) Change in planar sp^2 content within PCIB set;(b) Change in sp^2 content within PCEA set. Data was analysed using the 5 Gaussian fitting method.

This findings are in good agreement with the findings of Muto and Tanabe [75] who predicted that at electron irradiation beam of doses ~1dpa and irradiations temperatures higher than 356 °C, the irradiation should not change the local structure of graphite but simply fragment the crystallites.

Chapter 6 Summary and conclusions

6.1.Summary of work

Nuclear graphite properties are determined by its structure, which can be changed by the neutron irradiation dose and irradiation temperature. Inside a reactor, these parameters can significantly change the crystallite size and the lattice parameters of the graphite crystallites, with the **a**-axis contracting and the **c**-axis expanding - assuming that the crystallites are aligned with their **a**-axis parallel with the extrusion direction, so influencing bulk properties by interfering with the integrity and dimensions of nuclear graphite components. Even though the mechanisms are not totally understood, it is clear that the solidity and working life of reactor components are influenced by dimensional changes, amongst other effects of neutron irradiation [7]. For a better understanding of nuclear graphite structure, an investigation and a characterization of un-irradiated graphite was necessary along with the corresponding neutron irradiated graphites.

Considering the importance of the representation of structural factors mentioned above, by means of different characterization techniques (XRD, Raman Spectroscopy, TEM, EELS and SEM), information ranging from the atomic scale to the nano- and micro-scale structure were obtained from different grades of virgin and irradiated nuclear graphite. The chosen techniques not only provided valuable information on the different structures and properties, both when virgin or irradiated, but they were also a help in improving the methodology in order to facilitate future work on nuclear graphite. The improved methodology regarding the extraction of chemical bonding information from the C K-edge by automating the fitting of the EELS spectra, was shown to work on damaged the graphite structures irradiated at different doses by electron irradiation. Furthermore improvements were made in finding the damage and orientation-free acquisition parameters for analysing the graphitic structures when analysed by TEM-EELS techniques (e.g. the magic angle at 80 keV).

The analysis of virgin graphites by XRD showed a similarity in the measured lattice parameter, while the coherence lengths in both **a-** and **c**-direction vary, perhaps due to different precursors (especially the filler particle size obtained from the precursor). These range from 20.7 nm to 31.0 nm for the **c-**direction**,** and from 35.1nm to 61.7 nm for the **a**-direction. The calculated values were partially in agreement with the literature, although the L_a values were consistently higher than the ones reported in the literature, although we speculate in a recent paper [84] the authors used a shape factor of 0.9 instead of 1.84, the latter being more widely used by carbon researchers [3,116,135,160]

The Raman spectroscopy showed that the FWHM of the G peak varies linearly with I_D/I_G ratio. It is believed that while the intensity of the D peak arises from the edge boundaries (both crystallites and domains) and other defects present in the crystallite (e.g. dislocations), the FWHM of the G peak is more influenced by the point defects within the crystallites. It was also observed that none of the virgin graphites have a I_D/I_G ratio bigger than 0.4, with a FWHM of the G peak in the range of 14.5 – 29 cm^{-1}

Comparing the Raman and XRD results from virgin graphites, I_D/I_G ratio versus L_a shows a correlation, different for each type of graphite analysed, where by decreasing L_a leads to an increase in I_D/I_G as a result of increased crystallites boundaries per unit volume, this being in agreement with the literature [98,117,119]. There was found no correlation between the G peak position or the FWHM of the G peak with the L_a from XRD.

Considering the results obtained with all this techniques on the virgin graphites analysed, and also by adding the information found on the literature regarding the structure of graphite (e.g. point defects in graphite, Mrozovski cracks, values and change of L_a and L_c, pore structure), it was possible to propose a model of the virgin graphite which helped explain the changes exhibited by nuclear graphite when exposed to different irradiation parameters.

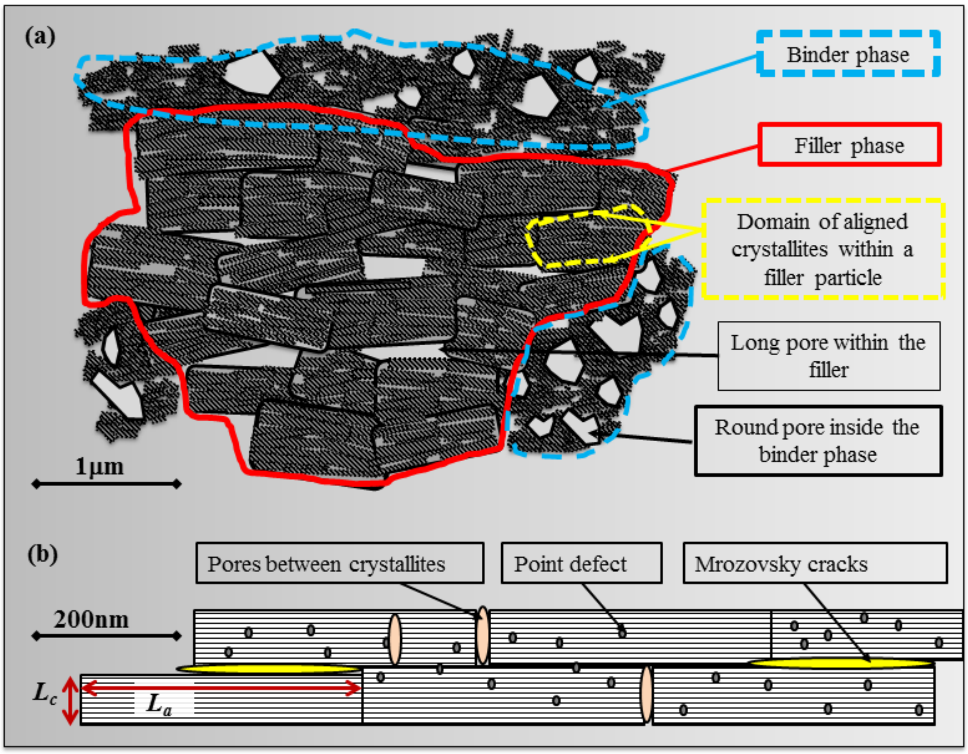

Figure 6.1 2D diagram representing: (a) Part of a needle shape filler particle with its components and (b) Nanometre scale representation of crystallites within the domains –yellow dashed in (a).

Figure 6.1(b) represents a schematic view of virgin graphite at nano scale, with the major components marked: long crystallites, cracks between crystallites (Mrozowski cracks), and nano pores. L_a and L_c represents the dimension of crystallites (or coherence lengths) in **a** and **c** directions, respectively. This is part of a larger filler/ binder microstructure shown in Figure 6.1 (a).

6.2. Accepted models for structural change of NG following irradiation

The accepted understanding of the nuclear graphite degradation is that, due to neutron irradiation, the **bulk** material should firstly shrink in the **a-**direction and swell in the **c**-direction, change that is accommodated by the cracks before turnaround and relieved by irradiation creep [7,44,161] when the cracks starts to open. However, even though the bulk nuclear graphite exhibits the changes mentioned above, based on different research studies, Baker [7] reported different a behavior happening at the atomic scale, e.g. due to neutron irradiation, the coherence length in the **c** direction (L_c) reduces its dimension, sometimes with even 75% (irradiation temperature ~300-1275 °C), phenomena which happens in different nuclear graphites [7]. The same author states that the dimensional change may be subject to the analysed sample dimensions and to the irradiation temperature and fluence. The expansion might be due to the creation of new pores as the result the strains produced by the incompatible crystallite. This pore generation was first observed in lower temperature irradiations but occurs at all temperatures when the internal strains exceed a critical value, which apparently varies from one graphite to another [44].

As mentioned in the previous chapters, graphite response to irradiation was researched using different types of irradiation beside neutrons e.g. ions or electrons. Muto and Tanabe [51,75], who studied the degradation of the atomic structure of graphite caused by both neutrons and ions, were the first who proved through TEM and Raman analysis the idea of fragmentation of the crystallites due to irradiation. Following previous research Shtrombakh *et al.* [54] proposed a model of the graphite crystallites fragmentations due to internal stress caused by irradiation.

Using different characterisation techniques described in the previous chapters, (XRD, Raman, TEM, SEM and EELS), ***the analysed graphites***, irradiated at relative lower fluencies, provided a series of data sets related to the atomic and micro structure of nuclear graphite. Based on the correlation of the results from all these techniques and based on the findings reported in the literature of the atomic structure degradation of graphite, a hypothesis of two possible irradiation regimes specific for these ***particular analysed samples*** was proposed.

6.2.1. Possible structural changes of nuclear graphite due to neutron irradiation with low dose-low temperature

For neutron irradiation at low doses (~1.5 dpa) and low temperatures (~350 °C), the degradation of the graphite structure can be seen easy from SEM images. Both irradiated graphite grades (PCEA and PCIB) revealed a change in the both the internal structure or the surface area. The PCEA graphite revealed a higher surface porosity with an increase in pore concentration with irradiation, however PCIB was influenced as well by the irradiation, but due to the small grain size, the surface pore area was more difficult to be measured with SEM analysis.

In PCEA case, the density of pores increased from 1 pore/mm^2 (for the virgin sample), to 9 pores /mm^2 (for B25 which was irradiated with low dose at low temperature), more the increase in the pore number came with the slight decrease in the dimension of the area of the pores from ~2500 μm^2 to ~2000 μm$^{2.}$

EELS and TEM analyses showed no difference in both lattice fringes and chemical bonding. From XRD analyses of irradiated samples, a change in the lattice parameter due to neutron irradiation was observed, with different responses to irradiation of PCEA compared to PCIB. For PCEA the lattice parameter was increased in the **c-**direction and decreased the **a**-direction, in agreement with the literature. In PCIB case the lattice parameter in the **c**-direction initial swelled followed by a decrease, while in the **a**-direction the change was inconclusive. However, the change in lattice parameters was not reflected in the dimensions of the crystallite coherence lengths, which decreased dramatically when irradiated at ~350 °C with ~1.5 dpa, in both the **c** and **a** directions (Table 4.5), indicating that the crystallites are breaking and forming more crystallites boundaries per unit volume presumably from the accumulation and diffusion and coalescence of defects.

Raman revealed a change in the FWHM of the G peak, as a result of irradiation with 1.5 dpa, suggested to be due to the accumulation of defects within the crystallites. For the same peak it was observed a change in position, to higher wave numbers, which is thought to be indicative of the transformation from graphite to nano-graphite [101]. This correlates with and increase on I_D/I_G ratio reflecting an increase in crystallites boundaries (and possibly more amorphous material inside the pores), shown by a decrease in both L_a and L_c , determined from XRD. All these statements are based on the assumption that defects can move and coalesce to form new crystallite boundaries.

Figure 6.2 is a schematic representation of the possible degradation process of ***the analysed nuclear graphite*** under irradiation of ~1.5 dpa at a temperature of ~350 °C. In

Figure 6.2 (b) the combination and multiplication of point defects is emphasized, along with the increase of porosity found by SEM.

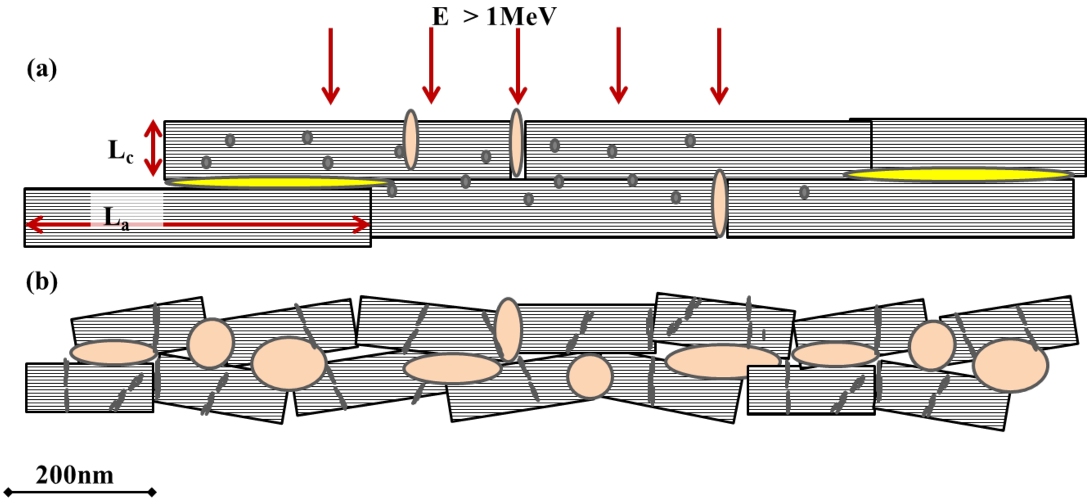

Figure 6.2 2D Schematic representation of the degradation of graphite from virgin graphite (a) under neutron irradiation of energies > 1MeV, corresponding to irradiation dose ≈1.5 dpa at temperatures ≈ 360C (b)

6.2.2. Possible structural changes of nuclear graphite due to neutron irradiation with high dose-high temperature

Following neutron irradiation at high temperature with higher doses (~6.8 dpa), it was observed that there was an annealing effect due to higher irradiation temperatures (~650 °C).

Although XRD showed a decrease in the L_c value, the same technique reveals an increase of the L_a, possibly due to the annealing of the basal plane point defects. The decrease in L_c of the crystallites was probably the main cause for the increase in porosity seen in SEM image analysis: the density of pores increased from 1 pores/mm^2 (for the virgin sample), to 10 pores/mm^2 (for B17). The increase in density of pores was accompanied with dimensional growth of the area of pores from an average of ~2500 μm^2, which increased to ~3200 μm^2.

Furthermore, Raman analysis revealed a slight decrease in both G peak position and FWHM of the G peak with irradiation. Although the irradiation dose increased from

1.5 dpa to 6.8 dpa, the fact that the temperature increased from ~350 °C to ~650 °C, resulted in a healing of the damage, particularly defects within crystallites. The evidence for this is in the observed decrease in the FWHM of the G peak with almost 50% of the value observed at ~650 °C as compared to the value found at 350 °C.

Again, no noticeable differences compared to virgin graphites were seen from the HRTEM images or EEL spectra of the irradiated samples with 6.8 dpa at ~650 °C. Together, all this information from the high dose irradiated samples at higher temperatures helped develop a second possible regime for ***the analysed nuclear graphite*** degradation.

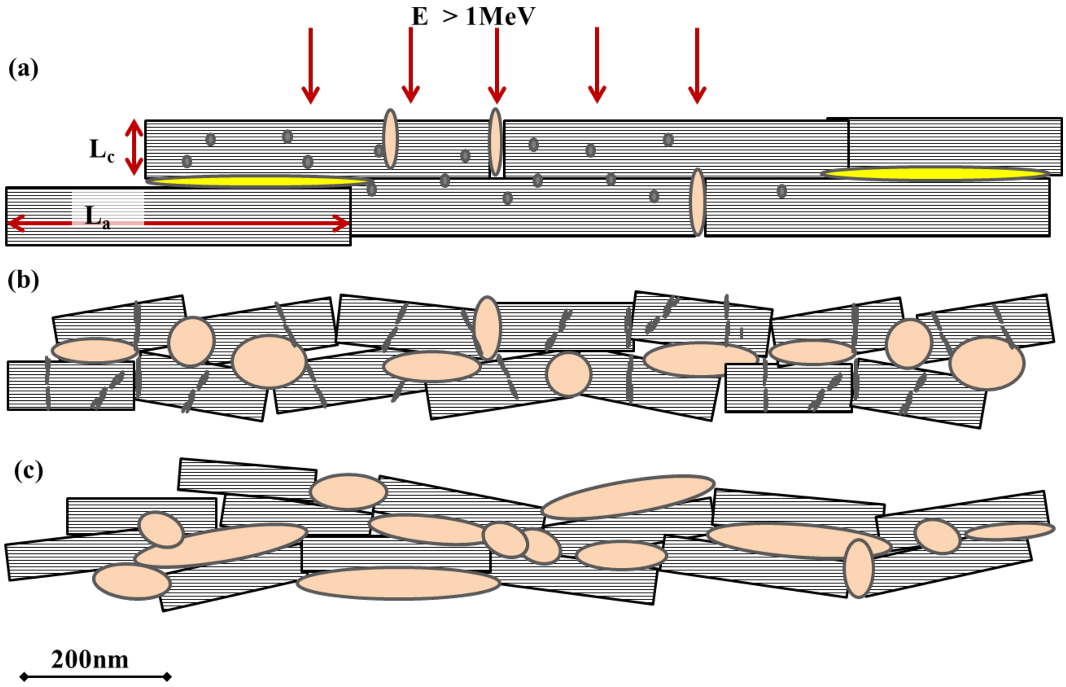

Figure 6.3 2D Schematic representation of the degradation of graphite from virgin graphite (a) under neutron irradiation of energies > 1MeV, corresponding to irradiation dose ≈1.5 dpa at temperatures ~360C (b) and ≈6.8dpa at ~650 C (c)

Figure 6.3 is a schematic representation of the two possible main regimes of degradation of ***the analysed nuclear graphite*** due to neutron irradiation. In Figure 6.3 (b) the first regime of is shown presenting degradation process at low doses and low temperatures, followed by Figure 6.3 (c) presenting the second possible degradation regime of nuclear graphite which occurs at high doses and high temperatures. In the second process, point defects are annealed due to higher temperatures, with an increase in coherence lengths in the **a**-direction, and an increase in the nano-porosity.

The proposed representation of graphite degradation needs further experiments to validate the suppositions on which the schematic representation is based on. By the fact that only the surface pores where taken in consideration by SEM and image analysis, the representation can be counted as wrong or biased, so further internal porosity has to be analysed by other technique e.g. XRD tomography, Gas Adsorption analysis. Also a more reliable representation would be based on graphites irradiated at ranges of temperature and doses between the already analysed ones (350-650 °C; 1.5 -6.8dpa).

The accepted understanding of the bulk nuclear graphite degradation is that the material should firstly shrink in the **a-**direction and swell in the **c**-direction, change that is accommodated by the porosity and relieved by irradiation creep after turnoaround. However, the ***analysed samples*** which received relatively low fluence, were investigated only from the point of view of atomic to micro scale and presented partially the same behavior reported in the literature (e.g. shrinkage of the L_c) by exhibiting a fragmentation of the crystallites [7] and an increase in the surface porosity.

The suggested schematic representation for the possible degradation due to neutron irradiation of ***these specific analysed*** nuclear graphites shows a similarity with the previous results reported in the literature, regarding the change happening at the atomic scale, due to different types of irradiation (e.g. neutron, electron and ion irradiation) of graphites which sustained a fragmentation of the crystallite that could be seen with TEM, X-ray Diffraction or Raman spectroscopy [51,54,73,74,78,152,162,163]. Nevertheless, as the measurements were done mostly at the atomic scale, a more thorough investigation has to be done in order to correlate dimensional changes, pores presence and atomic structure alteration with the bulk behaviour, and to explain fully the results.

6.3. Conclusions

The comparison between different types of nuclear graphites revealed valuable information related to structural differences of different analysed grade graphites, which were an aid in explaining the different behaviour of the two irradiated and distinct grade graphites analysed. Specifically, under the same irradiation parameters PCIB and PCEA have different responses provides important information regarding the choice of nuclear graphites to be used in nuclear reactors. The difference in dimension of the filler particle was seen to have influence on the increase in structural defects, PCEA showing a higher surface porosity irradiation compared to PCIB.

The comparison of virgin versus neutron-irradiated graphites gave the opportunity to propose an initial model for the degradation of graphite under different irradiation processes. However, because the experiments were conducted with different types of irradiation parameters (low dose-low temperature; high dose-high temperature), these results could only be used to develop an initial mechanism operating during neutron irradiation of the different graphite types, and there is a need for more experiments in order to assess the gaps regarding nuclear graphite responses for intermediate doses and temperatures.

Until now, the model of graphite fragmentation during irradiation was proposed only for electron irradiation with doses lower that 1 dpa and temperatures lower than 370 °C, as a result of point defect coalescence. Using a range of techniques, this work has showed that under the neutron irradiation, some graphite has the same behaviour of crystallite fragmentation with no significant change in carbon-carbon bonding. These results could lead to a new scenario for the nuclear graphite degradation under neutron irradiation, which can be completed with more precision by electron irradiation, by varying the parameters in order to achieve reactor-like conditions.

6.4. Future work

Highlighting the importance of nuclear graphite integrity and following the main objectives to design better graphite structures, by understanding the failures of the previous generations of graphite, it seems that a study of the structural properties of the crystallites, elucidation of the key nano-structural components during the degradation process appears the key in achieving safer and longer working nuclear plants.

The schematic representation proposed in this thesis, could be the first step in this research. Being a rudimentary model, in order to fill the gaps in knowledge and also to transform supposition into facts, more experiments are needed. The results of electron irradiation at room temperature show that temperature is an important factor in the structural change of graphite when irradiated.

Experiments, which could be improved in order to confirm both the schematic representation and also the response of graphite when irradiated, include:

1) Improvements the TEM sample preparation technique, in order to prove that the basal plane defects are forming and increasing due to neutron irradiation, and to confirm that contrast changes in the TEM images is due to sample preparation, Focused Ion Beam (FIB) milling would be a good choice in sample preparation;

2) Prepare and analyse a set of samples with increasing irradiation temperatures whilst keeping the dose constant;

3) Prepare and analyse a set of samples with increasing irradiation doses whilst keeping the temperature constant;

4) Compare effects of the same irradiation parameters on a set of nuclear graphites with differing starting microstructures.

5) A correlative study of porosity across the length scale (nano to micro to macro) and how this change with irradiation using FIB slices and view, X-ray tomography and nitrogen gas adsorption.

Appendix A Essential TEM calibration

If EELS is performed in TEM diffraction mode the important parameters are: beam convergence (α) and collection angle (2β), which have to be discussed together as the two are combined in quadrature to obtain an effective collection angle, $\beta_{ef.}$

A.1. Beam convergence (α)

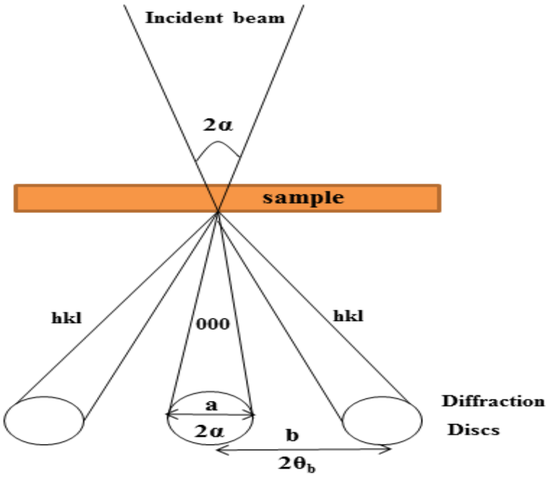

Figure A.1 Definition of incident beam convergence (α

After the microscope was aligned, the specimen was positioned at the eucentric height, by minimising the movement of the viewing plane when wobbling automatically the second condenser lens (C2) from under focus to over focus. The specimen was considered to be at the eucentric height when the image did not move from side to side but pulsed in the centre of the viewing screen.

When parallel beam illumination is used the diffraction pattern from a single crystal should look like an alignment of small and intense spots. For this calibration exercise, a single crystal test specimen of gold (gold foil Agar Scientific) was used.

The convergence values can be measured using Eq. A.1 with the details specified in Figure A.1. When using the Eq. A.1, it was known from Braggs law (Eq. 3.1) that for Au(002) θ_b= 6.204mrads with a spacing of 0.2039nm.

$$2\alpha = 2\theta_b * (a/b) \qquad \text{Eq. A.1}$$

If the incident beam is convergent, the small sharp dots forming the diffraction pattern will transform in to discs which will grow when changing the C2 current, up to the point of crossing over when they start to decrease again in size (Figure A.2).

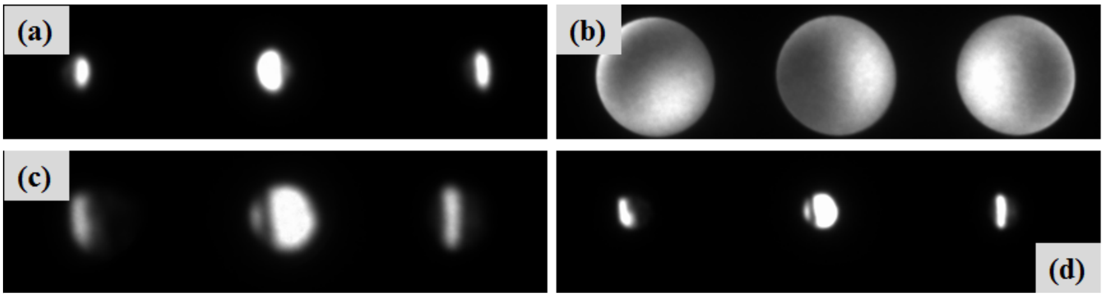

Figure A.2 Beam crossing over at sample: (a) C2=1100mA; (b)C2~1105(before cros over); (c)C3=1119mA; (d)C2=1123m

Figure A.2 shows the behaviour of the beam when changing the strength of the C2 current at 80 keV. Starting with the bigger current at 1132 mA, the beam is converging to a point – “cross-over” where the discs have their maximum dimensions in the diffraction plane (1108mA) after which the discs start to decrease their dimensions (1105mA). The changing strength of the C2 current is conventionally named “focus”, is “over focused” when the C2 current is the biggest and became “under focused” after the crossing over with lower lens current. As the convergence (α) is not equal when “under focused” and “over focused” even though the discs/spots have the same dimension, the agreed convention is to work in “over focused” conditions [164].

This data is plotted as the convergence angle vs C2 current (Figure A.3 (a) – (b)). Considering that the major part of the thesis was analysing carbon specimens - graphite (which gets damaged by an electron beam above 80 keV) the same procedure was done for both 200 keV and 80 keV.

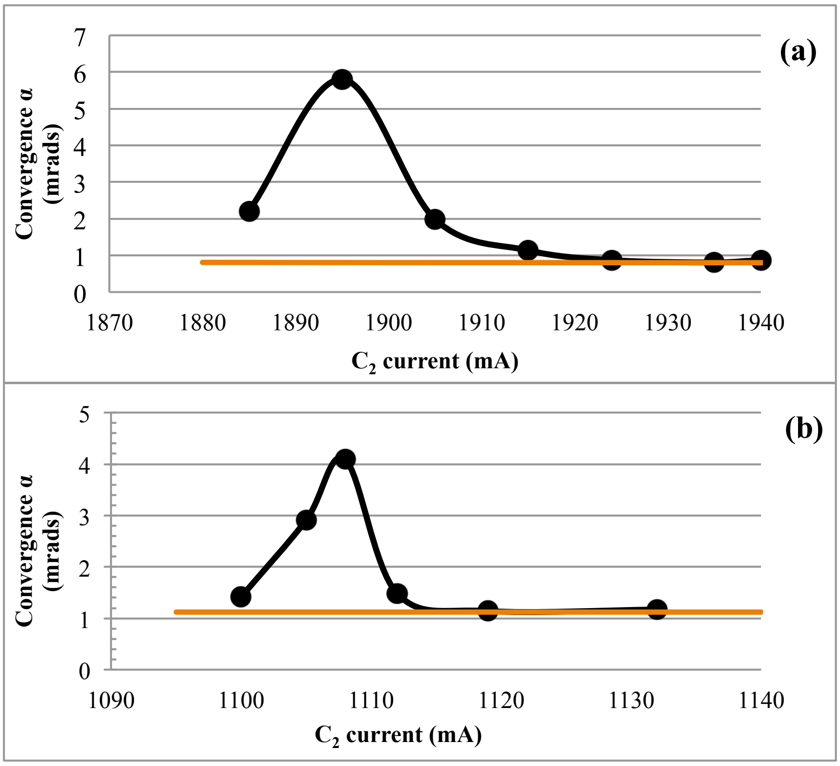

Figure A.3 Beam convergence semi-angle plot for: (a) 197 keV and (b) 80 keV (b)

From the plots showed in Figure A.3, it was possible to extract the value of convergence (α) at 200 keV and 80 keV. For 200 keV the convergence (α) was equal at 0.8mrads (as found before by Daniels [164] , while for 80 keV convergence (α) = 1.13mrads.

A.2. Collection angles; Imaging and Spectroscopy (Diffraction Mode)

The collection semi-angle (β) is a very important factor for as the collection of spectra at different β can cause misinterpretation if comparison between spectra is required. In image mode, the objective aperture controls the value of β. In diffraction mode, as used here, β is defined by the camera length (CL) of the diffraction pattern and the size of the spectrometer entrance aperture. Defining β is important as EEL spectra should be collected at the "magic angle" [139], at which the spectra are not influenced by the anisotropy of the sample [139,164–166].

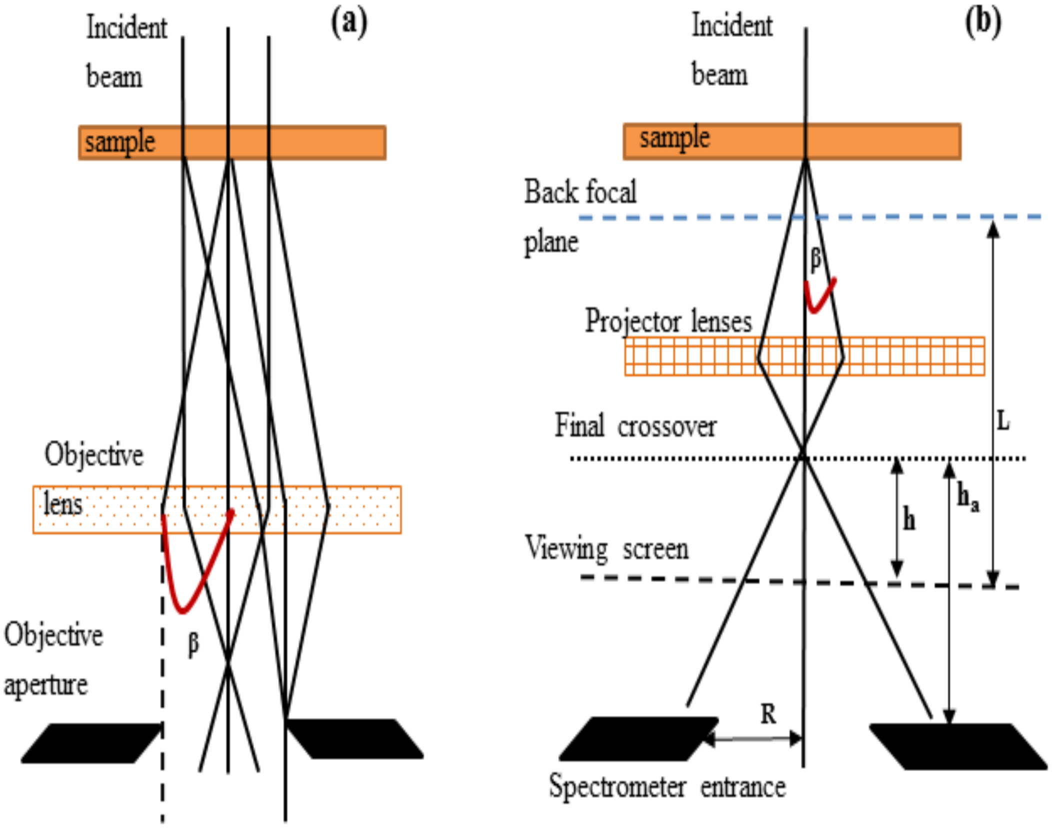

Figure A.4 Schematic diagram defining the collection semi-angle within: (a) image mode; (b) diffraction mode

Figure A.4 (b) defines the collection semi-angle, which has the mathematical formula:

$$\beta = \frac{L}{R} * \frac{h}{h_a} \qquad \text{Eq. A.2}$$

Where: β = Represents the collection semi-angle (mrads); L= Effective camera length (mm); R= Entrance aperture radius (mm); h= Distance from final projector crossover to the viewing screen (mm); h_a= Distance from final projector crossover to the spectrometer entrance (mm).

From previous research [139,164] it was known that at 200 keV the magic angle conditions for the carbon K- edge (E = 285 eV), were achieved at L=115mm camera length, which corresponded to a collection semi-angle (β) of 1.7mrads, using the entrance aperture of 0.6mm.

A.3. Camera length (CL) calibration

As mentioned before the camera length value has an important role in considering the calculation of geometrical collection semi-angle (β). When calibrating the CL at 80 keV the same test sample was used as when finding the beam convergence (α), namely Au(002) with a Bragg angle of θ_b= 6.204mrads with a spacing of 0.2039nm. The value of CL was calculated using the formula:

$$Rd = \lambda L \qquad \text{Eq. A.3}$$

Where L represents the camera length of the microscope at which the diffraction is collected, R is the distance from the incident spot to the first order spot, corresponding to the d_{hkl}, and θ is the angle at which the electron is scattered by the hkl plane (in a TEM the approximation $\sin\theta \approx \theta$ can be made as the scattering process happens at very small angles).

In Figure A.5, R is the distance between the incident beam and the nearest spot in the diffraction pattern of Au(002). The relativistic λ at 80 keV, was calculated using Eq. A.4, giving a relativistic λ=4.17x10^{-3}nm.

$$\lambda = \frac{h}{\left[2m_0eV(1+\frac{eV}{2m_0c^2})\right]^{1/2}} \qquad \text{Eq. A.4}$$

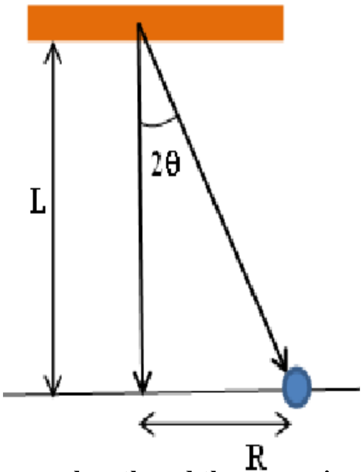

Figure A.5 Description of camera length and the connexion with diffraction pattern as presented in Eq. A.3

Having used the known constants it was found that the camera length for 80 keV changed according to the **Table A.1:**

Table A.1 Values of quoted and calculated camera length of the microscope

Nominal camera length (mm)	**Actual camera length (mm)**
42	37
62	48
84	63
115	98
150	128
210	182
300	193
420	348

A.4. Calibration of collection semi-angle (β)

For calibrating the value of **β**, one can use two methods. The first way is by using the existing calibration of the microscope, and second by recording a diffraction pattern of a known specimen, using a different entrance aperture for the GIF.

Method I. Using Eq. A.5 a table was made with the collection semi-angle (**Table A.2**), using h and h_a values of 389 respectively 728mm (for h_a the value supplied from FEI was changed from 638 to 728mm due to the instalment of a second Charge Coupled Device (CCD) camera).

Table A.2 Calculated collection semi-angle based on the values in Table A.1

Nominal camera length (mm)	Actual camera length (mm)	Collection Semi-Angle, β (mrads)		
		Entrance aperture radius , R (mm)		
		0.3	**1**	**1.5**
42	37	4.29	14.29	21.43
62	48	3.31	11.04	16.56
84	63	2.53	8.42	12.63
115	98	1.62	5.40	8.10
150	128	1.24	4.12	6.18
210	182	0.87	2.91	4.37
300	194	0.82	2.74	4.10
420	348	0.46	1.52	2.28
620	488	0.33	1.09	1.63
840	665	0.24	0.80	1.20

Method II. The second method of finding **β,** employed the GIF in image mode and visualise the 0.6 and 2mm diameter spectrometer entrance apertures directly and calibrate this against a known diffraction pattern.

The specimen used for this method was a Crocodilite sample, chosen because it has a big enough d-spacing (hence closer spaced diffraction pattern) to provide the desired information to calibrate the angular range of the spectrometer entrance aperture.

After the image acquisition of the diffraction pattern, the measurements were completed with a Digital Micrograph. It was observed that even though the 0.6 and 2mm diameter apertures fitted well onto the CCD, the measurements from different CLs were hard to complete due to the fact that the real CL at 80 keV has a smaller values than the equivalent value at 200 keV. Hence it was only possible to measure two, 62mm (actually 48.07 mm) and 84 mm (in real ~ 63.04), the first corresponding to Figure A.6. Knowing the d-spacing for the (020) diffraction spots for Crocodilite is d=0.903nm, with the calculated θ_b = 2.307mrads (@ 80 keV), it was possible to calculate the value of **β**. By this method the measured value of **β** was very close to the values found by the first method and for 62 mm **β** was found to be 3.63 mrad (compared to 3.31 mrad from the first method) and for 84 mm **β** had the value of 2.61 mrad (compared to 2.53 mrad from the first method). The small difference between the values of both methods were not taken in consideration as both method imply measurement errors due to both microscope and user, and the difference was not larger than 10% of the measured value.

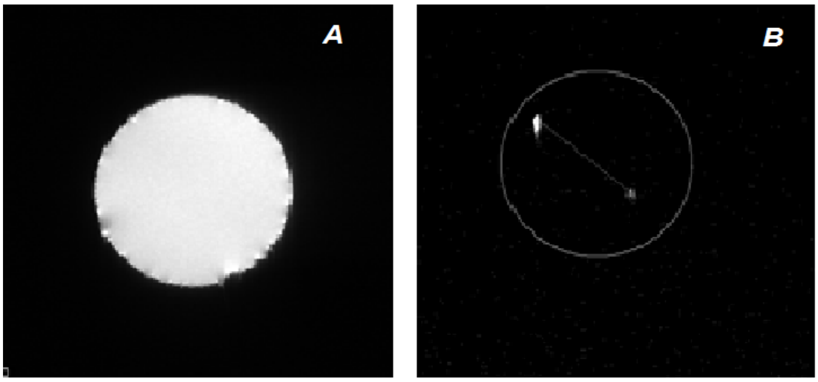

Figure A.6 Effective Collection Angle

This correlation shows that the calibration in **Table A**.2 (based on the microscope geometry) are an accurate representation of **β** values for EELS.

A.5. Effective collection semi-angle (β*)

As stated previously, the effective collection (β*) contains the information of both beam convergence (α) and collection semi-angle (β), which are linked in quadrature [127] as in Eq. A.6:

$$\beta^{*} = \sqrt{\beta^{2} + \alpha^{2}} \qquad \text{Eq. A.6}$$

The effective collection angle was calculated for different conditions using the above equation as seen in **Table A.3** Considering a convergence semi-angle **α** of 1.13mrad for 80 keV (see Figure A.3) for the values of **α** at high C_2 current).

The value of Magic angle (MA) at different accelerating voltages has been theoretically calculated by P. Schattschneider [141] and shown in Figure A.7.

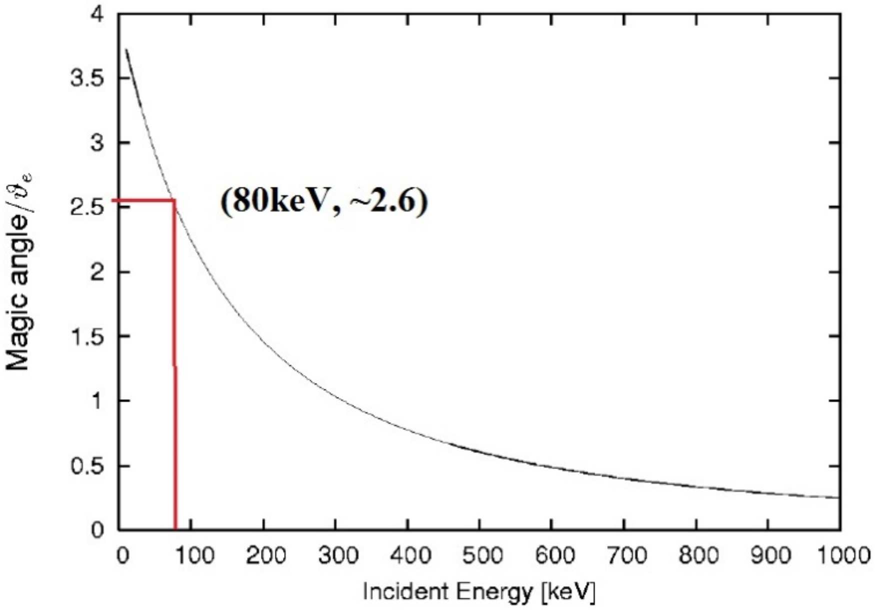

Figure A.7 Approximation of the MA as a function of accelerating voltage and characteristic scattering angle θ_E[141]

Table A.3 Collection angles and effective collection semi-angles at @80keV for both 0.6mm and 2mm entrance aperture

Camera lengths (mm)	Collection semi-angle β	Eff.Collection semi-angle β*	Collection semi-angle β	Eff.Collection semi-angle β*
Aperture	**0.6mm**	**0.6mm**	**2mm**	**2mm**
42	4.29	4.44	14.29	14.33
62	3.31	3.50	11.04	11.10
84	2.53	2.77	8.42	8.50
115	1.62	1.98	5.40	5.52
150	1.24	1.68	4.12	4.27
210	0.87	1.44	2.91	3.13
300	0.82	1.40	2.74	2.96
420	0.46	1.23	1.52	1.90
620	0.33	1.19	1.09	1.57
840	0.24	1.16	0.80	1.39

For 200 keV the MA is $\theta_M \approx 2\theta_E$ and calculated to be 1.7 mrad (for the carbon K-edge with θ_E= 0.84mrad as found by H. Daniels [139]), for 80 keV only the theoretical predications have been made by P. Schattschneider [141] for MA without any empirical evidence to support the calculations. The value at 80 keV is predicted to be ≈ 2.6 θ_E which for CK-edge is 4.63mrad (θ_E= 1.78mrad). **Table A.4** shows the values of **β*** in units of θ_E.

According to Jouffrey *et al* [142], the calculation of MA can vary with ± 0.3mrad at 200 keV and also added that the CL calibration can influence the calculation of MA with extra ±3%. Knowing that at the MA conditions, the orientation should not have any effect on the intensity of the two peaks at the C K-edge (π* and σ*), choice of MA was checked by comparing the C K-edge of a HOPG sample as a function of sample tilt.

Table A.4 Characteristic scattering angles θ_E for different CL[2]

CL (mm)	β^* (mrad)	β^* as units of θ_E	β^* (mrad)	β^* as units of θ_E
Aperture	**0.6mm**		**2mm**	
42	**4.44**	**2.49**	**14.33**	**8.05**
62	**3.50**	**1.97**	**11.10**	**6.23**
84	**2.77**	**1.56**	**8.50**	**4.77**
115	**1.98**	**1.11**	**5.52**	**3.10**
150	**1.68**	**0.94**	**4.27**	**2.40**
210	**1.44**	**0.81**	**3.13**	**1.76**
300	**1.40**	**0.79**	**2.96**	**1.67**
420	**1.23**	**0.69**	**1.90**	**1.07**
620	**1.19**	**0.67**	**1.57**	**0.88**
840	**1.16**	**0.65**	**1.39**	**0.78**

The calculated characteristic scattering angle θ_E @80 was found to be 1.78 mrad by using Eq.3.8). It can be seen from **Table A.4** that for 80 keV the nearest match to the theoretical MA of $2.6\theta_E$ is at: 1. CL=115mm (~98mm in true) and an acquisition aperture of 2mm, with a difference of plus 0.5 θ_E; 3. CL=150mm (~128mm in true) with a difference of minus 0.2 θ_E.

In order to check the lack of dependency on sample orientation, the ratio between a 5eV (window containing the π* peak) over a 20eV window (containing both σ* and π* peaks - (π*+ σ*)) was plotted for both CL=115mm and CL=150mm conditions (Figure A.8). The differences were found to be small between the two parameters with a bigger variation while the tilting series was acquired for the 150 mm, but this could be due to the instability of the microscope, so a different method needed to be applied in order for a decision to be made.

---

[2] Highlighted in green are the closest values which match the theoretical MA

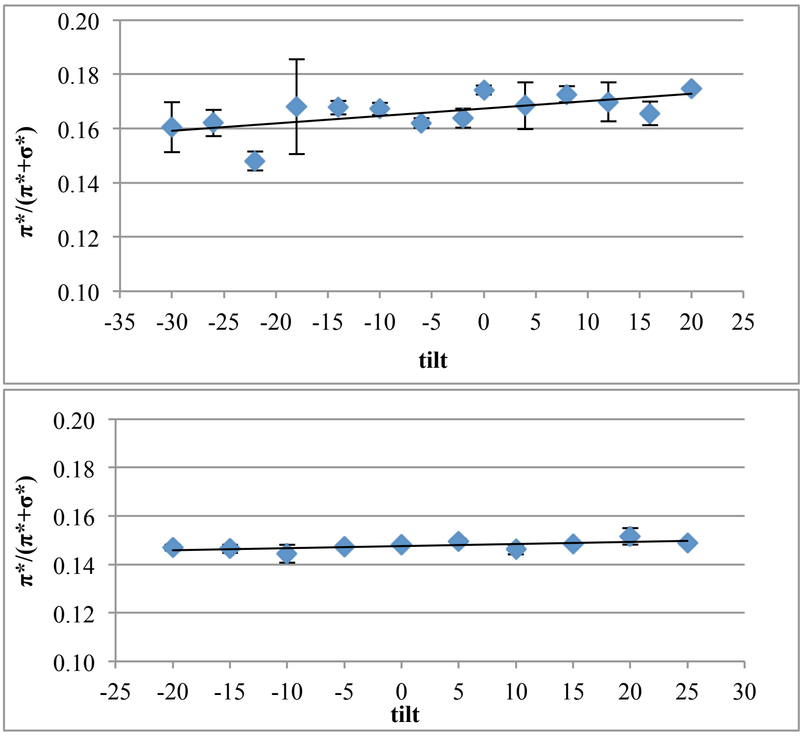

Figure A.8 Comparison of tilt series at (a).CM=150mm and (b) CM=115mm using an aperture of A=2mm

The decisive method was the comparison of C K-edge shape for both camera lengths of interest (Figure A.9). Even though the intensity ratio between the two windows (5 eV and 20 eV) was maintained during the tilting series it was observed that at CL=150 mm the shape of the π* peak was larger relative to the σ* peak, a sign that the magic angle conditions were not satisfied.

In the case other case, CL= 115 mm, the relative intensities of the two peak , appear to agree to theory [127]. It was considered that the closest to the MA value and was used for all measurement at 80 keV

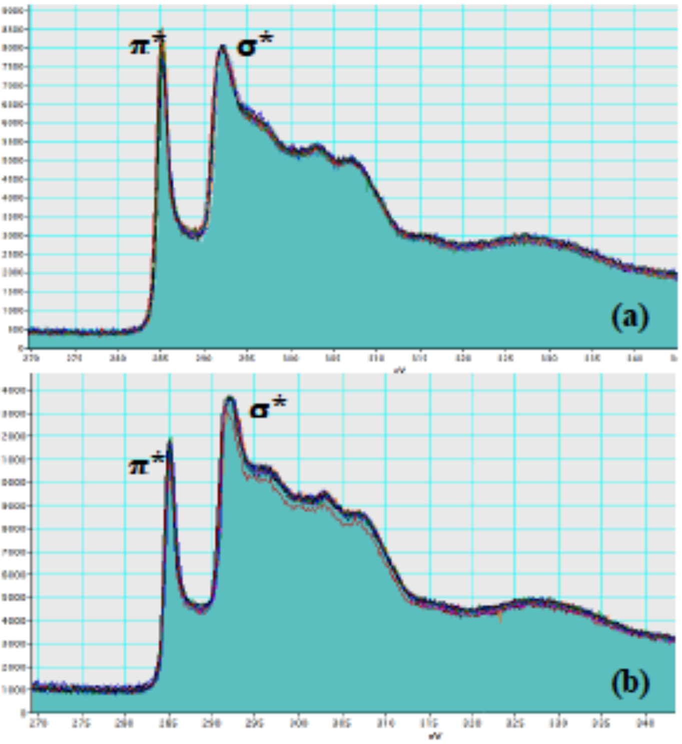

Figure A.9 Overlapped EEL spectra for the tilt series of at (a) CM=150mm and (b) CM=115mm

Appendix B Sample irradiation process

The information presented in this section is subtracted from INL US, reports (2011-2013) [2,79,167] containing irradiation parameters data along with the description of irradiation facility.

The graphites analysed in this thesis were subject to various irradiation processes as part of the existing plan to build the Next Generation Nuclear Plant (NGNP) which will be a helium-cooled and part of very high temperature reactor (VHTR) using graphite as moderator in the core. The previous nuclear reactors (both research and commercial), build in United States, were graphite based, using H-451 (medium grain, near-isotropic, extruded nuclear graphite, and no longer available [168]). Hence new developed graphites needed to be designed and tested in order to successfully replace and be suitable to be used in the new generation of reactors.

Knowing the induced irradiation creep due to high irradiation temperatures, neutron irradiation and applied stress, all graphites were irradiated as part of Advanced Graphite Creep-1 (AGC-1) experiment which took place in the Advanced Test Reactor (ATR) in a large flux trap at the Idaho National Laboratory (INL) Site. The experiment is designed to sustain 6 irradiation capsules (Figure B.1) that can hold ~500 graphite samples, and to have the neutron irradiation doses in the rage of 0.5 - 7 dpa, at temperatures up to 1200°C. Between the graphites irradiated is worth mentioning: NBG-18, PCEA, IG-110, and from the minor grades of graphite (i.e., “piggyback” specimens) PCIB and HOPG [167].

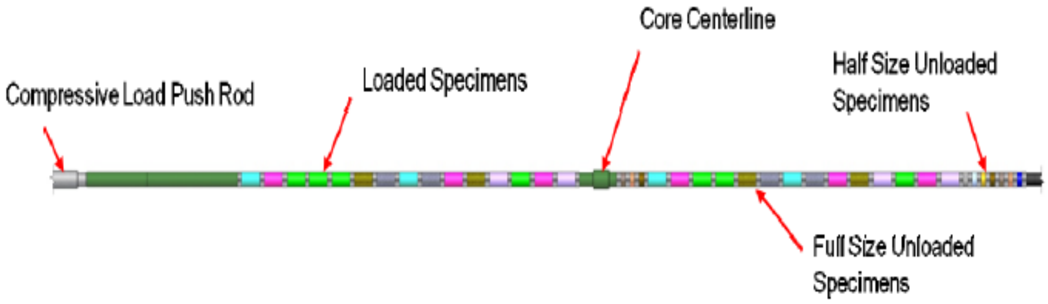

Figure B.1 Schematic representation of an AGC-1 capsule sample stack [79].

The AGC-1 capsule was irradiated in the south flux trap of the ATR from September 5, 2009 to January 8, 2011 crossing seven irradiation cycles (approximately 378 effective full-power days). After irradiation, completed on January 8, 2011, the AGC-1 capsule was stored in the ATR Canal for approximately 60 days to allow the activity of the steel pressure tube section of the capsule to decay to lower levels, following the disassembly of the capsules [2].

In order to ensure that the similar samples (top-bottom) receive the same dose the staking of sample had to match the ATR flux profile, which is asymmetric (Figure B.2) due to the core components are altering the profile. This request of insuring for similar samples to receive similar doses, was achieved by loading in the bottom of the capsule couple more piggyback samples next to de core centreline. However, more samples were irradiated from the new designed ones (e.g. PCEA) compared to the old generation H451, in order to ensure a higher variety of irradiation temperatures and doses.

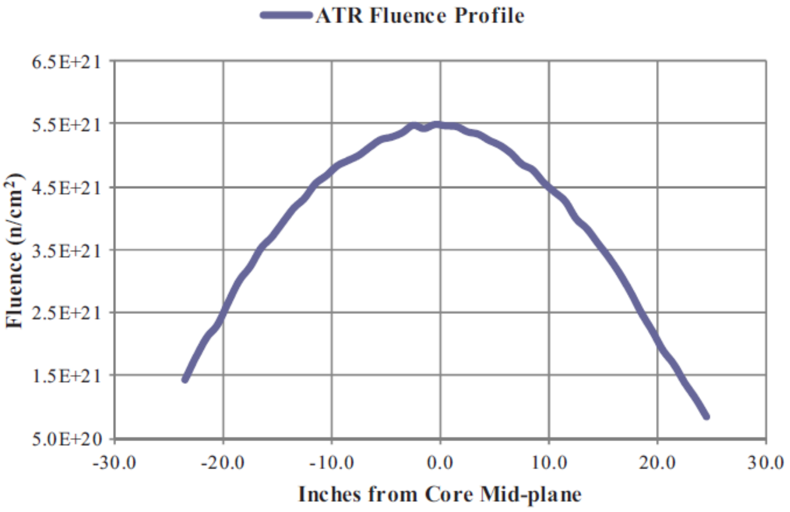

Figure B.2 ATR flux profile during irradiation [79]

When staking the samples it was taken in consideration, also the orientation of the grain size relative to the irradiation load, knowing that irradiation creep is influenced by the orientation of the grain (being more important the measurements with the load applied parallel to the grain). The experiment ensured that each capsule was irradiated at constant temperature, and only the dose and the load was varied.

The AGC-1 samples, which finished their irradiation cycle in January 2011, had an accumulated dose in the range of 1.36 - 6.94 dpa. Being the first experiment done as part of AGC, it had issues from the software in controlling the temperature; in the way that the temperature was not uniforms (Figure B.3) through the capsule, and the irradiation temperature was raised to ~675 °C. During irradiation the variation of temperature within the entire capsule was 350 °C with doses in the range of 1.82 - 6.94 dpa. The temperature variation between matched pair samples in this central region ranged from a low of 30 °C to a high of 68 °C between sample pairs, these temperature variations are higher than planned, but within acceptable levels of uncertainty [79].

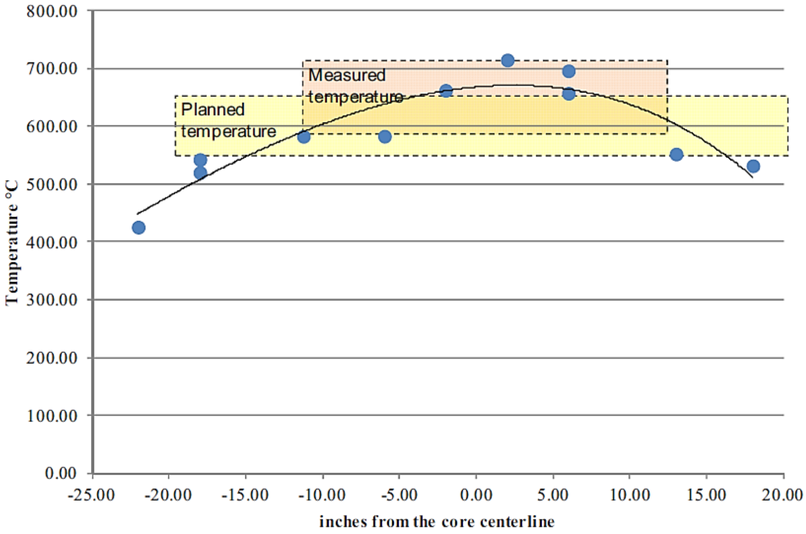

Figure B.3 Temperature variation within the ATR irradiation capsule [79]

NOTE: The sample analysed in this thesis, were a part of the central capsule, and no load was applied.

Appendix C Displacement cross section

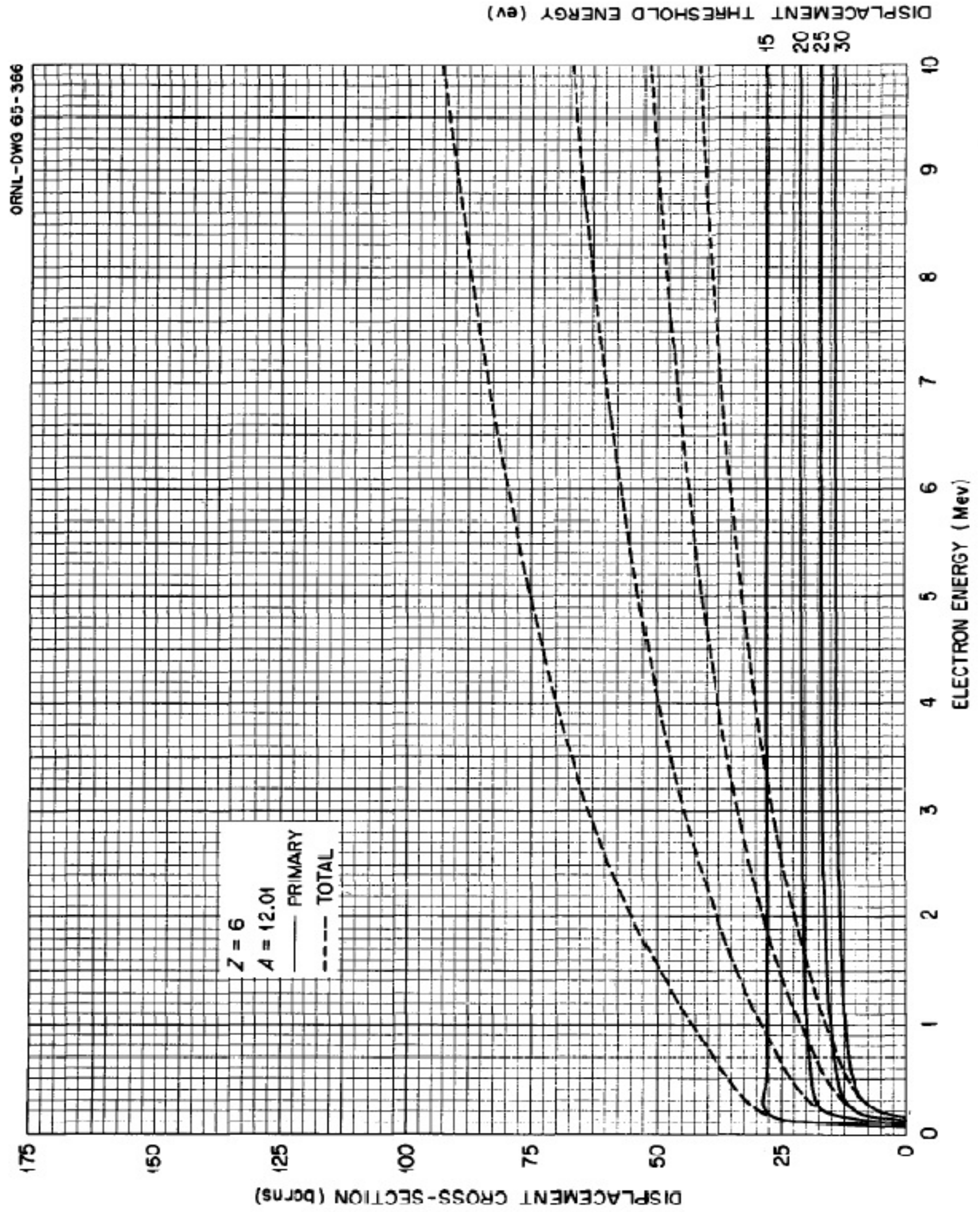

Figure C.1 Carbon primary and total displacement cross section as a function of electron and displacement threshold energies (capture from Oen (1965).

BIBLIOGRAPHY

[1] Department of Energy & Climate Change (DECC), Department of Eenergy & Climate Change (DECC). Table of past and present nuclear reactors in the UK. London: 2014.

[2] Swank W. AGC-1 Post-Irradiation Examination Status. 2011.

[3] Nightingale RE. Nuclear Graphite. Academic Press Inc.; 1962.

[4] Mrozowski S. Mechanical strength, thermal expansion and structure of cokes and carbons. Proc Conf Carbon 1954:31.

[5] Reynolds WN. Physical properties of graphite. Elsevier Publishing Co. LTD; 1968.

[6] Wen K, Marrow J, Marsden B. Microcracks in nuclear graphite and highly oriented pyrolytic graphite (HOPG). J Nucl Mater 2008;381:199–203. doi:10.1016/j.jnucmat.2008.07.012.

[7] Baker DE. Graphite as a neutron moderator and reflector material. Nucl Eng Des 1970;14:413–44. doi:10.1016/0029-5493(70)90160-3.

[8] Simmons JHW. Radiation damage in graphite. vol. 102. Pergamon Press; 1965.

[9] Kelly BT. Physics of graphite. 1981.

[10] Bacon GE, Warren BE. X-ray diffraction studies of neutron-irradated graphite. Acta Cryst 1956. doi:10.1107/S0365110X56002989.

[11] Heggie MI, Suarez-Martinez I, Davidson C, Haffenden G. Bukled, ruck and tuck: A proposed new model for the response of graphite to neutron irradiation. J Nucl Mater 2011;413. doi:10.1016/j.jnucmat.2011.04.015.

[12] WTA. World Nuclear Association n.d. world-nuclear.org.

[13] Mantell CL. Carbon and graphite handbook. New York: Interscience Publishers; 1968.

[14] Pierson HO. Handbook of carbon, graphite , diamond and fullerenes. Noyes Publications; 1993.

[15] Kroto* HW, Heath JR, O'Brien SC, CurlL RF, Smalley RE. C60: Buckminsterfullerene. Nature 1985;318:162–3. doi:doi:10.1038/318162a0.

[16] Kratschmer W, Lamb LD, Fostiropoulos K, Huffman DR. Solid C60: a new form of carbon. Nature 1990;347:354–8. doi:doi:10.1038/347354a0.

[17] Dresselhaus MS. Future directions in carbon science. Annu Rev Matterials Sci 1997;27:1–34. doi:10.1146/annurev.matsci.27.1.1.

[18] Abergel DSL, Apalkov V, Berashevich J, Ziegler K, Chakraborty T. Properties of graphene: a theoretical perspective. Adv Phys 2010;59:261–482. doi:10.1080/00018732.2010.487978.

[19] Oberlin A. Carbonization and graphitization. Carbon N Y 1984;22:521–41.

[20] Metals E. Graphite-Pyrolytic Grade. 2015.

[21] Rantala J. Pyrolytic graphite – thermal performance by structure. Electron Cool 2002.

[22] Vaughan DJ. Handbook of Mineralogy: Volume I; Elements, Sulfides, Sulfosalts. Mineral Mag 1991;55:146–7. doi:10.1180/minmag.1991.055.378.20.

[23] AIST-NT Inc. HOPG. Http://nanoprobes.aist-Nt.com n.d. http://nanoprobes.aist-nt.com/apps/HOPG.

[24] Powell RL, Childs GE. American Institute of Physics Handbook. McGraw-Hill, New Yor; 1972.

[25] Lemak RJ. High Performance Pyrolytic Graphite Composite Heat Spreaders. 2011.

[26] Thrower PA. Impurity nucleation of irradiation damage in graphitee. J Nucl Mater 1964;12:56–60.

[27] Mercuri RA, Criscione JM. Nuclear graphite 1985.

[28] Atomics G. Graphite design handbook. General Atomics for the Department of Energy; 1988.

[29] Burchell TD, Bration R, Windes W. NGNP Graphite Sel & Acquisition Strategy. 2007.

[30] Windes WE. Graphite Technology Development Plan. 2010.

[31] Kane J, Karthik C, Butt DPP, Windes WEE, Ubic R. Microstructural characterization and pore structure analysis of nuclear graphite. J Nucl Mater 2011;415:189–97. doi:10.1016/j.jnucmat.2011.05.053.

[32] Ubbelholde AR, Lewis FA, Taverna D, Kociak M, Charbois V, Henrard L. Graphite and its crystal compounds. Oxford University Press 1960; 1960.

[33] Energy USD of. DOE Fundamentals Handbook - Nuclear physics and reactor theory. Vol. 2 2, vol. 2, 1993.

[34] Epiney AS. Improvement of the Decay Heat Removal Characteristics of the Generation IV Gas-cooled Fast Reactor. Ecole Polytechnique Federale de Lausanne, 2010.

[35] http://www.world-nuclear.org/info/Nuclear-Fuel-Cycle/Power-Reactors/Appendices/RBMK-Reactors/ n.d. http://www.world-nuclear.org.

[36] Haag G. Properties of ATR-2E Graphite and Property Changes due to Fast Neutron Irradiation. 2005.

[37] Walker L, Thrower PA. Chemistry and Physics of Carbon. vol. 1. Edward Arnold Ltd., London; 1973.

[38] Nordlund K, Keinonen J, Mattila T. Formation of Ion Irradiation-Induced Small-Scale Defects on Graphite Surfaces. Phys Rev Lett 1996;77:699–702. doi:10.1103/PhysRevLett.77.699.

[39] Smith R, Beardmore K. Molecular dynamics studies of particle impacts with carbon-based materials. Thin Solid Films 1996;272:255–70. doi:10.1016/0040-6090(95)06052-9.

[40] Yazyev O, Tavernelli I, Rothlisberger U, Helm L. Early stages of radiation damage in graphite and carbon nanostructures: A first-principles molecular dynamics study. Phys Rev B 2007;75:115418. doi:10.1103/PhysRevB.75.115418.

[41] Kelly BT. The theory of irradiation damage in graphite. Carbon N Y 1977;15:117–27. doi:10.1016/0008-6223(77)90027-6.

[42] Latham CD, Heggie MI, Alatalo M, Oberg S, Briddon PR. The contribution made by lattice vacancies to the Wigner effect in radiation-damaged graphite. J Phys Condens Matter 2013;25:135403. doi:10.1088/0953-8984/25/13/135403.

[43] Trevethan T, Dyulgerova P, Latham CD, Heggie MI, Seabourne CR, Scott AJ, et al. Extended Interplanar Linking in Graphite Formed from Vacancy Aggregates. Phys Rev Lett 2013;111:95501. doi:10.1103/PhysRevLett.111.095501.

[44] Kelly BT. Graphite - the most fascinating nuclear material 1982. doi:10.1016/0008-6223(82)90066-5.

[45] Windes W, Burchell T, Bratton R. Graphite Technology Development Plan. 2007.

[46] Thrower PA, Reynolds WN. Microstructural changes in neutron-irradiated graphite. J Nucl Mater 1963;8:221–6. doi:10.1016/0022-3115(63)90037-0.

[47] Thrower PA. Impurity nucleation of irradiation damage in graphitee.pdf. J Nucl Mater 1964;12:56–60.

[48] Thrower PA. The influence of crystal perfection on defect nucleation in graphite irradiated at high temperatures. Carbon N Y 1968;6.

[49] Burleigh DD, Thrower PA. Irradiation damage to pyrolytic graphites at very high temperatures. Carbon N Y 1973;11:505–10.

[50] Niwase K, Nakamura K, Shikama T, Tanabe T. On the amorphization of neutron-irradiated graphite. J Nucl Mater 1990;170:106–8.

[51] Tanabe T, Muto S. Reduction of the crystalline size of graphite by neutron irradiation. J Nucl Mater 1990;175.

[52] Niwase K. Raman Spectroscopy for Quantitative Analysis of Point Defects and Defect Clusters in Irradiated Graphite. Int J Spectrosc 2012;2012:1–14. doi:10.1155/2012/197609.

[53] Brocklehurst JEE, Kelly BTT. Analysis of the dimensional changes and structural changes in polycrystalline graphite under fast neutron irradiation. Carbon N Y 1992;31:155–78. doi:10.1016/0008-6223(93)90169-B.

[54] Shtrombakh YI, Gurovich BA, Platonov PA, Alekseev VM. Radiation damage of graphite and carbon-graphite materials. J Nucl Mater 1995;225:273–301. doi:10.1016/0022-3115(95)00060-7.

[55] Lokajicek T, Lukas P, Nikitin AN, Papushkin I V., Sumin V V., Vasin RN. The determination of the elastic properties of an anisotropic polycrystalline graphite using neutron diffraction and ultrasonic measurements. Carbon N Y 2011;49:1374–84. doi:10.1016/j.carbon.2010.12.003.

[56] Price RJ, Bokros JC. Annealing of neutron-irradiated pyrocarbons. Carbon N Y 1971;9:555–72.

[57] Kelly BT, Martin WH, Nettley PT. Dimensional Changes in Polycrystalline Graphites under Fast-Neutron Irradiation. Philos Trans R Soc A Math Phys Eng Sci 1966;260:51–71. doi:10.1098/rsta.1966.0029.

[58] Brocklehurst JE, Kelly BT. Analysis of the dimensional changes and structural changes in polycrystalline graphite under fast neutron irradiation. Carbon N Y 1992;31. doi:10.1016/0008-6223(93)90169-B.

[59] Kelly BT, Burchell TD. Structural-related property changes in polycrystalline graphite under neutron iradiation. Carbon N Y 1994;32. doi:10.1016/0008-6223(94)90172-4.

[60] Henson RW, Perks JA, Simmons JHW. Lattice parameter and dimensional changes in graphite irradiated between 300 and 1350°C. Carbon N Y 1968;6:789–806. doi:10.1016/0008-6223(68)90065-1.

[61] Henson RW, Reynolds WN. Lattice parameter Changes in irradiated graphite 1965:277–87. doi:10.1016/0008-6223(65)90062-X.

[62] Karthik C, Kane J, Butt DPPP, Windes WEEE, Ubic R. In situ transmission electron microscopy of electron-beam induced damage process in nuclear grade graphite. J Nucl Mater 2011;412:321–6. doi:10.1016/j.jnucmat.2011.03.024.

[63] Thrower PA. The structure of reactor graphites and its relation to high temperature irradiation dimensional stability. Carbon N Y 1971;9.

[64] Thrower P a. Interstitial loops in graphite, their motion and their effect on elastic modulus. Philos Mag 1967;16:189–209. doi:10.1080/14786436708229268.

[65] Marsden BJ. Irradiation Induced Dimensional and CTE Changes in Graphite. PPT 2008.

[66] Rappeneau J, Bocquet M, Micaud G, Fillatre A. Effets de l'irradiation sur les proprietes physiques du graphite. Carbon N Y 1964;1:97–109. doi:10.1016/0008-6223(64)90063-6.

[67] Pedraza DF, Koike J. Dimensional changes in grade H-451 graphite due tu electron irradiation. Carbon N Y 1993;32. doi:10.1016/0008-6223(94)90095-7.

[68] Egerton RF. Electron energy-loss spectroscopy in the TEM. Reports Prog Phys 2009;72:016502. doi:10.1088/0034-4885/72/1/016502.

[69] Koike J, Pedraza DF. Structural changes of graphite during electron irradiation 1993;279:67–72.

[70] Takeuchi M, Muto S, Tanabe T, Arai S, Kuroyanagi T. Damage process in electron-irradiated graphite studied by transmission electron microscopy. II. Analysis of extended energy-loss fine structure of highly oriented pyrolytic graphite. Philos Mag A 1997;76:691–700. doi:10.1080/01418619708214030.

[71] Tanabe T, Maruyama T, Iseki M, Niwase K, Atsumi H. Radiation damadge of graphite: degradation of material parameters and defect structures. Fusion Eng Des 1995;29:428–34. doi:10.1016/0920-3796(95)80049-4.

[72] Tanabe T, Kitajima M, Nakamura K, Fujitsuka M, Shinno H, Yumoto M. Study of raman spectroscopy on carbon materials irradiated with a high current density electron beam. J Nucl Mater 1991;179-181:180–3. doi:10.1016/0022-3115(91)90056-D.

[73] Tanabe T. Radiation Damage of Graphite - Degradation of Material Parameters and Defect Structures. Phys Scr 1996;7:7–16.

[74] Muto S, Horiuchi S, Tanabe T. Local structural order in electron-irradiated graphite studied by high-resolution high-voltage electron microscopy. J Electron Microsc (Tokyo) 1999;48:767–76. doi:10.1093/oxfordjournals.jmicro.a023747.

[75] Muto S, Tanabe T. Fragmentation of graphite crystals by electron irradiation at elevated temperatures. J Electron Microsc (Tokyo) 1999;48:519–23. doi:10.1093/oxfordjournals.jmicro.a023710.

[76] Tanabe T, Niwase K, Tsuhuda N, Kuramoto E. On the characterization of graphite. J Nucl Mater 1992:330–4.

[77] Takeuchi M, Muto S, Tanbe T. Structural change in graphite under electron irradiation at low temperatures. J Nucl Mater 1999;271&272:280–4. doi:10.1016/S0022-3115(98)00714-4.

[78] Muto S, Tanabe T. Temperature efect of electron-irradiatin-induced structural modification in graphite. J Nucl Mater 2000.

[79] Windes W. Data Report on Post- Irradiation Dimensional Change in AGC-1 Samples. 2012.

[80] Hammond C. The Basics of Crystallography and Diffraction. Third Edit. Oxford University Press 1960; 2009.

[81] Steadman R. Crystallography. Van Nostrand Reinhold (UK) Co. Ltd.; 1982.

[82] Warren BE. X-ray Diffraction in Random Layer Lattices. A J Exp Theor Phys 1941;59:693–8. doi:10.1103/PhysRev.59.693.

[83] Goggin PR, Henson RW, Perks AJ, Reynolds WN. Dimensional changes in the irradiated graphite lattice. Carbon N Y 1964;1:189–200. doi:10.1016/0008-6223(64)90075-2.

[84] Zhou Z, Bouwman WGGG, Schut H, Pappas C. Interpretation of X-ray diffraction patterns of (nuclear) graphite. Carbon N Y 2014;69:17–24. doi:10.1016/j.carbon.2013.11.032.

[85] Milev A, Wilson M, Kannangara GSK, Tran N. X-ray diffraction line profile analysis of nanocrystalline graphite. Mater Chem Phys 2008;111:346–50. doi:10.1016/j.matchemphys.2008.04.024.

[86] Howe JY, Cavin BO, Drakeford AE, Peascoe RA, Zontek TL, Miller DJ. Influence of Bulk Graphite Thickness on the Accuracy of X-Ray Diffraction Measurement I . Introduction III . Results and Discussion. 2007 Carbon Conf. Proc., 2007, p. 1–5.

[87] Howe JY, Rawn CJ, Jones LE, Ow H. Improved crystallographic data for graphite. Powder Diffr 2003;18:150–4. doi:10.1154/1.1536926.

[88] Williamson G. K, Hall W. H. X-ray linea broadening from filed Aluminium and Wolfram. Acta Crystallogr 1953;1:22–31. doi:10.1016/0001-6160(53)90006-6.

[89] Solin SA, Ramdas AK. Raman Spectrum of Diamond*. Phys Rev B 1970;1.

[90] Ramdas AK. A Case History in Raman and Brillouin Scattering: Lattice Vibrations and Electronic Excitations in Diamond. In: Willes H. Weber RM, editor. Raman Scatt. Mater. Sci., Springer; 2000.

[91] Prawer S, Nemanich RJ. Raman spectroscopy of diamond and doped diamond. Philos Trans A Math Phys Eng Sci 2004;362:2537–65. doi:10.1098/rsta.2004.1451.

[92] Nemanich RJ, Solin SA. First and second order Raman scattering from finite-size crystals of graphite. Phys Rev B 1979;20.

[93] Reich S, Thomsen C. Raman Spectroscopy of graphite. Philos Trans A Math Phys Eng Sci 2004;362:2271–88. doi:10.1098/rsta.2004.1454.

[94] Kwiecinska B, Suárez-Ruiz I, Paluszkiewicz C, Rodriques S. Raman spectroscopy of selected carbonaceous samples. Int J Coal Geol 2010;84:206–12. doi:10.1016/j.coal.2010.08.010.

[95] Tuinstra F, Koenig JL. Raman spectra of graphite. J Chem Phys 1970;53.

[96] Gouadec G, Colomban P. Raman Spectroscopy of nanomaterials: How spectra relate to disorder, particle size and mechanical properties. Prog Cryst Growth Charact Mater 2007;53:1–56. doi:10.1016/j.pcrysgrow.2007.01.001.

[97] Ni Z, Wang Y, Yu T, Shen Z. Raman spectroscopy and imaging of graphene. Nano Res 2010;1:273–91. doi:10.1007/s12274-008-8036-1.

[98] Pimenta MA;, Dresselhaus G, Dresselhaus MS, Cançado LG, Jorio A, Saito R. Studying disorder in graphite-based systems by Raman spectroscopy. Phys Chem Chem Phys 2007;9:1276–91. doi:10.1039/b613962k.

[99] Dresselhaus MS, Jorio A, Souza Filho AG, Saito R. Defect characterization in graphene and carbon nanotubes using Raman spectroscopy. Philos Trans A Math Phys Eng Sci 2010;368:5355–77. doi:10.1098/rsta.2010.0213.

[100] Vidano R, Fischbach DB. New lines in the Ramana Spectra of carbons and graphite. J Am Ceram Soc 1978;61:13–7. doi:10.1111/j.1151-2916.1978.tb09219.x.

[101] Ferrari AC. Raman spectroscopy of graphene and graphite: Disorder, electron–phonon coupling, doping and nonadiabatic effects. Solid State Commun 2007;143:47–57. doi:10.1016/j.ssc.2007.03.052.

[102] Thomsen C, Reich S. Double Resonant Raman Scattering in Graphite. Phys Rev Lett 2000;85:5214–7. doi:10.1103/PhysRevLett.85.5214.

[103] Maultzsch J, Reich S, Thomsen C. Double-resonant Raman scattering in graphite: Interference effects, selection rules, and phonon dispersion. Phys Rev B 2004;70:155403. doi:10.1103/PhysRevB.70.155403.

[104] Nemanich RJ, Lucovsky G. Optical Probes of the Lattice Dynamics of Graphite*. Mater Sci Eng 1977;31:157–60.

[105] Dresselhaus MS;, Jorio A, Saito R. Characterizing Graphene, Graphite, and Carbon Nanotubes by Raman Spectroscopy. Annu Rev Condens Matter Phys 2010;1:89–108. doi:10.1146/annurev-conmatphys-070909-103919.

[106] McCreery RL. Advanced carbon electrode materials for molecular electrochemistry. Chem Rev 2008;108:2646–87. doi:10.1021/cr068076m.

[107] Al-Jishi R, Dresselhaus G. Lattice dynamic model for alkali-metal-graphite intercalation compounds. Phys Rev B 1982;26.

[108] Dresselhaus MS, Chieu TC, Endo M. Raman studies of benzene-derived graphite fibers. Phys Rev B 1982;26.

[109] Wang Y, Alsmeyer DC, Mccreery RL. Raman spectroscopy if carbon materials: structural basis of observed spectra. Chem Mater 1990;2:557–63.

[110] Kawashima Y, Katagiri G. Observation of the out-of-plane mode in the Raman scattering from the graphite edge plane. Phys Rev B 1999;59:62–4. doi:10.1103/PhysRevB.59.62.

[111] Katagiri G, Ishida H, Ishitani A. Raman spectra of graphite edge planes. Carbon N Y 1988;26:565–71. doi:10.1016/0008-6223(88)90157-1.

[112] Wilhelm H, Lelaurain M, McRae E, Humbert B. Raman spectroscopic studies on well-defined carbonaceous materials of strong two-dimensional character. J Appl Phys 1998;84:6552. doi:10.1063/1.369027.

[113] Ferrari AC, Robertson J. Interpretation of Raman spectra of disordered and amorphous carbon. Phys Rev B 2000;61:14095–107. doi:10.1103/PhysRevB.61.14095.

[114] Knight DS, White EB. Characterization of diamond films by Raman spectroscopy 1989;16802:385–93.

[115] Cançado LG, Takai K, Enoki T, Endo M, Kim Y a., Mizusaki H, et al. General equation for the determination of the crystallite size L[sub a] of nanographite by Raman spectroscopy. Appl Phys Lett 2006;88:163106. doi:10.1063/1.2196057.

[116] Tasco JMD, Cuesta A, Dhamelincourt P, Laureyns J. Comparative performance of X-ray diffraction and Raman microprobe techniques for the study of carbon materials. J Mater Chem 1998;8:2875–9. doi:10.1039/A805841E.

[117] Nikiel L, Jagodzinski PW. Raman spectroscopic characterization of graphites: A re-evaluation of spectra/ structure correlation. Carbon N Y 1993;31:1313–7. doi:10.1016/0008-6223(93)90091-N.

[118] Ammar MR, Rouzaud JN. How to obtain a reliable structural characterization of polished graphitized carbons by Raman microspectroscopy. J Raman Spectrosc 2012;43:207–11. doi:10.1002/jrs.3014.

[119] Maslova OA, Ammar MR, Guimbretière G, Rouzaud J-N, Simon P. Determination of crystallite size in polished graphitized carbon by Raman spectroscopy. Phys Rev B 2012;86:134205. doi:10.1103/PhysRevB.86.134205.

[120] Dillon RO, Woollam JA, Katkanant V. Use of Raman scattering to investigate disorder and crystallite formation in as-deposited and annealed carbon films. Phys Rev B 1984;29.

[121] McCulloch DG, Prawer S, Hoffman A. Structural investigation of xenon-ion-beam-irradiated glassy carbon. Phys Rev B 1994;50. doi:10.1103/PhysRevB.50.5905.

[122] Chu PK, Li L. Characterization of amorphous and nanocrystalline carbon films. Mater Chem Phys 2006;96:253–77. doi:10.1016/j.matchemphys.2005.07.048.

[123] Williams DB, Carter CB. Transmission Electron Microscopy A textbook for Material Science. 2nd ed. Springer; 2009.

[124] Pawlyta M. Transmission electron microscope studies on carbon nanostructured materials. Arch Mater Sci Eng 2013;63:58–67.

[125] Mironov BE, Freeman HM, Brydson RMD, Westwood a VK, Scott a J. Simulating Neutron Radiation Damage of Graphite by In-situ Electron Irradiation. J Phys Conf Ser 2014;522:012051. doi:10.1088/1742-6596/522/1/012051.

[126] Brydson R. Electron Energy Loss Spectroscopy. BIOS Scientific Publishers Ltd; 2001.

[127] Egerton RF. Electron Energy-Loss Spectroscopy in the Electron Microscope. 3rd ed. Springer; 2011.

[128] Fink J, Muller-Heinzerling T, Pfluger J, Scheerer B, Dischler B, Koidl P, et al. Investigation of hydrocarbon-plasma-generated carbon films by electron-energy-loss spectroscopy. Phys Rev B 1984;30:4713–8. doi:10.1103/PhysRevB.30.4713.

[129] Laffont L, Monthioux M, Serin V. Plasmon as a tool for in situ evaluation of physical properties for carbon materials. Carbon N Y 2002;40:767–80. doi:10.1016/S0008-6223(01)00196-8.

[130] Stöger-Pollach M. Optical properties and bandgaps from low loss EELS: pitfalls and solutions. Micron 2008;39:1092–110. doi:10.1016/j.micron.2008.01.023.

[131] Batson PE. Carbon 1s near edge absorption fine structure in graphite. Phys Rev B 1993;48:2608–10. doi:10.1103/PhysRevB.48.2608.

[132] Berger SD, McKenzie DR, Martin PJ. EELS analysis of vacuum arc-deposited diamond-like films. Philos Mag Lett 1988;57:285–90. doi:10.1080/09500838808214715.

[133] Mansot JL, Wery J. Quantitative study of irradiation damage in organo-metallic colloidal particles. Microsc Microanal Microstruct 1993;4:87–100. doi:10.1051/mmm:019930040108700.

[134] Daniels HR, Brydson R, Rand B, Brown a. P. Investigating carbonization and graphitization using electron energy loss spectroscopy (EELS) in the transmission electron microscope (TEM). Philos Mag 2007;87:4073–92. doi:10.1080/14786430701394041.

[135] Zhang Z, Brydson R, Aslam Z, Reddy S, Brown AP, Westwood A, et al. Investigating the structure of non-graphitising carbons using electron energy loss spectroscopy in the transmission electron microscope. Carbon N Y 2011;49:5049–63. doi:10.1016/j.carbon.2011.07.023.

[136] Menon NK, Yuan J. Quantitative analysis of the effect of probe convergence on electron energy loss spectra of anisotropic materials. Ultramicroscopy 1998;74:83–94. doi:10.1016/S0304-3991(98)00029-1.

[137] Souche C, Jouffrey B, Hug G, Nelhiebel M. Orientation Sensitive EELS-Analysis of Boron Nitride Nanometric Hollow Spheres. Micron 1999;29:419–24. doi:10.1016/S0968-4328(98)00030-4.

[138] Paxton AT, Schilfgaarde van M, MacKenzie M, Craven AJ. The near-edge structure in energy-loss spectroscopy : many-electron and magnetic effects in transition metal nitrides and carbides. J Phys Condens Matter 2000;729:729–50.

[139] Daniels H, Brown AP, Scott A, Nichells T, Rand B, Brydson R. Experimental and theoretical evidence for the magic angle in transmission electron energy loss spectroscopy. Ultramicroscopy 2003;96:523–34. doi:10.1016/S0304-3991(03)00113-X.

[140] Hébert C, Schattschneider P, Franco H, Jouffrey B. ELNES at magic angle conditions. Ultramicroscopy 2006;106:1139–43. doi:10.1016/j.ultramic.2006.04.030.

[141] Schattschneider P, Hébert C, Franco H, Jouffrey B. Anisotropic relativistic cross sections for inelastic electron scattering, and the magic angle. Phys Rev B 2005;72:045142. doi:10.1103/PhysRevB.72.045142.

[142] Jouffrey B, Schattschneider P, Hébert C. The magic angle: a solved mystery. Ultramicroscopy 2004;102:61–6. doi:10.1016/j.ultramic.2004.08.006.

[143] Zobelli a., Gloter a., Ewels C, Seifert G, Colliex C. Electron knock-on cross section of carbon and boron nitride nanotubes. Phys Rev B 2007;75:245402. doi:10.1103/PhysRevB.75.245402.

[144] Krasheninnikov A V, Nordlund K. Ion and electron irradiation-induced effects in nanostructured materials. J Appl Phys 2010;107:71301. doi:10.1063/1.3318261.

[145] Banhart F. Irradiation effects in carbon nanostructures. Reports Prog Phys 1999;62:1181–221. doi:10.1088/0034-4885/62/8/201.

[146] Oen OS. Cross sections for atomic displacements in solids by fast electrons. ORNL- 3813. Oak Ridge National Laboratory; 1965.

[147] Henrard L, Stephan O, Colliex C. Electron Energy Loss study of plasmon excitation in curved carbon network. Synth Met 1999;103:2502–3. doi:10.1016/S0379-6779(98)01072-8.

[148] Gass MH, Bangert U, Bleloch AL, Wang P, Nair RR, Geim AK. Free-standing graphene at atomic resolution. Nat Nanotechnol 2008;3:676–81. doi:10.1038/nnano.2008.280.

[149] Marinopoulos A, Reining L, Olevano V, Rubio A, Pichler T, Liu X, et al. Anisotropy and Interplane Interactions in the Dielectric Response of Graphite. Phys Rev Lett 2002;89:076402. doi:10.1103/PhysRevLett.89.076402.

[150] Banhart F. The role of lattice defects in the formation of new carbon structures under electron irradiation. Japanese Soc Electron Microsc 2002;51:189–94. doi:10.1093/jmicro/51.Supplement.S189.

[151] Magnuson M, Andersson M, Lu J, Hultman L, Jansson U. Electronic structure and chemical bonding of amorphous chromium carbide thin films. J Phys Condens Matter 2012;24:225004. doi:10.1088/0953-8984/24/22/225004.

[152] Niwase K. Irradiation-induced amorphization of graphite. Phys Rev B 1995;52.

[153] Zheng G, Xu P, Sridharan K, Allen T. Characterization of structural defects in nuclear graphite IG-110 and NBG-18. J Nucl Mater 2014;446:193–9. doi:10.1016/j.jnucmat.2013.12.013.

[154] Seehra MS, Pavlovic AS. X-ray diffraction, thermal expansion, electrical conductivity, and optical microscopy studies of coal-based graphites. Carbon N Y 1993;31:557–64.

[155] Seehra MS, Pavlovic AS, Babu VS. MEASUREMENTS AND CONTROL OF ANISOTROPY TEN COAL-BASED GRAPHITES. Carbon N Y 1994;32:431–5.

[156] Joyce MRR, Marrow TJJ, Mummery P, Marsden BJ j. Observation of microstructure deformation and damage in nuclear graphite. Eng Fract Mech 2008;75:3633–45. doi:10.1016/j.engfracmech.2007.11.003.

[157] Hall G, Marsden BJJ, Fok SLL. The microstructural modelling of nuclear grade graphite. J Nucl Mater 2006;353:12–8. doi:10.1016/j.jnucmat.2006.02.082.

[158] Bradford MR, Steer AG. A structurally-based model of irradiated graphite properties. J Nucl Mater 2008;381:137–44. doi:10.1016/j.jnucmat.2008.07.040.

[159] Morgan MS, Schlag WH, Wilt H. Surface Properties of the Quinoline-Insoluble Fraction of Coal-Tar. J Chem Eng Data 1960;5:81–4. doi:10.1021/je60005a020.

[160] Iwashita N, Park CR, Fujimoto H, Shiraishi M, Inagaki M. Specification for a standard procedure of X-ray diffraction measurements on carbon materials. Carbon N Y 2004;42:701–14. doi:10.1016/j.carbon.2004.02.008.

[161] Cox JH, Helm JW. Graphite Irradiations 300 ~1200C. Carbon N Y 1969;7:319–27. doi:10.1016/0008-6223(69)90115-8.

[162] Nakai K, Kinoshita C, Matsunaga A. A study of amorphization of graphite using e and ion irradiation. Ultramicroscopy 1991;39:361–8.

[163] McCulloch DG, Brydson R, Search H, Journals C, Contact A, Iopscience M. approach Carbon K-shell near-edge structure calculations for graphite using the multiple-scattering approach. J Phys Condens Matter 1996;3835:3835–41.

[164] Daniels HR. Novel Characterization Techniques for Cabonaceous Materials in the FEGSTEM. 2003.

[165] Hébert C, Jouffrey B, Schattschneider P. Comment on "Experimental and theoretical evidence for the magic angle in transmission electron energy loss spectroscopy" by H. Daniels, A. Brown, A. Scott, T. Nichells, B. Rand and R. Brydson. Ultramicroscopy 2004;102:61–6. doi:10.1016/j.ultramic.2004.08.006.

[166] Blaha P, Schattschneider P, Louf P-HP, Luitz J, Nelhiebel M, Schwarz K, et al. The orientation-dependent simulation of ELNES. Ultramicroscopy 2000;83:9–16.

[167] Windes WE, Swank WD, Rohrbaugh DT, Lord JR. AGC-2 Graphite Preirradiation Data Analysis Report. 2013.

[168] Burchell TD. Irradiation induced creep behavior of H-451 graphite. J Nucl Mater 2008;381:46–54. doi:10.1016/j.jnucmat.2008.07.022.

[169] Liang T. Something about nuclear graphite. Http://www.iaea.org/ n.d. http://www.iaea.org/NuclearPower/Downloadable/Meetings/2012/2012-10-22-10-26-WS-NPTD/Day-3/14.Liang.pdf.

[170] Lutcov AI, Volga VI, Dymov BK. Thermal conductivity, electric resistivity and specific heat of dense graphites. Carbon N Y 1970;8:753–60. doi:10.1016/0008-6223(70)90100-4.

[171] Limited Az. Graphite (C) - Classifications , Properties and Applications of Graphite. 2013.

[172] Kelly BT. The effect of defects on the basal plane thermal conductivity. Carbon N Y 1967;5. doi:10.1016/0008-6223(67)90006-1.